Dissertation

Cold, Dense, and Slow Samples of Polyatomic Molecules for Collision Experiments

Thomas Gantner

23/05/19

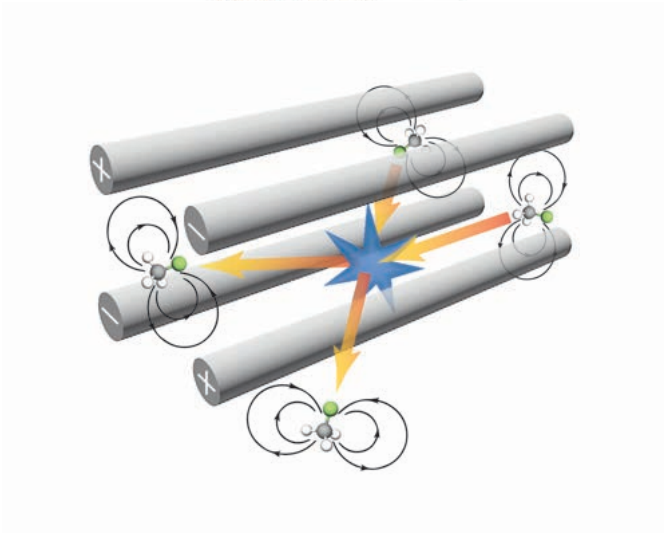

Technische Universität München
Fakultät Physik
Max-Planck-Institut für Quantenoptik

Technische Universität München
Max-Planck-Institut für Quantenoptik

Cold, Dense, and Slow Samples of Polyatomic Molecules for Collision Experiments

Thomas Gantner

Vollständiger Abdruck der von der Fakultät für Physik der Technischen Universität München zur Erlangung des akademischen Grades eines

Doktors der Naturwissenschaften (Dr. rer. nat.)

genehmigten Dissertation.

Vorsitzender :	Prof. Dr. Michael Knap
Prüfer der Dissertation :	1. Hon.-Prof. Dr. Gerhard Rempe
	2. Prof. Dr. Johannes Barth

Die Dissertation wurde am 24.06.2019 bei der Technischen Universität München eingereicht und durch die Fakultät für Physik am 07.10.2020 angenommen.

Abstract

Cold polar molecules provide fascinating research possibilities in physics and chemistry. They are currently used to investigate fundamental questions about the Standard Model of physics by measuring the electric dipole moment of the electron, or employed to understand the nature of dark matter. Furthermore, they are envisioned as tools for quantum information processing, as quantum memories or as link for quantum information stored and transmitted in different frequency regimes. In chemistry, they are utilized to examine the role of quantum mechanics in particle interactions. This research can lead to a better understanding of chemical reactions. The ultimate goal would be to control the collisions and reactions on a fundamental level, by manipulating all internal and external degrees of freedom of the interaction partners.

All these applications and ideas depend on a great level of control over the molecules, therefore, they need to be cooled and slowed. Additionally, for most proposals based on cold molecules, it is necessary to start with a trapped, dense sample of molecules to achieve strong molecule-molecule interactions and a high level of control. These are the goals that were pursued in this thesis. Firstly, a buffer gas cell was set up to cool the molecules, the translational as well as their internal, rotational degrees of freedom. To improve this scheme, a Monte-Carlo simulation was developed, that led to a better understanding of the cell dynamics, and can be used for future setup and optimization of buffer gas cells. The buffer gas cell produces cold beams of molecules, however, these beams are still to fast to be trapped in any available trap. Therefore, the cryogenic cell is combined with a centrifuge decelerator, which achieved a record high flux exceeding $10^{10}\mathrm{s}^{-1}$ and densities up to $10^{9}\mathrm{cm}^{-3}$ of internally cold polar molecules with a single state purity of up to 92% at kinetic energies corresponding to less than 1K. Due to these densities, collisions between the cold molecules could be observed for the first time, even though their interaction time was limited to few milliseconds during the time-of-flight from the centrifuge to the detector. To further improve the system, a microstructured electrostatic trap was installed, which is used to hold the molecules for several seconds. During that time, the molecules can be further investigated, e.g. to measure their energy, or manipulated by selecting only the slowest ones. In the trap, further investigation of the collisional properties of the molecules is possible, for example to find a molecule suitable for evaporative cooling. Additionally, the geometry of the trap is ideally suited to perform Sisyphus cooling to the sub-millikelvin regime.

Contents

1 Introduction

1.1 Who likes molecules?

More than 30 years ago, the first atoms were decelerated [PM82, WI79] and could later be completely stopped by laser light [EBHZ85, PMP$^+$85]. Atoms could then be trapped for several seconds in a magneto-optical trap (MOT) [RPC$^+$87]. Soon after, further cooling steps were invented [DCT89, LWW$^+$88, AAK$^+$88], and the implementation of new magnetic traps led to the evaporative cooling [PAEC95, DMJ$^+$95], and finally to Bose-Einstein condensation of atoms [DMA$^+$95, ARM$^+$95]. Ever since then, more and more tools to produce and control cold atoms have been developed [GWO00, LAKC96], and atoms have evolved to become the fundamental tools for a new era of physics such as quantum information [BMDM04, SNR$^+$11], quantum simulation [GME$^+$02, BDZ08] or high precision clocks [UHH02, THHK05], just to name a few.

In this field, that is mostly limited to alkaline and alkaline earth atoms, molecules look like the two-faced Roman god Janus: The vast number of different molecules and their rich internal structure is a great promise for new, very different effects and applications. At the same time, their great variety can look confusing, and the internal complexity makes a full control seem unfeasible. However, the advantages were compelling to many people, and experiments progressing towards cold molecules were established. In the last years great progress has been made towards full control of molecules, and soon they might become the new workhorse to perform experiments beyond the possibilities of atoms.

One property that strongly distinguishes molecules from atoms is their electric dipole moment. This dipole moment leads to a strong, long ranged, anisotropic interaction between the molecules. Polyatomic, symmetric-top molecules are particularly interesting, as they possess a permanent dipole moment and consequently a exhibit a linear Stark effect with external electric fields. These interactions are expected to make molecules especially suitable for applications in quantum simulation [BDPZ12] or computation [DeM02], and more [YMG$^+$13]. In this thesis, the first dipolar molecule-molecule collisions at energies below $1K \cdot k_B$ are observed and investigated, by using a unprecedented flux and density of slow molecules produced by the Cryofuge. Furthermore, the understanding of the cryogenic buffer gas cell for the production of cold molecule samples was improved, and an electrostatic trap for 3D trapping of the slow molecule beam was installed and characterized.

In the introduction, I will present the applications that are envisioned or already implemented for cold molecules, and afterwards the different approaches to achieve cooling, slowing and trapping of molecules. In the end of the chapter, I will give an outline of the rest of this thesis that focused on the implementation of techniques to cool, decelerate, and trap polyatomic, chemically stable, dipolar molecules, and the investigation of their collisional properties at low energies.

1.2 Applications of cold molecules

1.2.1 Measurements of fundamental constants

Electron electric dipole moment One of the great advantages of molecules which is already used in experiments and producing state-of-the-art results, are the big internal electric fields of up to 100 GV/cm [MB08, SPT13]. As these fields can be many orders of magnitude bigger than fields conventionally produced in a lab of about 100 kV/cm, the interaction with any dipole inside the molecule is greatly enhanced. This effect is used to search for an electric dipole moment of the electron (eEDM). The Standard Model of particle physics predicts this eEDM to be extremely small, less than $10^{-40} e \cdot cm$, with e the charge of an electron. And even though the Standard Model has been very successful in describing particle physics in great detail, it is known to be incomplete. For example, the CP-violation provided by the Standard Model is not enough to explain the matter-antimatter imbalance observed in the universe [CDS12].

Theories that extend the Standard Model predict larger eEDMs, and these are within reach of current experiments. Therefore, several groups are investigating in this direction, pushing for measurements with a greater and greater precision.

For the experiment, the molecules are prepared in a coherent superposition of two Zeeman sublevels. After the preparation, they interact with the electric and magnetic fields. Here, the laboratory electric field can be small, as it is only used to polarize the molecules, and the internal molecule electric field is the one that interacts with the electron. After the interaction, the final state of the molecule is detected by pumping the molecule into a decaying bright state from both of the Zeeman sublevels and examining the asymmetry. For a more detailed description, see [Hut14, Rab16].

In recent years, the value of the eEDM found in experiments has always been consistent with zero, but with a rapidly decreasing upper bound [CBC$^+$14, HKS$^+$11, CGG$^+$17]. All these experiments rely on molecules, ThO, YbF, and HfF^+, respectively, improving previous best results obtained in atom experiments by orders of magnitude [RCSD02]. The latest result in [AH18] gave an upper bound to the eEDM of $1.1 \cdot 10^{-29} e \cdot cm$. With this limit, some of the theories extending the Standard Model, as for example most supersymmetric models, can already be excluded. The

work to further improve this limit or to eventually measure the value of the eEDM are still ongoing, and promise more fascinating results in the future. It is worth to mention here that these experiments benefit from cold and slow molecules, as the low temperature increases the population of the investigated ground state of the molecule, and a small forward velocity increases the interrogation time of the molecules in the beam experiments.

Search for dark matter Another idea to test physics on a fundamental level using molecules is the detection of dark matter axions. Axion-like particles are one proposed dark matter particle candidate, among others [Fen10], and are searched for in different systems based on a microwave cavity detector or a superconducting quantum interference device (Squid)[DST$^+$06, ACH$^+$10], without employing molecules. These experiments were able to exclude the existence of axions in a mass range of about 2.0 µeV to 3.5 µeV.

It was already proposed early on that molecules would be a suitable tool to detect dark matter [ZS88], a large number of molecular radicals, diatomic and polyatomic molecules were listed as candidates. As dark matter detectors, dipole forbidden transitions in the molecules would be excited by the dark matter axions. While this process is also possible in atoms, the large variety of transitions in molecules make them perfectly suited for this type of experiments. For example, a system based on a O_2 sample cooled to 280 mK was proposed that could be sensitive to a mass range of 1.4 meV to 1.9 meV [SBC$^+$15]. More recently, even a very wide detection range between 0.2 eV to 20 eV is proposed based on resonant axion absorption in molecules [ADVT18]. All these experiments rely on a good control over the molecules under investigation.

1.2.2 Quantum Information Processing

Quantum information processing is widely regarded as next possible big step in information technology, as it could substantially speed up certain processes that are extremely time consuming and difficult on classical computers. For example, Shor's algorithm shows how the factorization of large numbers can be finished in polynomial time, using the power of quantum gates [Sho94]. While an implementation of this technique can render current encryption methods useless, the setup of a "quantum internet" could in turn provide unbreakable communication channels [Eke91].

To implement quantum gates, quantum memories, or quantum nodes, molecules offer several advantages. Molecular states can have long lifetimes, and are therefore suitable to act as quantum bits (qubits)[TdVR02]. In a system of a two-atomic gas of NaK molecules, first steps towards molecules as quantum memory has been made by demonstrating a coherence time close to 1 s [PYL$^+$17].

As previously mentioned, molecules can posses a large electric dipole moment, and can be controlled by electric fields which gives the ability to move them around more

easily. Moreover, due to the dipole moment, they strongly interact with each other. This large interaction could be used to couple single molecules acting as qubits with each other. This idea was already suggested in 2002 by DeMille [DeM02], and developed since then. Many of the ideas start from bialkalis [LO05, JBJDL13, NRG18], but also other diatomic molecules are considered [YKC06, KSF+16], and also bigger ones like polyatomic symmetric top molecules are contemplated [WKFH11, SB09].

Another benefit of molecules is their strong interaction with microwave radiation which arises from their internal rotational states. With this, they can couple to superconducting stripline cavities [ADD+06], and as a longterm vision, hybrid systems made from mesoscopic solid state devices and single molecules become possible. This will first require a fully quantum controlled system, and a careful choice of the molecule species.

1.2.3 Cold and controlled collisions

Another application of cold molecules is not as a tool for further applications, but to use the molecules themselves as study object. In contrast to molecule interactions and reactions at room temperature and above, when a large number of internal states are occupied and many reaction channels are available, the behavior can change drastically when examining cold or ultracold molecules. An overview over the prospects of cold molecules for collision studies is found in [Bal16]. Another recent review about cold molecules and their prospects is given in [BRY17].

Astrophysics Even moderately cold samples of molecules are of interest for astrophysics. Although most of the mass in the universe is made up of hydrogen and helium, a variety of molecules exist in molecular clouds in interstellar space, where temperatures typically range between 10 K and 20 K [Fer01]. Herbst and Millar [HM08] or more recently Tielens [Tie13] give an extensive list of molecules found in space, including the symmetric tops methanol and deuterated ammonia that were used for this work. Methanol is particularly interesting, as it can be used to perform spectroscopy that sets a limit on variations of the proton-to-electron mass ratio [BDJ+13]. Understanding the interactions between the molecules at these low temperatures can even help to understand the process of star formation [MO07].

Quantum properties For even smaller temperatures, the quantum mechanical properties of the molecules surface, and appear as resonances when determining the collisions cross sections for varying collision energy. This was shown by Narevicius and coworkers [HGS+12] when recording the Penning ionization rate between molecular hydrogen H_2 and metastable helium He^*. The collision energy was reduced by merging two beams of similar velocity, reducing the relative velocity in a co-moving frame between the collision partners. More recently, the same technique

was used to observe a clear difference in scattering behavior for two different rotational states of H_2 at collision energies corresponding to a temperature of well below 1 K [KSS+17]. Penning ionization of merged beams was also used by Osterwalder et al. to search for resonances in the $CH_3F + Ne$ system at energies corresponding to 150 mK to 56 K.

Velocity map imaging Velocity map imaging was implemented by Meerakker et al. to examine molecule-atom collisions in a crossed beam experiment [VZOV+14]. This technique is not only sensitive to the absolute velocity and direction of the produced particle, but by considering energy and momentum conservation can also detect the final internal state of the molecular ion. With this, they were able to measure differential cross section for inelastic collisions of NO with He, Ne, and Ar.

Dipole-dipole interactions In 2010, the group of Ye et al. investigated the non-homogeneous behavior of dipolar molecules, using an ultracold gas of KRb molecules in a pancake-shaped optical dipole trap [NOW+10, ONW+10]. In this setup, they were able to alter the interactions between the molecules by applying static electric fields. The alignment of the molecular dipoles by electric field leads to a drastically anisotropic interaction depending on the collision happening side-to-side or head-to-tail. Recently, many more experiments were set up to produce ultracold molecules out of two alkali atoms, like RbCs, NaRb, or NaK[TRS+14, MGJ+14, PWZ15, GZL+16, SBL+18], and set out to examine long-range molecule-molecule interactions in detail.

Notwithstanding the developments for the bialkali molecules, polyatomic molecules would be ideally suited to investigate dipole-dipole interactions. These possess a permanent electric dipole moment and consequently exhibit a linear Stark effect, which leads to strong interactions, even at small electric fields. One of the molecules investigated in this thesis, CH_3F, was also proposed to be used to examine quantum magnetism [WMC15].This thesis makes a step towards the understanding of these interactions by investigating for the first time the collisions between polyatomic molecules at a collision energy below 1 K in a 2D trap environment.

1.3 Producing cold molecules

For all the envisioned and already implemented applications mentioned above, getting molecules under control and achieve cold or even ultracold temperatures is a prerequisite. In general, there are two different approaches to produce cold molecules. Indirect cooling methods begin with samples of cold or ultracold atoms, and assemble the molecules from the sample of atoms. This way, the established techniques to cool atoms can be used, and the quantum optical toolbox that was developed

over the last decades is at hand. As a drawback, this method is currently limited to alkali dimers.

Alternatively, molecules can also be cooled directly. Here, molecules are first produced or taken from a gas bottle, and then cooled and decelerated until they can be trapped. These direct methods work for a much wider variety of different molecules, and therefore are the only possible way to go for some of the applications. However, the temperature and precise control achieved here cannot yet rival the indirect cooling methods.

I will give an overview over the different approaches to molecule cooling and slowing that are implemented or currently being developed. The focus will be on the direct methods, as these are the ones that are realized in this work.

1.3.1 Indirect cooling of molecules

Indirect cooling of molecules starts with direct cooling of atoms. Currently, all existing indirect cooling methods assemble molecules out of two of the five stable alkali elements, using the standard techniques of Zeeman deceleration and magneto-optical trapping. Some of the dimers can react exothermically in the form of $AB + AB \rightarrow A_2 + B_2$ and are therefore not stable in molecule collisions, which reduces the number of possible combinations for chemically stable, dense molecule samples [ŻH10]. Most of the current experiments employ dimers of two different elements, as these have a large electric dipole moment.

After cooling and spatially overlapping the atoms either in optical dipole traps [AAH$^+$10, MGJ$^+$14, PWZ15, GZL$^+$16, SBL$^+$18] or lattices [TRS$^+$14], the atoms have to be associated to form a molecule. This can be done by photoassociation, where a pair of atoms is excited to a higher lying molecular state via a laser, followed by a spontaneous decay or a stimulated emission to a stable molecule state. This was first demonstrated in 2000 for Cs_2 [FCC$^+$98], and later for KRb [WQS$^+$04].

Most of the experiments working on alkali dimers now employ a different idea. To utilize the so-called Feshbach association, the unbound scattering states of the atoms are tuned via a magnetic field in resonance with a molecular state lying close to the dissociation threshold. At the resonance, the scattering length of the atoms diverges, and the atoms can enter the short-lived molecular state.

The next step after photoassociation as well as after Feshbach association, is to achieve long-lived molecules that can be used for further experiments. Therefore, the vibrational and rotational ground state of the molecule has to be reached. This is implemented using lasers that induce a resonant transfer to the desired state. In the first implementations, two photons were used to induce a non-coherent Raman transfer, but to increase the efficiency the transfer can be done coherently via a stimulated Raman adiabatic passage (STIRAP). As the internal structure of the molecules is typically complicated, and theoretical predictions of the energy levels

and transfer strengths are imprecise, it can be a tedious task to perform spectroscopy to find suitable transitions for this process.

1.3.2 Direct cooling of molecules

To be able to use more diverse classes of molecules, direct cooling methods have to be applied. When starting out with room temperature or even hotter molecules, the choice of molecule species is not as strictly limited as for the indirect cooling methods. For the measurements of fundamental constants, when properties of certain molecules are necessary, direct cooling of these molecules is the only practical way. Also for collision and reaction studies, it is important to investigate molecules that, for example, appear in interstellar space or have interesting internal properties. And in fact, many of the direct cooling methods have been designed to be relatively general and have few requirements on the molecule properties.

Buffer gas cooling One of the most general cooling techniques is to use a buffer gas cell. It was first implemented to cool molecules in 1998 by Weinstein et al. [WdG$^+$98]. The underlying idea is to sympathetically cool the molecules via collisions with a cold buffer gas, typically helium or another noble gas. When warm molecules and cold buffer gas mix inside a cryogenic cell, the buffer gas atoms cool down the molecules to the cell temperature that can be as low as the condensation point of the buffer gas. When the molecule density is chosen much smaller than the buffer gas density, the molecules cannot form ice because molecule-molecule collisions are rare. Moreover, the buffer gas atoms can hinder the molecules from reaching the cell walls and avoid freezing. A small output nozzle in the cell allows the formation of a beam of the cooled molecules. With this method, including expansion cooling out of the cell into vacuum, temperatures down to about 1 K are commonly achieved.

As the technique is very generic and relies only on collisions of the molecules with buffer gas atoms, it can be used for several different applications. Before cooling molecules, cold buffer gas was already used to cool ions [SBK$^+$91] or atoms [KFK$^+$97], or even antiprotons [GFO$^+$89]. For molecules, it can be used for radicals created in a hot plasma produced by an ablation laser [ZCW$^+$14] or a glow source[ECF$^+$04], or also for chemically stable molecules that can simply come from a gas bottle [vBSM$^+$09]. Importantly, in the buffer gas cell not only the external, translational degrees of freedom are cooled, but simultaneously the internal vibrational and rotational degrees of freedom [WGZ$^+$16]. Due to the generality, buffer gas cells have become a very common molecule source all over the world, and often act as starting point for further molecule cooling or deceleration experiments. A good overview over buffer gas cells can be found in [HLD12].

A cryogenic buffer gas cell was also used for all the experiments in this thesis. A new simulation to understand and optimize buffer gas cells is described in chapter 2.

Stark and Zeeman deceleration Many cold molecule experiments aim to trap molecules, to be able to interrogate them over a longer time period, or to cool and manipulate them further. Even if cooled in a buffer gas cell, typically, the forward velocity of the molecules is orders of magnitude to large to be trapped in feasible electric, magnetic, microwave or optical traps. Therefore, a deceleration stage has to be realized. Two of the decelerators that were used for molecules are the Stark decelerator [BBM99] and the Zeeman decelerator [vdMBM08], which use a similar underlying idea.

In the case of the Stark decelerator, first realized in 1999 [BBM99], the molecules in a beam interact with an electric field that forms a potential hill. Upon ascending the field, the molecules are slowed down. As soon as they reach the peak of the potential, the electric fields are switched off, leaving the molecules with a smaller kinetic energy. Because electric fields achievable in a laboratory environment are much too small to stop the molecules immediately, this process is repeated many times as the molecules propagate. Later, the scheme was improved by using ring shaped electrodes to increase the transverse stability of the molecules during deceleration. Additionally, the electrodes are switched in a way that provides a decelerated three-dimensional trap for the molecules rather than many successive one dimensional hills [OMH$^+$10]. Miniaturized Stark decelerators have also been implemented as microstructured chips [MCM09a].

The Zeeman decelerator also employs the idea of repeated deceleration by successive small, fast switching potentials. In contrast to the Stark decelerators, the Zeeman decelerator provides the potential hills via magnetic instead of electric fields [NR12]. Therefore, it is applicable to different molecule species without a large electric dipole moment.

The fast switching of high electric or magnetic fields, the necessary timing precision, and the large number of deceleration stages make these experiments challenging. The reward is a setup that provides the ability to decelerate any molecule with a suitable dipole moment to mass ratio into a narrow velocity range, and an adjustable final velocity. Therefore, these decelerators are well suited for collision studies [JO15, VOC$^+$15, KSS$^+$17], and in the case of the Zeeman decelerator and the Stark chip decelerator can have a trap integrated at the output of the decelerator [AKS$^+$17, MCM09b].

One important drawback is that these types of decelerators cannot work continuously, as they rely on many successive deceleration steps tailored for a molecule pulse. If operated with a continuous source like a buffer gas cell fed from a gas bottle, the efficiency becomes very low, limited by the spatial and velocity acceptance window and switching frequency of the decelerator.

Centrifuge The centrifuge [CWB$^+$14, Wu17] was introduced to overcome the drawback of non-continuous deceleration. It uses the interaction of molecules with an electric field like the Stark decelerator, but only uses it to trap the molecules in

2D, that means, to guide the molecule beam. The deceleration is performed by a centrifugal pseudo-potential, and is constructed so that most of the molecules of a continuous beam can be decelerated. With its design it has demonstrated an input to output efficiency of a continuous molecule beam of up to 20%. The centrifuge was the basis for the low-energy molecule-molecule collision measurements, and is described in greater detail in chapter 3.

Laser cooling Laser cooling of molecules is based on the same ideas as for atoms. To be decelerated, the particles absorb a photon from a laser beam that is directed against their propagation direction, and re-emit it in 4π. In this process, the particles lose momentum due to the photon recoil. This general process is the same for Zeeman slowers, chirp slowers, and magneto-optical traps (MOTs) [PPM85]. Because the momentum transfer of a single photon is small, the absorption-emission process has to be repeated many thousand times. Therefore, it is important to find a cycling transition, so that the particle always falls back to its initial ground state.

This is possible for atoms, but proves to be a considerable challenge to find in molecules. The problem lies in the large number of internal states of moelcules. While the decay to different rotational states obeys strict selection rules and can be adjusted to achieve a closed cycling transition, the decay to vibrational states is only governed by the Franck-Condon factors (FCF) that depend on the wave function overlap between the excited and the ground state. Some molecule species that could fulfill the condition of advantageous FCFs were proposed [DR04, SSWY08]. All of these molecules are radicals, and therefore not chemically stable. Hence they cannot be purchased in a gas bottle, but have to produced directly in the experiment, for example by laser ablation in a buffer gas cell. Even with these species, however, many different laser frequencies are necessary to repump the molecules to the ground state of the cycling transition to achieve enough absorption-emission cycles.

Despite these complications, the laser cooling of molecules was achieved, first for SrF [SBD10], and later for other molecules [ZCW$^+$14, HYS$^+$13], and a cooling effect in 1D was even shown for a triatomic molecule species [KBM$^+$17] or heavy molecules [LAT$^+$18]. MOTs for molecules were realized shortly after for SrF, CaF, and YO[BMN$^+$14, TWH$^+$17, AAC$^+$17, CDW$^+$18b]. The first sub-Millikelvin MOT was presented in 2016 by DeMille and coworkers [NMS$^+$16]. Very recently, laser cooled molecules have been loaded to a magnetic trap where the temperature was further reduced to 50 µK [MSZD18], or in an optical dipole trap with a temperature of 60 µK [AAB$^+$18]. During this thesis was written, both of the experiments reported temperatures of around 5 µK [CAA$^+$18, CDW$^+$18a]. Currently, these are the lowest temperatures achieved for molecules by direct cooling techniques. The drawback of the current laser cooling experiments is the small number of sub-Millikelvin molecules produced.

Sisyphus cooling A different approach to achieve ultracold molecules by direct cooling is the opto-electrical Sisyphus cooling [ZMPR09]. Here, slow molecules are extracted from a liquid nitrogen cooled nozzle via an electrical quadrupole guide. The slowest molecules out of the Maxwell-Boltzmann distribution are selected by velocity filtering [RJR$^+$03, JRR$^+$04], and loaded into an electrostatic microstructured trap [EMS$^+$11]. The cooling process utilizes the different Stark shifts in electric fields for different internal molecular states, and an infrared laser pumps the molecules back into their initial state [ZEG$^+$12]. As the energy is extracted by the interaction with electric fields instead of the photon recoil, very few scattering processes are necessary compared to laser cooling. This method is tailored for symmetric tops, and therefore is not limited to radicals. Sisyphus cooling was demonstrated for two different polyatomic molecules, CH_3F and H_2CO (Formaldehyde). A temperature of 400 µK was achieved for a sample of 3×10^5 molecules [PIG$^+$16]. At the same time, excellent internal state purity of the molecules was obtained [GPE$^+$15, GPRZ15]. To date, this represents the largest sample of trapped molecules at a temperature below 1 mK.

The same trap as used for Sisyphus cooling was used during the work for this thesis. The implementation in the experimental setup, first trapping results, and the characterization of the system is shown in chapter 4.

1.4 About this thesis

The thesis will describe the efforts of the past years to produce slow, cold, and trapped polar polyatomic molecules. All the experiments described here are performed on chemically stable molecules, that can be commercially obtained in gas bottles, and are generally applicable to a huge variety of molecules, as they only rely on a favorable dipole moment to mass ratio of the molecule species.

After the introduction, I will describe a simulation of the buffer gas cooling and cell design used in the experiment in chapter 2. I will first introduce the buffer gas cell design that was used for all the subsequent experiments. Then I am going to introduce a new Monte-Carlo simulation based on the statistical Gambler's Ruin problem. A comparison to data obtained from the buffer gas cell will show that the simulation can precisely reproduce the molecule flux obtained from the cell depending on the buffer gas flux into the cell. This comparison is performed for two different molecule species, CH_3F and ND_3, two different buffer gas species, He and Ne, and different temperature settings. A good fit can be obtained with just one free fit parameter.

With some additional improvements made for the simulations, it is possible to obtain a good fit to experimentally obtained velocity distributions of the molecules. The necessary updates to the calculations will be highlighted and explained. Due to these results, the boosting effect of molecules out of the buffer gas cell can be understood without need to implement hydrodynamic effects.

At the end of chapter 2, I will propose a scheme to use the simulation for an optimization of buffer gas cells that can considerably speed up the current trial-end-error approach. The optimization scheme is explained on the example of finding the optimum cell length for a molecule trapping experiment.

In chapter 3 I will introduce the combination of the cryogenic buffer gas cell with the centrifuge decelerator, the so-called Cryofuge. In the beginning, the apparatus is presented, and the characterization of the quadrupole mass spectrometer is shown in detail. Afterwards, the results of the Cryofuge are presented, showing its versatility to cool and decelerate different molecule species, and to produce a huge flux of slow molecules. The large molecule flux and density in the electric guide is demonstrated by the first observation of dipolar molecule-molecule collisions at temperatures below 1 K. Two different molecule species with different electric dipole moments were studied in detail. A comparison of the results to theoretical calculations and numerical simulations reach a good fit with the empirical data.

The large flux of slow molecules is perfectly suitable to be trapped in an electrostatic trap. The addition of such a trap to the setup is shown in chapter 4. Here, the first trapping of buffer gas cooled and centrifuge decelerated molecules is illustrated. The combination of the system is thoroughly investigated and the trapped molecules samples are characterized. :

In the outlook, I will discuss the immediate improvements made on the setup and the upcoming efforts to improve the control over the molecules. Additionally, the further prospects that may be enabled by the new experiment are considered.

2 Buffer gas cell simulations

In this chapter I will describe simulations performed in order to better understand the properties of the buffer gas cell. The simulations are based on a particle picture with ballistic movement, and no fluid dynamics are regarded. However, using a refined model employing a detailed analysis of collision properties, the boosting effect [MSZ+09] of molecules out of the cell could be reproduced. Moreover, the stochastic thermalization process and the dependence of the molecule flux out of the cell on varying buffer gas densities could be fitted to experimental data. This is shown by comparison of simulated count rates and velocity distributions of molecules with experimental data obtained with our cryogenic buffer gas cell setup. At the end of the chapter, I propose a method to optimize the buffer gas cell. This could significantly shorten the currently used trial-and-error approach. Moreover, it has the prospect to find better parameters than what can be found purely empirically.

2.1 An effusive buffer gas cell

A buffer gas cell is a widely used device to cool molecules, and relies on the simple principle of sympathetic cooling of heavier particles via a buffer gas. But even though the basic idea is straightforward, the details of the dynamics are not well understood. The buffer gas cell can be operated in two fundamentally different regimes: In the limit of low buffer gas densities in the cell, the mean free path is large compared to the exit nozzle of the cell. In this limit, the molecules move ballistically through the cell, performing a random walk. For high buffer gas densities, hydrodynamic effects play a role, and can drastically change the properties of the molecules coming out of the cell. The simulations already available consider the latter [BSH+13, DSL+17], while the work presented here concentrates on the former, effusive regime, up to the point of the onset of boosting, where velocity distributions of molecules are no longer purely effusive, but are altered by molecule-buffer gas collision outside the cell.

A phenomenological explanation of the shape of the velocity distributions of molecules out of the buffer gas cell has been given previously [MSZ+09]. Here, the Maxwell-Boltzmann distribution of the thermalized molecules was adjusted by a factor $\exp(-b/v)$ to exponentially suppress the slow molecules. In this work, b is an arbitrarily chosen parameter that is fitted to the velocity distribution. With this, the approximate shape of the boosted distributions could be analytically described. However, it could

not be used before the molecules were fully thermalized in the buffer gas cell, and relied on a fitting parameter for every measured velocity distribution. For the simulations presented here, a single fit to experimental data is sufficient to describe the properties of the velocity distributions of molecules out a buffer gas cell.

A cryogenic buffer gas cell consists of a cryogenically cooled copper box, the cell. Furthermore, it needs a molecule source, which can be realized , e.g., by an ablation source or a discharge source, but is implemented here as a small hole in the back of the cell where molecules are fed in via a Teflon tube. Vis-à-vis the molecule input is another hole where the cooled molecules exit the cell, the output nozzle. The buffer gas is brought into the cell via eight holes, symmetrically arranged around the axis of the cell. This ensures a homogeneous distribution of the buffer gas.

Due to this geometry, and the small buffer gas density used in the cell, the buffer gas density throughout the cell is spatially constant to good approximation. Due to the large mean free path, hydrodynamic effects do not occur, and therefore the velocity distribution of the buffer gas atoms is spatially constant as well. In such a cell where the conditions for the molecules do not change, the molecule dynamics can be regarded as a random walk. This allows for the visualization via a Gambler's Ruin problem, as it will be explained in the following paragraphs. In the vicinity of the output nozzle, where the mean free path of the molecules is comparable to or even smaller than the nozzle diameter, some deviations of these simple assumptions have to be made, which will be described later.

2.2 Simulation principles

First, the foundations of the simulations will be explained. A simple model based on the one-dimensional Gambler's Ruin problem is presented first, which helps to qualitatively understand the underlying physics. To quantitatively grasp the experimental data, this analytical model is expanded to a microscopic particle model, which traces the path of the molecules in the cell, and is implemented as a numerical Monte Carlo simulation. With some additional refinements, this approach can accurately model count rates and velocity distributions of the buffer gas cooled molecules.

2.2.1 Gambler's Ruin problem

The Gambler's Ruin problem is a century old idea first described by Blaise Pascal [Edw83] who imagines a gambler with a finite amount of capital, out of which he places bets, in which he either doubles or loses his wager. It is easy to see that if it is a fair game and given unlimited time, the gambler will inevitably go broke. However, an additional question arises: Will the gambler gain a predefined amount before he loses all his money? This question can be mapped to the problem of a

molecule in one dimension starting to diffuse from a certain point in the buffer gas cell and performing a random walk trajectory. Can it reach the exit of a buffer gas cell before it will go back to its input position and get lost there? As the cell is three-dimensional, this has to be generalized to the question if the molecule can reach the exit nozzle, or first hits the cell wall, and freezes there.

Fig. 2.1 shows a simplified sketch of the cell. The warm molecules enter the cell from a hole in the center of the left wall of the cell, the exit nozzle is in the center of the wall on the right. We assume that the molecules travel a distance x straight into the cell before they are thermalized and start their random walk. This distance can be written as $x = m \cdot \mathrm{mfp}$ in units of the mean free path mfp of the molecules in the buffer gas environment, which is given by $\mathrm{mfp} = 1/(n \cdot \sigma)$. Here, n is the buffer gas density, and σ the molecule-buffer gas collision cross section. The number m can be interpreted as the number of collisions of a warm molecule with cold buffer gas atoms necessary to thermalize to cell temperature. The length of the cell L_{cell} can be written in units of the mean free path as $L_{\mathrm{cell}} = A \cdot \mathrm{mfp}$, with the dimensionless length of the cell A. For the 1D case, the probability of a molecule to reach the exit is then given by the simple equation

$$P = m/A = m/(L_{\mathrm{cell}} \cdot n \cdot \sigma) \tag{2.1}$$

To correct for the 3D case, we add a factor proportional to the solid angle, under which the molecule sees the exit nozzle with a radius of r from its starting position. The result is then

$$P = \frac{m}{L_{cell} \cdot n \cdot \sigma} \frac{r^2}{\left(L_{cell} - \frac{m}{n \cdot \sigma}\right)^2} \tag{2.2}$$

For simplification we collect the constants as $a = r^2/(4L_{cell}^2)$ and $b = m/(L_{cell} \cdot \sigma)$, and write

$$P = a \frac{b/n}{(1 - b/n)^2} \tag{2.3}$$

Fig. 2.2 shows the Gambler's Ruin model in blue, together with experimental data in black. The same data are plotted inFig. 2.2 a) and b) in linear and logarithmic scale, respectively. Here, the buffer gas density in the cryogenic cell is varied, and the resulting molecule flux is recorded. A more detailed description on how the data is taken is given below. As can be seen, the model reproduces the qualitative behavior of the system for higher densities, where the probability of the molecules to exit the cell is decreasing. This is also seen in experimental data, and can be understood in the model. If the density is high, the molecules are already thermalized close to the input, and need more and more steps on the random walk to reach the exit,

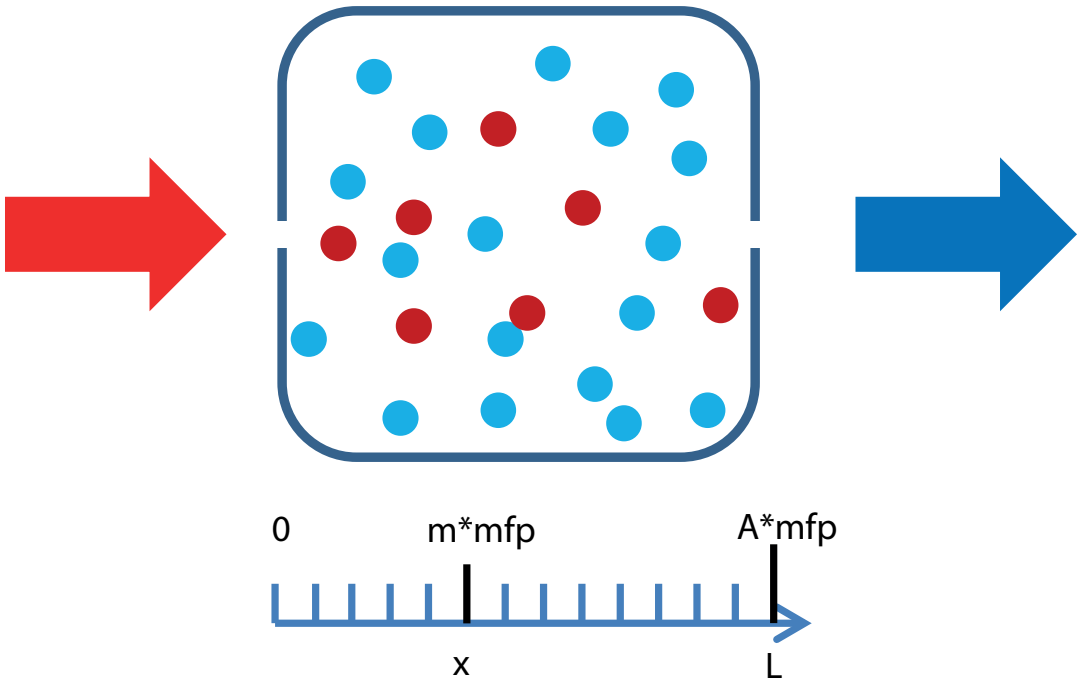

Figure 2.1: Simplified sketch of the buffer gas cell. The molecules enter through the center of the left wall of the cell (red arrow), and propagate towards the right, and can eventually exit the cell through the nozzle in the right wall (blue arrow). The length L_{cell} of the cell can be written in units of the mean free path of the molecules mfp as $L_{\text{cell}} = A \cdot \text{mfp}$. Before the molecules are thermalized, they experience m collisions and travel a distance $x = m \cdot \text{mfp}$ into the cell, where they start the random walk process.

as the mean free path is reduced. For lower densities, however, equation 2.3 shows nonphysical behavior, as it has a pole for $n = b$. In the model, this would be the situation when the molecule is thermalized precisely at the position of the exit nozzle.

Additionally, the number m is not well-defined, and changes stochastically for different realizations, while it is taken as a constant in the Gambler's Ruin problem. Beyond the pole at even lower densities the model cannot hold any more. In the experiment, a buffer gas cell without buffer gas will act as a simple aperture for the molecules, and will result in a finite and constant escape probability as long as n is small, so that the mean free path of molecules is large compared to the length of the cell. Moreover, the Gambler's Ruin can only give insights about the probability of a molecule to reach the exit nozzle, but cannot give any information about the velocity distribution of the molecules. For this, a particle based trajectory simulation is employed. However, at intermediate buffer gas densities, the Gambler's Ruin model is valid, and can give a simple and fast estimation of the escape probability

of molecules out of a buffer gas cell. Additionally, it provides a simple picture why the molecule flux out of the cell changes drastically with changes in the buffer gas density.

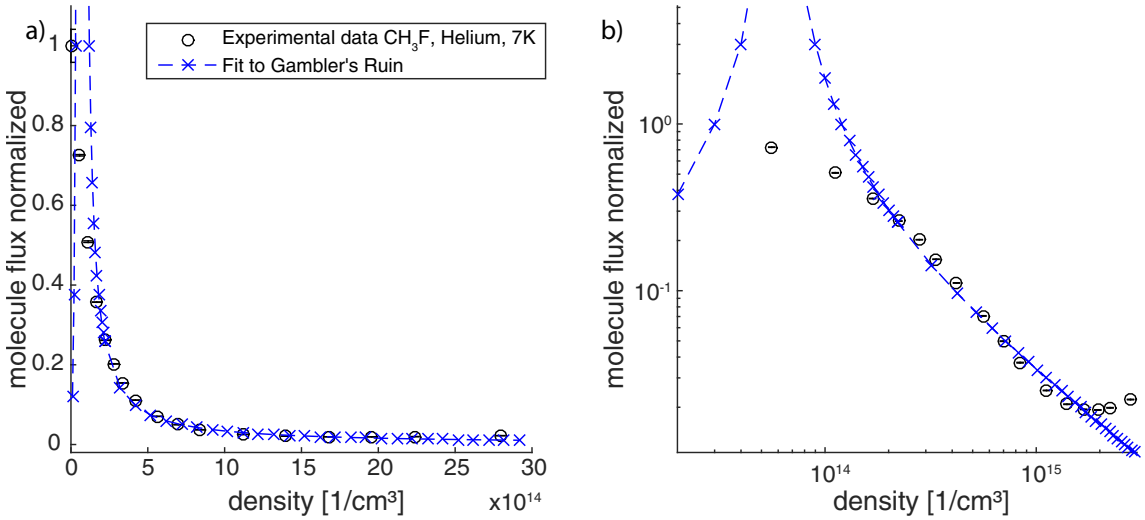

Figure 2.2: Comparison of experimental data and the Gambler's Ruin model, in linear (a) and logarithmic (b) scale. Experimental data for a cell temperature of 7 K are shown as black circles, including 1σ error bars. The according Gambler's Ruin model is shown as blue crosses, with a dashed line to guide the eye. The parameters a and b are adjusted to fit the experimental data.

2.2.2 Monte Carlo simulation

For a more conclusive simulation the Monte Carlo method is used. The underlying idea is to simulate single molecule trajectories one by one, while starting conditions and scattering parameters are randomly chosen according to their occurrence probability.

Underlying assumptions

As a basis for the simulation, some assumptions are made:

- Molecules entering the cell have a velocity distribution according to Maxwell-Boltzmann. The input temperature used in the simulation is the one read from the temperature sensor at the molecule input line next to the cell input. This means that the molecules do not enter the cell with a directed motion, but diffuse from the input hole.
- Buffer gas atoms have a velocity distribution according to Maxwell-Boltzmann. The temperature is given by the cell temperature measured in the experiment.

The temperature is spatially constant throughout the cell volume. This is a good approximation, as the buffer gas density is typically higher than the molecule density, and therefore the warm molecules do not have a large impact on the buffer gas atom sample.

- The buffer gas density is homogeneous throughout the cell. The cell is constructed with eight symmetrically arranged buffer gas inputs to achieve a homogeneous density. Hydrodynamic effects that could locally vary the density are not considered. We will see that the validity of that assumption breaks down for high densities, when the simulation results deviate from experimental data.
- Molecule-molecule collisions are not considered. As soon as the molecules have entered the cell, the molecule density is small compared to the buffer gas density.
- Molecules that hit the cell walls are lost from the simulation. In reality, molecules would stick and freeze when hitting the cell wall, as their freezing point is a lot higher than the cell temperature for all parameters considered here. Possible reflections of molecules off the walls are ignored.
- The internal structure of the molecules is not considered. All the collisions will be considered purely elastic, cooling of internal degrees of freedom can therefore not be simulated.
- The scattering angle between a molecule and a buffer gas atom is distributed homogeneously in 4π in the center of mass frame. This approximation is acceptable, as many collision will happen for each molecule diffusing through the cell. Therefore, any preferred scattering direction is averaged out before a molecule reaches the output nozzle of the cell.
- The collision cross section does not change while the molecule propagates. A change in collision cross section, for example due to the decreasing collision energy as the molecules are decelerated, is not considered.
- The collision cross section for the simulation is a priori arbitrarily chosen. As it only appears in combination with the buffer gas density to define a mean free time between two collisions, it can be used as a free fitting parameter when comparing the numerical to the empirical results.

Fig. 2.3 shows the buffer gas cell that is used for the experiments shown in this chapter, and which is reproduced in the simulations. The same buffer gas cell is also employed for the subsequent experiments of guiding, decelerating and trapping of molecules. The relevant parameters are the cell temperature T_{cell}, the molecule line temperature T_{mol}, the length of the cell $L_{\mathrm{cell}} = 2\,\mathrm{cm}$, its diameter $d_{\mathrm{cell}} = 1.7\,\mathrm{cm}$, and the radius of the exit nozzle $r_{\mathrm{nozzle}} = 1\,\mathrm{mm}$. The size and position of the QMS is not directly relevant for the simulation, but plays an important role when comparing the simulation results to experimental data. As only molecules in a certain solid

angle can be detected, only molecules leaving the cell in this angle in the simulation will be considered.

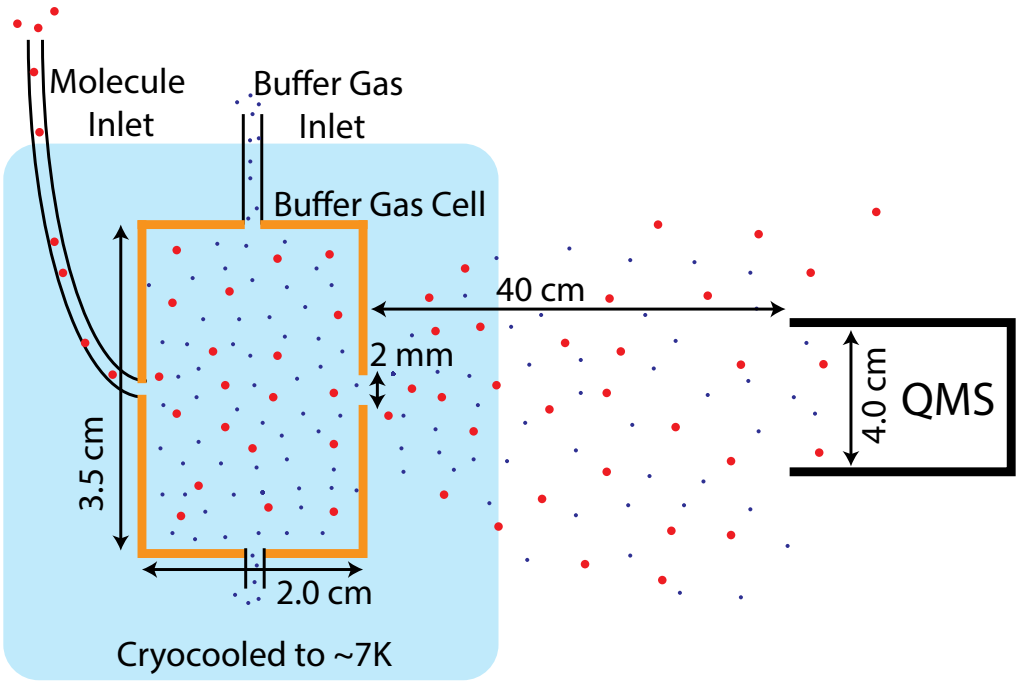

Figure 2.3: Schematic drawing of the buffer gas cell as used for the count rate measurement for varying buffer gas densities. The relevant sizes are shown. The drawing is not to scale. For the velocity distribution measurements, a 90° guide with a radius of 20 cm is added after the exit nozzle, and the QMS is placed after this guide.

Simulation process

I will now describe the general scheme for the simulations. The refinements of the simulation necessary to get velocity distributions that match the experimental data are explained in the next section.

The molecules are treated one by one. Before the trajectory starts, the molecule starting velocity is randomly picked with a probability following a Maxwell-Boltzmann distribution. The direction is randomly selected from a solid angle of 2π. The starting position for all molecules is the center of the left wall of the cell.

For the first step of the molecules, the current mean free path r_{mfp} is calculated from the constant mean free time between two collisions. The actual distance r_{path} the molecule travels before a collision occurs is then randomly selected with a probability following the Beer–Lambert law, $P(r_{\mathrm{path}}) = 1/r_{\mathrm{mfp}} \cdot \exp(-r_{\mathrm{path}}/r_{\mathrm{mfp}})$.

Then, the molecule is propagated in a straight line along its velocity direction for the distance r_{path}. For the collision process, a velocity and direction of the scattering partner is chosen. It is picked randomly from a Maxwell-Boltzmann distribution with the temperature of the cell and the mass of the buffer gas atoms. The scattering process itself is considered elastic, and therefore kinetic energy and momentum are conserved. The one free parameter in the process, the scattering solid angle in the center of mass reference frame, is randomly chosen from a homogeneous distribution over 4π. After the scattering, the molecule has obtained a new velocity vector, and the process starts over. The position and velocity of the molecule after each scattering process is recorded, so that a full trajectory of all molecules can be visualized. Saving the full trajectories can be omitted to speed up the simulation and to reduce memory requirements, if only the final position and velocity of the molecules is of interest.

After each step, the position of the molecule is examined. As long as the molecule is inside the cell volume, the free motion-collision process is repeated. In case the molecule is outside the cell volume, the trajectory of the previous step is checked to determine if the molecule left the cell through the exit nozzle, or is lost on the cell wall. The result of this check, together with the molecule's last position, velocity vector, and the number of collision the molecule has experienced, is saved.

Refinements

The simulation as described in the previous few paragraphs is sufficient to understand the probability of a molecule to leave the cell, and thereby the count rate of the QMS, for a varying buffer gas density. However, to correctly reproduce the velocity distribution of molecules leaving the cell, some refinements are necessary.

As a first step, we take a closer look at the nozzle region, were the boosting effect arises. As described above, molecule - buffer gas collision happen in the same way just inside the exit nozzle and further inside the cell. Outside the nozzle, the collisions would stop immediately. This is obviously unphysical, as buffer gas atoms leave the buffer gas cell together with the molecules. Therefore, the collision probability inside the nozzle should decrease as trajectories of buffer gas atoms from the nozzle cannot appear, and molecules still collide outside the nozzle with atoms coming out of the cell.

To implement this in the simulation, an additional check before the collision process is integrated, whenever the molecule is closer to the nozzle than one mean free path of a buffer gas atom inside the buffer gas environment [Bon64]. After the random determination of the buffer gas velocity vector, it is checked if the atom comes from the direction of the nozzle. If that is the case, the atom is ignored, the collision is omitted, and the molecule propagates another mean free path before the next collision can occur.

If the molecule exits the cell through the nozzle, the collision - propagation process is continued. However, a collision is only determined to occur if the buffer gas atom is coming from the nozzle area. This effectively leads to boosting, as molecules are most likely hit from behind, and are accelerated away from the cell. This process continues until the molecule reaches a distance d_{boost} of 2.5 cm from the cell. The precise size of this region has an negligible effect on the outcome of the simulation, as collisions naturally die out as $\sim r_{\mathrm{nozzle}}^2/d_{\mathrm{boost}}^2$ far away from the cell, when the solid angle covered by the nozzle area becomes small. Therefore, the fraction of collisions missed due to the finite value of d_{boost} is well below 1%.

Distribution of relative velocities

The mean free path of the molecule inside the buffer gas environment changes according to its velocity. For example, even a molecule at standstill would collide with a buffer gas atom eventually due to the motion of the atoms, therefore, the corresponding mean free path of molecules at standstill would be zero. Therefore, the mean free path of a molecule depends its velocity v_{mol} . Compared to the mean free path averaged over all molecule velocities $\mathrm{mfp}_{\mathrm{avg}} = 1/(n \cdot \sigma)$, it is scaled by the ratio of v_{mol} to the relative velocity $\overline{v_{\mathrm{rel}}}(v_{\mathrm{mol}})$ between the molecule the buffer gas atoms. It can then be written as:

$$\mathrm{mfp}(v_{\mathrm{mol}}) = \frac{v_{\mathrm{mol}}}{\overline{v_{\mathrm{rel}}}(v_{\mathrm{mol}})}\,\mathrm{mfp}_{\mathrm{avg}} \tag{2.4}$$

Therefore, we first need to find $\overline{v_{\mathrm{rel}}}(v_{\mathrm{mol}})$, which can be calculated by

$$\overline{v_{\mathrm{rel}}}(v_{\mathrm{mol}}) = (\pi{\cdot}w)^{-3/2} \int_{-\infty}^{\infty} \mathrm{d}v_x\,\mathrm{d}v_y\,\mathrm{d}v_z\,\sqrt{v_x^2+v_y^2+(v_z-v_{\mathrm{mol}})^2}\,\exp\left(\frac{-v_x^2-v_y^2-v_z^2}{w}\right) \tag{2.5}$$

Here, v_{mol} is defined in z-direction, without loss of generality. w describes the width of the Maxwell-Boltzmann distribution and is given as $w = \frac{2k_B T_{\mathrm{BG}}}{m_{\mathrm{BG}}}$, where T_{BG} is the temperature of the buffer gas, m_{BG} the mass of a buffer gas atom, and k_B the Boltzmann constant. $\sqrt{v_x^2+v_y^2+(v_z-v_{\mathrm{mol}})^2}$ is the relative velocity of the molecule and an atom of velocity (v_x, v_y, v_z). The Maxwell-Boltzmann distribution of the buffer gas atoms is given by $(\pi \cdot w)^{-3/2} \exp\left(\frac{-v_x^2-v_y^2-v_z^2}{w}\right)$. The integral can be solved analytically by splitting it up into transversal and longitudinal velocity components, and separately integrating the parts for $v_z > v_{\mathrm{mol}}$ and $v_z < v_{\mathrm{mol}}$. The final result can then be written as

$$\overline{v_{\mathrm{rel}}}(c) = \sqrt{w}\left(\frac{e^{-c^2}}{\sqrt{\pi}} + c \cdot \mathrm{erf}(c) + \frac{1}{2c} \cdot \mathrm{erf}(c)\right) \tag{2.6}$$

where c is defined as $c = v_{\mathrm{mol}}/\sqrt{w}$, and $\mathrm{erf}(x)$ is the error function $\mathrm{erf}(x) = \frac{2}{\sqrt{\pi}} \int_0^x e^{-t^2}\,\mathrm{d}t$. Fig. 2.4 shows $\overline{v_{\mathrm{rel}}}/\sqrt{w}$ for varying c in blue. For small molecule velocities, $v_{\mathrm{mol}} \to 0$, $c \to 0$, $\overline{v_{\mathrm{rel}}}$ goes to $2\sqrt{w}/\sqrt{\pi}$, which is the mean speed of the buffer gas atoms, as expected. For high v_{mol}, $c \gg 1$, the velocity of the atoms plays less and less of a role, and $\overline{v_{\mathrm{rel}}}$ approaches v_{mol}. The curve $\overline{v_{\mathrm{rel}}} = v_{\mathrm{mol}}$ is shown in red for comparison. The deviation at small c and therefore small v_{mol} reduces the mean free path of slow molecules.

Including this effect in the simulation has a small impact on thermalization in the cell, as collisions appear spatially homogeneously in an homogeneous environment. However, outside the nozzle, this effect is essential to create the boosting effect. The mean free path of the molecules depends on their velocity according to equation 2.4, this means slower molecules undergo more collision events while transversing the same distance. As described before, in this region molecules are predominantly hit by atoms from behind. Therefore, the slow molecules experience a much stronger acceleration effect in the nozzle region due to their reduced step size $\mathrm{mfp}(v_{\mathrm{mol}})$.

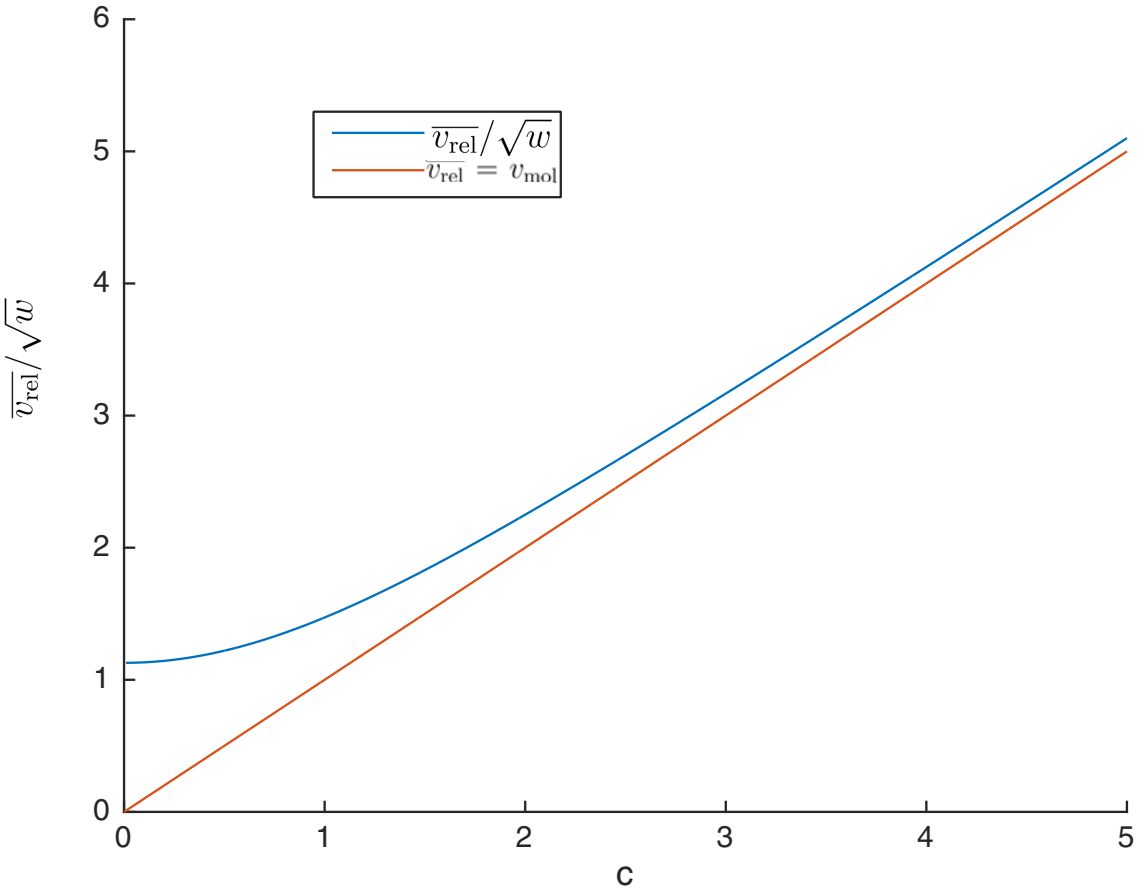

Figure 2.4: Unitless average relative velocity versus $c = v_{\mathrm{mol}}/\sqrt{\sigma}$. The asymptote $\overline{v_{\mathrm{rel}}} = v_{\mathrm{mol}}$ is shown in red.

Another effect implemented in the simulation is the alteration of the velocity distri-

bution of buffer gas atoms in a collision compared to the straightforward Maxwell-Boltzmann distribution. After thermalization, the molecules in the cell are on average slower than the buffer gas atoms due to their higher mass. The collision probability between a molecule and a buffer gas atom depends linearly on their relative velocity; e.g., for zero relative velocity, two particles can never collide. Therefore, the slow molecules collide with faster buffer gas atoms more often. This effect is implemented in the simulation, and shown in Fig. 2.5. Here, the histogram of the velocity of buffer gas atoms participating in a collision is shown in red. As comparison, the Maxwell-Boltzmann distribution of the buffer gas atoms is given in green. The distribution in the simulation is clearly showing an excess of fast atoms compared to the Maxwell-Boltzmann distribution, while the slow buffer gas atoms are missing.

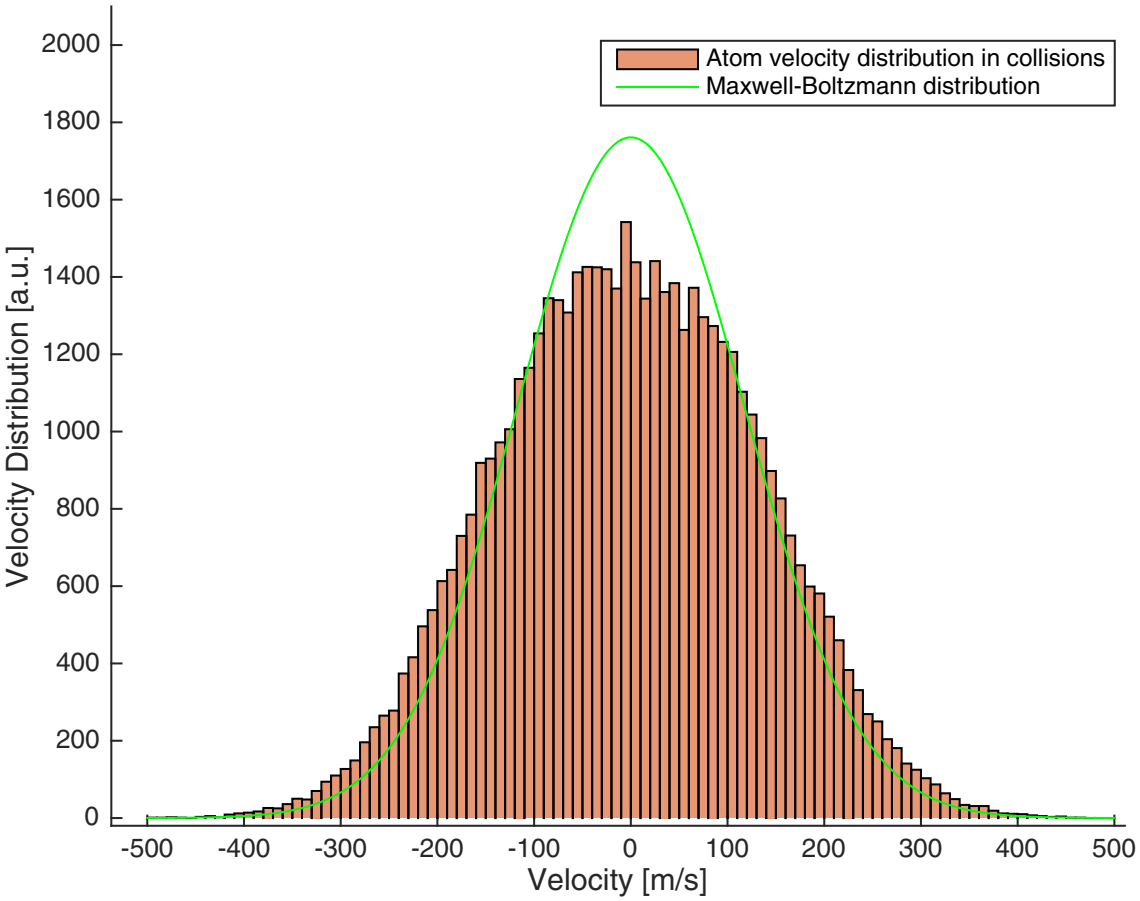

Figure 2.5: Histogram of the velocity of buffer gas atoms participating in a collision. The Maxwell-Boltzmann distribution of the atoms in the buffer gas cell is shown in green as comparison. Due to the dependence of the scattering rate on the relative velocity of two particles, faster atoms are favored in collisions compared to slower ones.

Note that all these refinements do not include fluid dynamical effects. In the hydrodynamic regime, the properties of the buffer gas atoms after the nozzle would

be drastically altered, compared to the assumption of a effusive source as used here [TW77]. Most importantly, it would lead to an increase of the mean forward velocity of the buffer gas. This would directly lead to an additional acceleration of the molecules. This regime is not implemented in the simulation described here, and the simulated velocity distributions cannot be brought to fit the distributions measured at high buffer gas densities. For simulations in this regime, refer to [BSH$^+$13, DSL$^+$17]. However, the long standing goal to understand the depletion of very slow molecules in a beam even at moderate buffer gas densities can be achieved, as will be shown in the next sections.

2.3 Results of the simulation

I will now present the results of the simulation. First, Fig. 2.6 and Fig. 2.7 show trajectories of molecules produced by the simulation inside the cell, for low and high buffer gas densities, respectively. The molecules start at origin of the coordinate system, $(0, 0)$, the exit nozzle is at $(3, 0)$, in the center of the opposite wall of the cell.

For the moderate buffer gas density shown in Fig. 2.6, the mean free path of the molecules is still large compared to the output nozzle, but smaller than the cell length. Therefore they travel about 0.5 cm into the cell before they are fully thermalized. Afterwards, they diffuse through the cell, until their trajectories terminate at a cell wall. In this example, one of the molecules could exit the cell, and would be counted as successfully cooled. A typical trajectory is shown in black for clarity.

The picture looks very different for high buffer gas densities as shown in Fig. 2.7. Here, the same number of trajectories is depicted. However, the mean free path of the molecules is very short, and therefore, they thermalize very close to the entry nozzle. As expected from the naive Gambler's Ruin problem, most molecules get lost at the cell walls close to the entry nozzle. Only few trajectories diffuse further than 0.5 cm into the cell, and it is evident that the probability to exit the cell is greatly reduced. For higher and higher buffer gas densities, more and more collision events appear, and consequently, the computing time increases. However, even for the highest densities considered, the simulation can still be done on a standard office PC in reasonable time, with a computation time of up to a few days.

When comparing the results for the two different densities, it becomes apparent that as soon as full thermalization is achieved, higher buffer gas densities will only reduce the molecule flux out of the cell, without a beneficial effect. Therefore it is important to chose the density correctly for the according experimental parameters to maximize the flux of thermalized molecules out of the cell.

To visualize the thermalization effect of the molecules diffusing into the cell, Fig. 2.8 shows the evolution of the molecule velocity versus the number of molecule-buffer gas collisions. Starting from the given Maxwell-Boltzmann distribution, the average

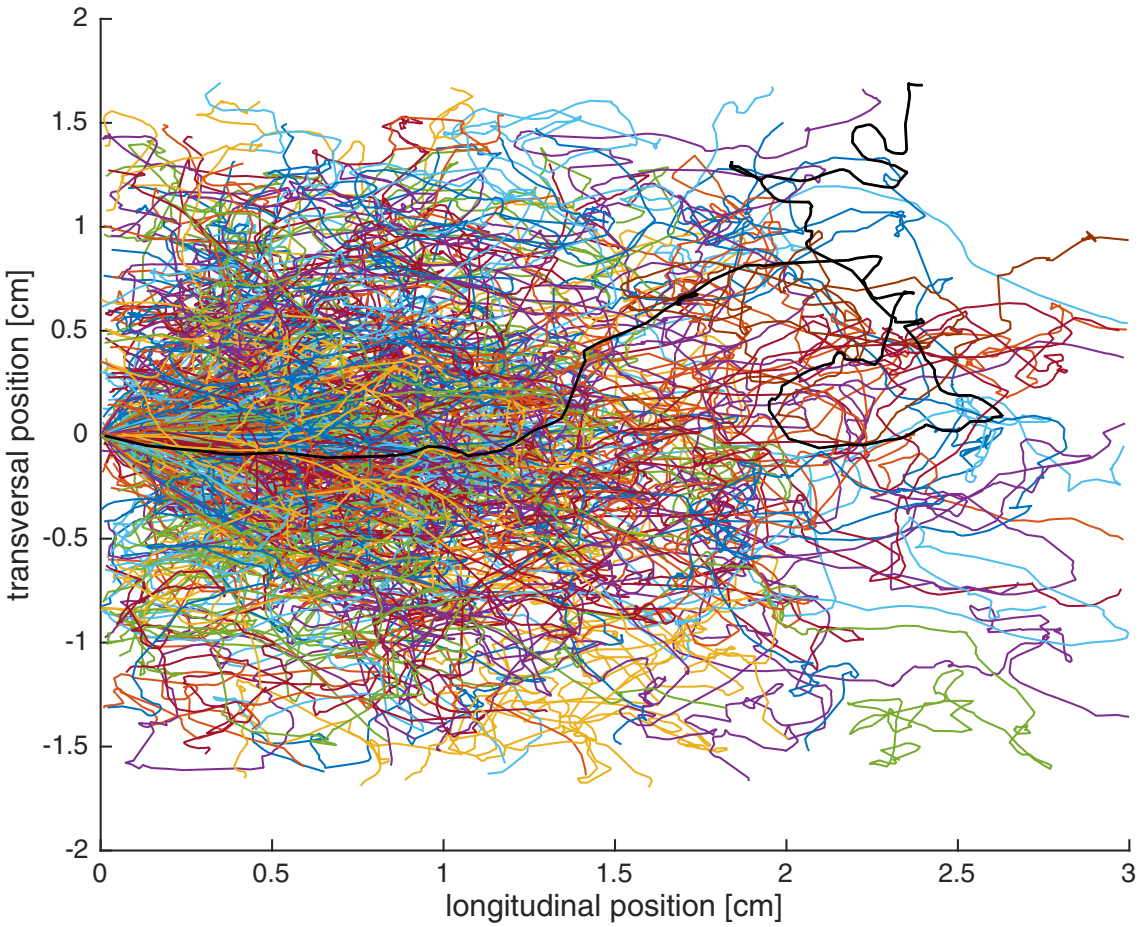

Figure 2.6: Simulated molecule trajectories inside the buffer gas cell for moderate buffer gas densities. Molecules enter the cell at position $(0, 0)$. The exit nozzle of the cell is located at $(3, 0)$. A typical trajectory is shown in black for clarity.

velocity decreases quickly as the molecules make their way through the cell and are decelerated by the cold buffer gas atoms. The inset shows the standard deviation of the velocity after each collision. After about 20 collisions, the molecule sample is fully thermalized, and the velocity distribution and its standard deviation does not change any more. This process does not depend on the buffer gas density, but is only determined by the molecule starting temperature, the buffer gas temperature, and the masses of the molecules and the buffer gas atoms.

The thermalization of molecules in the cell can also be seen from the varying velocity and angle distributions of molecules coming out of the cell at different buffer gas densities. This is depicted in Fig. 2.9. For very small buffer gas densities, we expect no collisions between molecules and buffer gas atoms, and the velocity distribution after the cell should be the Maxwell-Boltzmann distribution according to the molecule temperature at the start of the simulation. This is shown in Fig. 2.9a), where the blue histogram is the velocity distribution of the molecule sample com-

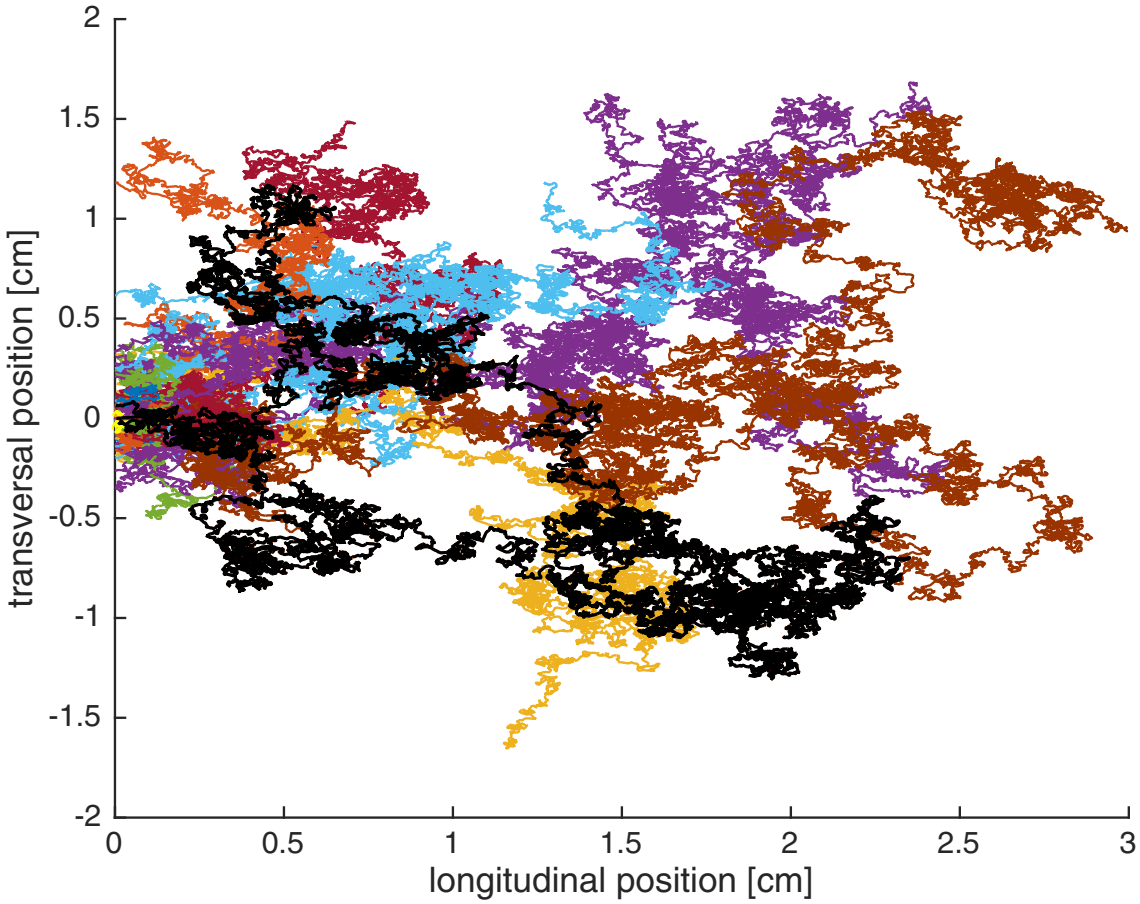

Figure 2.7: Simulated molecule trajectories inside the buffer gas cell for high buffer gas densities. Molecules enter the cell at position $(0, 0)$. One of the few trajectories that reach more than 0.5 cm into the cell is shown in black. A more typical trajectory that barely reaches 0.1 cm into the trap and is hardly visible close to the entry nozzle is plotted in bright yellow.

ing out of the cell, and the green solid line depicts the original Maxwell-Boltzmann distribution of the molecules. The angle distribution of molecules coming out of the cell is shown in Fig. 2.9b), and clearly shows the aperture effect of the nozzle, so that molecules can only leave the cell in a small solid angle.

For higher buffer gas densities, the molecules coming out of the cell are more and more slowed down, as visible in Fig. 2.9c) and e). The according angle distributions are shown in Fig. 2.9d) and f). By comparison of the velocity distributions to the Maxwell-Boltzmann distribution of the molecules at cell temperature shown by the red line, it the molecules are clearly not fully thermalized yet. The angle distribution widens up as the molecules collide with more and more buffer gas atoms on the way to the exit nozzle, so that it acts as an effusive source instead of as a aperture.

When further increasing the buffer gas density, the molecules undergo enough col-

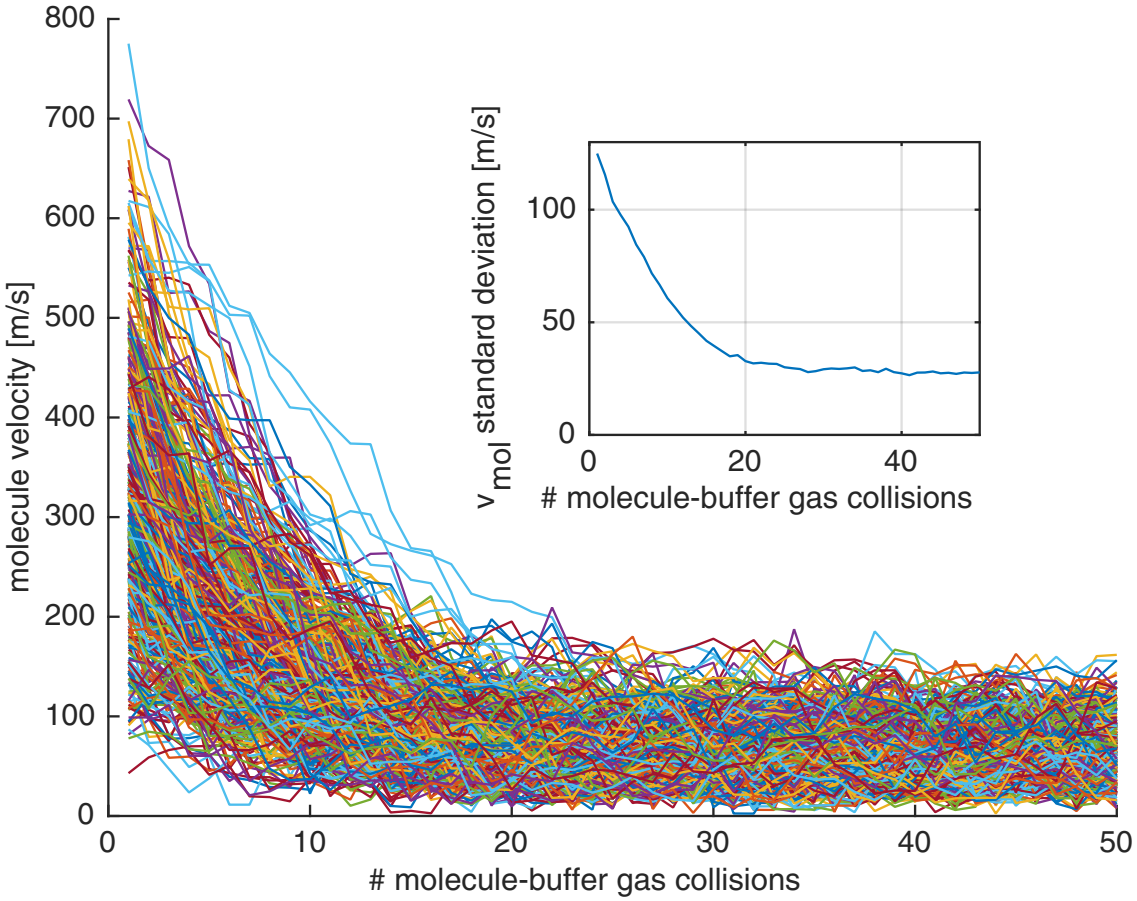

Figure 2.8: Velocities of molecules in the simulation versus the number of collisions they undergo. The inset shows the standard deviation of the velocity after each collision. The thermalization effect is clearly visible by the decrease of the average velocity and the standard deviation up to about 20 collisions.

lisions with the buffer gas atoms to fully thermalize with the atoms. Therefore, their velocity distribution as shown in Fig. 2.9g) is narrow, and has a even smaller mean velocity. Again, the red line shows a Maxwell-Boltzmann distribution of the molecules at cell temperature, which fits accurately to the simulation. Therefore, the molecules in this simulation are well thermalized. The distribution does not display a boosting effect yet. The angle distribution of this molecule sample is shown in Fig. 2.9h). Here, a broad distribution is visible, as expected it closely resembles the distribution of a gas coming from an effusive source as shown in magenta.

For the highest buffer gas densities considered here, the velocity distribution of the molecules is shown in Fig. 2.9i). Here the simulation output does not fit the Maxwell-Boltzmann distribution of the non-thermalized molecules at starting temperature. Likewise, it does not fit the thermalized distribution as shown in red. The average velocity is clearly increased, and the slowest molecules are missing. This is the effect of boosting out of the cell at high buffer gas densities. The black curve shows the

velocity distribution of buffer gas atoms at cell temperature. As the molecules are slower than the atoms, they are accelerated after leaving the cell. This is explained in greater detail later in this chapter. The angle distribution for the molecules at highest buffer gas density is shown in Fig. 2.9j). A modest narrowing effect on the molecule beam compared to the simple effusive source is evident. This comes from the fact that boosting happens predominantly in forward direction, leading to smaller escape angles.

2.4 Comparison to experimental results

To confirm that the simulation can be trusted, we compare its outcome to experimental data. We will check key properties of the cell, the flux of molecules coming out of the cell, and the velocity distribution of these molecules.

2.4.1 Molecules flux from the cell

As a first test, we use a QMS in front of the cell in a distance of 40 cm and a detection area with a diameter of 2 cm to detect the molecule flux out of the cell when varying the buffer gas flux into the cell. For this measurement, no electrical guide was installed. The velocity distribution of the molecules was not measured. This experiment was repeated for two different molecule species, CH_3F and ND_3, two different buffer gases, helium and neon, and different cell temperatures.

Fig. 2.10 shows the molecule flux out of the cell as detected by the QMS, for varying buffer gas flux through the cell up to 0.8 sccm. The molecule flux of CH_3F into the cell was kept constant at 0.02 sccm. The molecule input tube temperature was stabilized to 140 K, and the cell temperature is set to 30 K. The data point for 0 sccm helium flux was taken before the buffer gas flux was switched on. Between recording the molecule flux for the different buffer gas flux values, the system was left to stabilize at the new buffer gas flux. To avoid a hysteresis effect of about 5%, the buffer gas flux was scanned from low to high as well as from high to low, and the mean value of the resulting molecule flux is shown here. The molecule flux is monotonously decreasing with the buffer gas flux, as expected. Measured data points are given with one sigma error bars, the solid line is a guide to the eye.

The next step is to compare this data to the simulation results. To be able to relate the two data sets, we normalize both curves to the maximum count rate, when no buffer gas is in the cell. Additionally, we use one free fit parameter, to connect the buffer gas density n to the mean free path mfp of the molecules in the buffer gas environment of the simulation. This relation is given, as mentioned before, as $\text{mfp} = 1/(n * \sigma)$. Therefore, we can assign an effective collision cross section σ as fit parameter. However, it is important to keep in mind that this value is based on the assumption of fully elastic, homogeneous, hard sphere collisions. When comparing

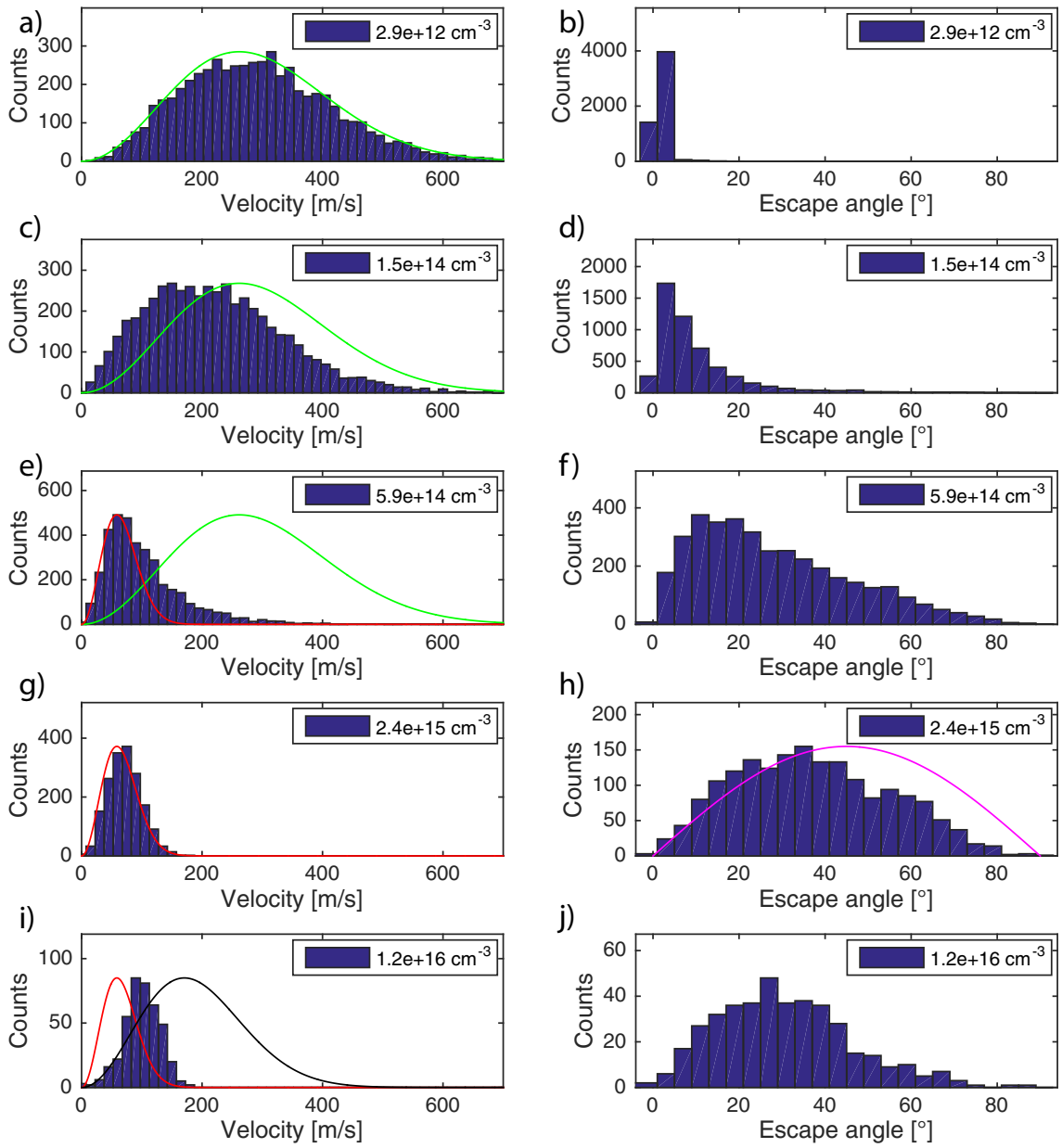

Figure 2.9: Simulated velocity distributions (a, c, e, g, i) and angle distributions (b, d, f, h, j) of molecules coming out of the buffer gas cell at increasing buffer gas densities from top to bottom. The green lines in a), c) and e) show the Maxwell-Boltzmann distribution of the molecules at starting temperature. The red lines in e), g) and i) show the Maxwell-Boltzmann distribution of the molecules at cell temperature. The black line in i) shows the Maxwell-Boltzmann distribution of the buffer gas atoms at cell temperature. The magenta line in h) shows the angle distribution expected for a totally effusive source. The effect of increasing number of collisions between molecules and buffer gas atoms is easily visible. Further details are given in the text.

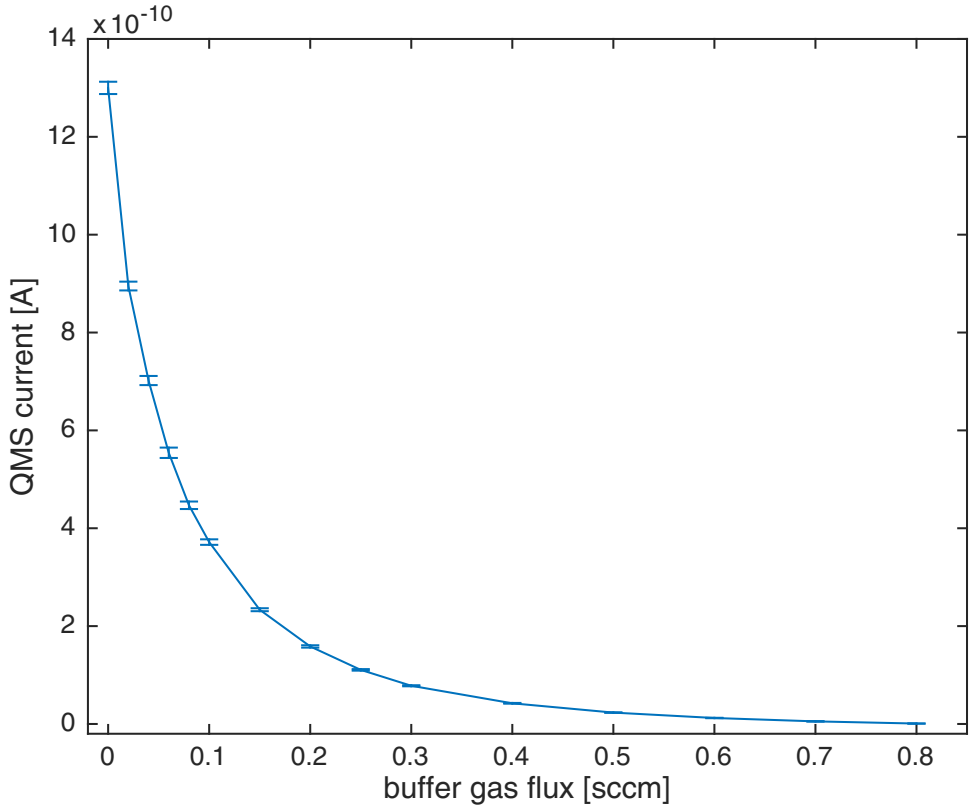

Figure 2.10: QMS signal for molecules depending on the buffer gas flux into the cell. Data is given with one sigma error bars, connecting line is a guide to the eye.

to other collision models that predict a large preference on forward scattering, like the Eikonal approximation, or include inelastic effects, the value of the total collision cross section can differ.

The result of the fit is shown in Fig. 2.11. Fig. 2.11 a) and Fig. 2.11b) show the same set of data, in a linear scale, and in a double logarithmic scale, respectively. The data of Fig. 2.10 is shown as green circles, the density is from simple calculations that transfer the buffer gas flux to a density in the cell. The fitted simulation is shown as red crosses, the dashed lines are connecting lines to guide the eye. The fitting of σ effectively introduces a stretching or compression of the abscissa. The fit results in a cross section $\sigma_{CH_3F-He,30K} = 2.9 \times 10^{-15}\,\mathrm{cm}^2$.

The same experiment and simulation was repeated for a smaller cell temperature of 7 K while keeping the rest of the experimental parameters unchanged. Here, the experimental data and the simulation is shown as black circles and blue crosses, respectively. It can easily be seen that for a lower buffer gas temperature, a higher density is necessary to create the same decrease in molecule count rate. However, this is a consequence of the changed collision dynamics, and the collision cross section

from the fit is almost identical, $\sigma_{CH_3F-He,7K} = 3.0 \times 10^{-15}\,\mathrm{cm}^2$.

In this data, the break down of the ballistic approximation with homogeneous buffer gas density is visible at the highest buffer gas densities. Here, hydrodynamic effects can enhance the extraction of molecules out of the cell, as seen in in Fig. 2.11b). This effect cannot be explained by the model used in the simulation. In the fit to obtain $\sigma_{CH_3F-He,7K}$, these highest buffer gas density points are excluded.

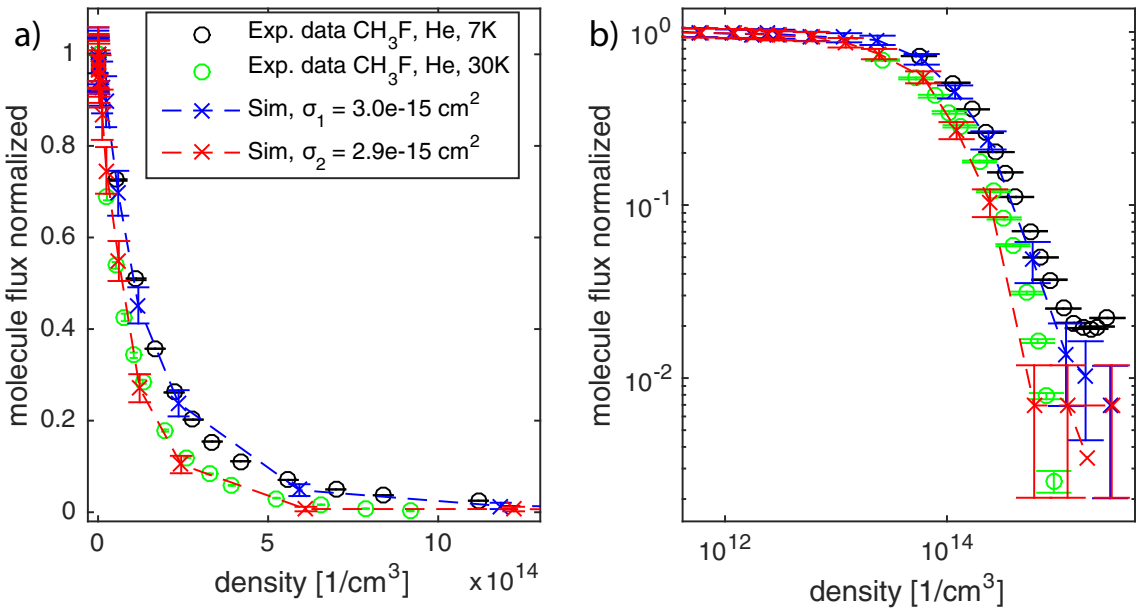

Figure 2.11: Comparison of experimental data and simulation, in linear (a) and logarithmic (b) scale. Experimental data for a cell temperature of 7 K and 30 K are shown as black and green circles, respectively, including 1σ error bars. The according simulation results are shown as blue and black crosses, respectively, with a dashed line to guide the eye. The simulation is scaled horizontally to fit the experiment, and to assign a collision cross section.

The same type of measurements and simulation were also performed for different settings, namely for ND_3 in an helium environment at different temperatures, and CH_3F in a neon buffer gas. The corresponding data and simulation results are shown in Fig. 2.12 and Fig. 2.13, respectively. The collision cross sections resulting from these fits are given in in Tab. 2.1. For the measurements with ND_3, the starting temperature of the molecules was set to 285 K to avoid freezing. For ND_3, the dependence of the cross section on the temperature appears to be much stronger, as it drops by more than a factor of 2 when increasing temperature from 8 K to 47 K. For the collision measurement between CH_3F and Ne, the fitted cross section was reduced compared to the cross section between CH_3F and He.

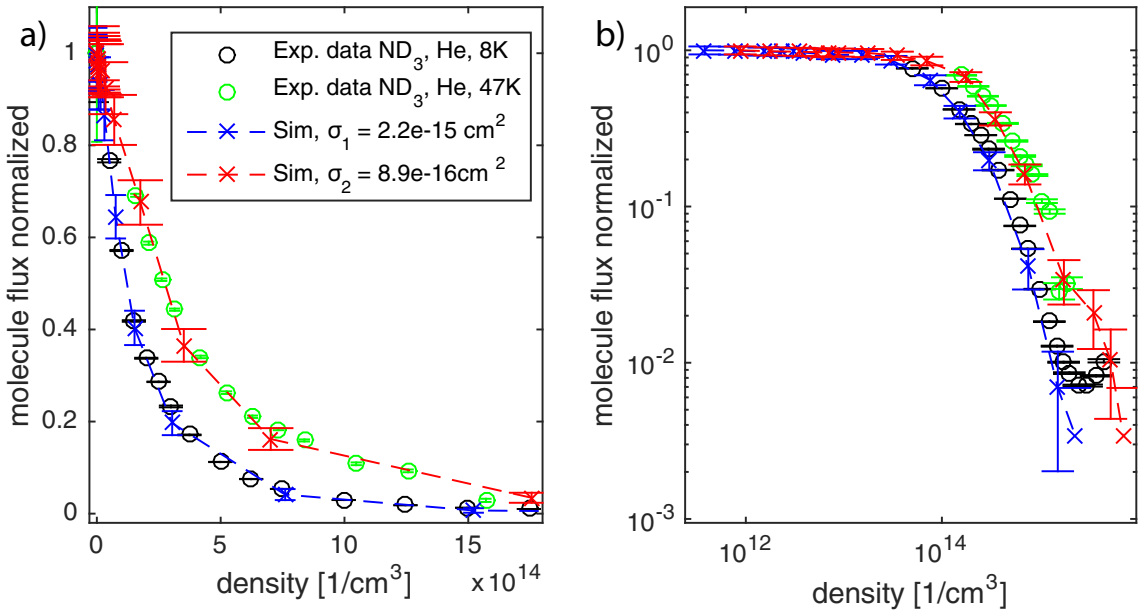

Figure 2.12: Comparison of experimental data and simulation, in linear (a) and logarithmic (b) scale. Experimental data for a cell temperature of 8 K and 47 K are shown as black and green circles, respectively, including 1σ error bars. The according simulation results are shown as blue and black crosses, respectively, with a dashed line to guide the eye. The simulation is scaled horizontally to fit the experiment, and to assign a collision cross section.

2.4.2 Velocity distributions

Another important benchmark for the simulations are the velocity distributions that can be derived from it. Therefore, we install a bent quadrupole guide with a radius of 20 cm behind the cell nozzle to separate the molecule beam from the helium, and measure the velocity distribution by time-of-flight (TOF). Of course, the velocity distribution after guiding around a bend is not the same as after the cell due to the filtering effect, as described in sec. 3.1.1, and in more detail in [SvBM+09, Mot09, Jun05, vBSM+09]. However, with the help of Monte Carlo trajectory simulations we can deduce the velocity distribution at the entry of the guide that is necessary to produce the distribution measured after. The detailed description of these simulations is given in [WGZ+16]. We can then compare empirical and numerical results at the guide entrance.

The following simulations and measurements were performed for CH_3F cooled by helium at a cell temperature of 7 K. Fig. 2.14 shows the simulated and measured velocity distributions for small buffer gas density in red and blue, respectively. Both curves are normalized. To set the correct mean free path of the molecules in the simulation according to the buffer gas density in the experiment, the result of the fit as shown in Fig. 2.11 was used. The Maxwell-Boltzmann distribution for a molecule ensemble fully thermalized to the cell temperature is shown in pink, the distribution

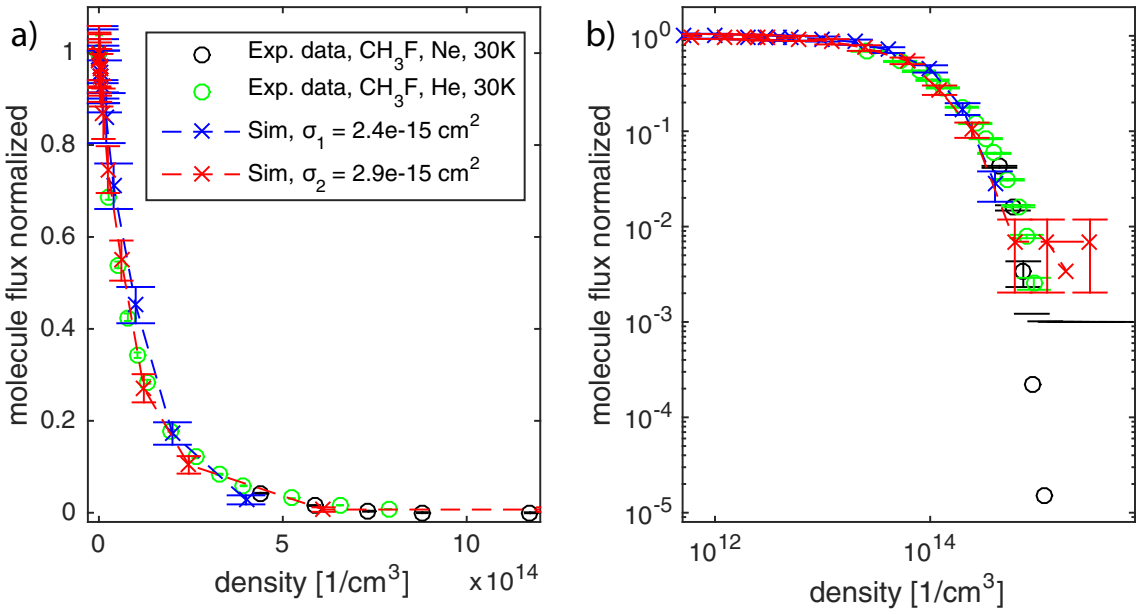

Figure 2.13: Comparison of experimental data and simulation, in linear (a) and logarithmic (b) scale. Experimental data for a cell temperature of 30 K for a buffer gas of neon and helium are shown as black and green circles, respectively, including 1σ error bars. The according simulation results are shown as blue and black crosses, respectively, with a dashed line to guide the eye. The simulation is scaled horizontally to fit the experiment, and to assign a collision cross section.

of the hot molecules entering the cell in cyan. Here, there are not enough collision events per molecule for a complete thermalization. There is no boosting visible, as molecules below $20\,\mathrm{m\,s^{-1}}$ are still present, and the peak of the distribution is well below $100\,\mathrm{m\,s^{-1}}$. To be able able to understand the shape of the velocity distribution for these low velocities is particularly important, if a buffer gas cell is built to generate molecules that are trappable without further deceleration steps.

Fig. 2.15 shows the simulated velocity distribution obtained for higher buffer gas densities in red compared to the experimental data in blue. The green line shows the most probable velocity of the helium atoms in the distribution used for the simulation. In reality, the helium atoms accelerate out of the cell due to hydrodynamic effects, and would amplify the boosting effect. This, however, is not included in the simulation. Therefore, the density shown in Fig. 2.15f) was the highest one used, as faster boosting cannot be reproduced with this model.

To achieve the fit as shown in Fig. 2.15, the mean free path in the simulation has to be adjusted compared to the count rate and thermalization measurements shown before. This fit results in a collision cross section of about $1.5 \times 10^{-14}\,\mathrm{cm^2}$, different compared to the $3.0 \times 10^{-15}\,\mathrm{cm^2}$ as given in Tab. 2.1. This reason for this difference is not fully understood, but a possible explanation is that the simulation uses a simple, hard sphere collision model, and the mismatch between the model and

Settings	Collision cross section σ
CH_3F + He, 7 K	$3.0 \times 10^{-15}\,\mathrm{cm}^2$
CH_3F + He, 30 K	$2.9 \times 10^{-15}\,\mathrm{cm}^2$
ND_3 + He, 8 K	$2.2 \times 10^{-15}\,\mathrm{cm}^2$
ND_3 + He, 47 K	$8.9 \times 10^{-16}\,\mathrm{cm}^2$
CH_3F + Ne, 30 K	$2.4 \times 10^{-15}\,\mathrm{cm}^2$

Table 2.1: Collision cross sections σ for different molecules, buffer gases and temperatures, obtained from fits of simulated to experimental data

reality is captured by the fitted effective total collision cross section. Here, two different processes are investigated: Inside the cell, the diffusion process is of interest, while boosting is produced by a directed transfer of energy and momentum to the molecules. Therefore, it is not surprising that the simple model with 4π homogeneous scattering cannot capture both effects. However, one free fit parameter for each of the effects is enough to tailor the simulation for the specific process. A more detailed investigation of the collisions, taking into account scattering angle distributions and inelastic collisions, might be able to remove this discrepancy, but is beyond the scope of this thesis.

It is important to note that this fit of the effective collision cross section for the boosting is only done for one of the resulting velocity distributions. With this parameter the simulation can subsequently reproduce velocity distributions including a correct boosting effect for buffer gas densities ranging over one order of magnitude. The measured data together with the simulation results are shown in Fig. 2.15. A shift of the velocity distribution is clearly observed, e.g. the slowest molecules appear at $50\,\mathrm{m\,s^{-1}}$ and $100\,\mathrm{m\,s^{-1}}$ for Fig. 2.15d) and Fig. 2.15f), respectively. The high velocity tail reaches $150\,\mathrm{m\,s^{-1}}$ and $200\,\mathrm{m\,s^{-1}}$, respectively, much higher than expected for a thermalized, non-boosted molecule beam.

2.5 Buffer gas cell optimization

After having explained the simulation and showed its validity, I will propose a way to optimize the buffer gas cell, saving time compared to a purely empirical trial-and-error approach. The optimization process suggested here follows a certain path, suited for our setup. However, it can easily be adopted for different cell geometries, molecule species, buffer gas species, temperatures, or other figures of merit.

Here, we will find the optimal cell length for our buffer gas cell, while keeping the cell diameter and nozzle area and position constant. We use CH_3F and helium at a cell temperature of 7 K. Under these conditions, we want to achieve a molecule sample that is thermalized to the cell temperature, while still avoiding boosting, at a maximum molecule flux.

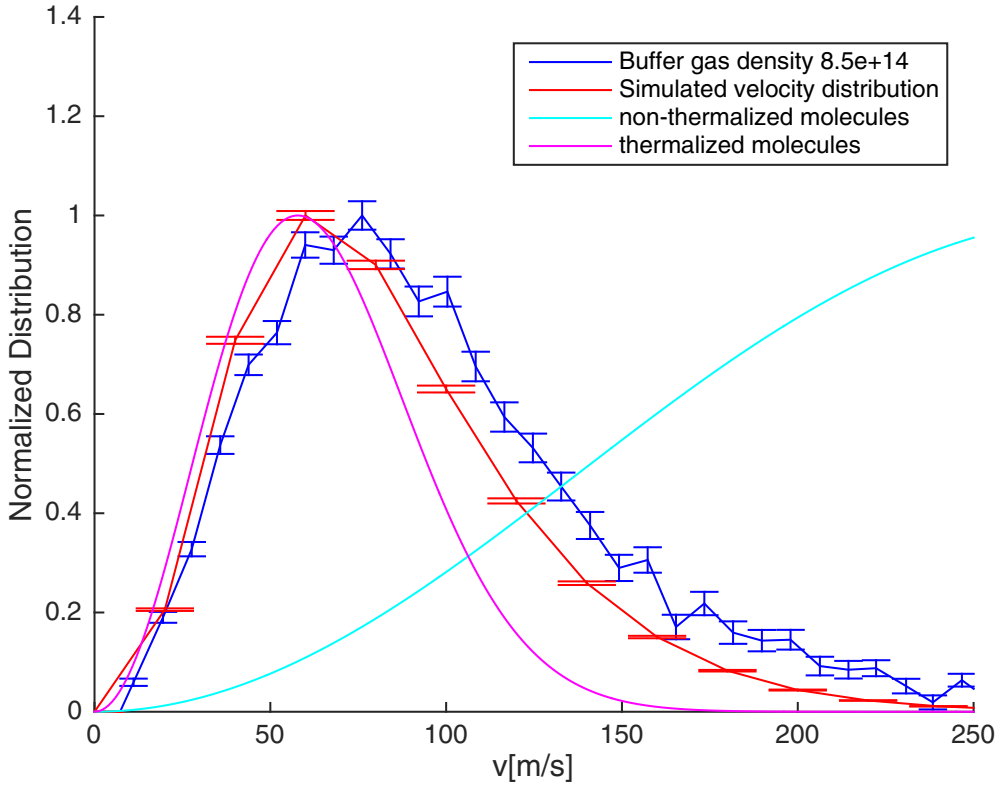

Figure 2.14: Comparison of velocity distributions obtained by simulations in red and from the experiment in blue. Error bars show 1σ statistical error. The cyan line shows the velocity distribution expected for molecules at the cell input without thermalization to the cell. The pink curve shows the velocity distribution of molecules fully thermalized to the cell temperature. The molecules are clearly not yet fully thermalized, which is accurately tracked by the simulation.

Fig. 2.16 shows the count rate of molecules coming out of the cell versus the average number of collisions a molecule experiences before it exits the cell, depending on the cell length. The shape of the curves is the same as in Fig. 2.11. For close to zero collisions, the count rate is inversely proportional to the cell length, as the cell only acts as aperture, and a longer cell reduces its acceptance angle. For bigger number of collisions, diffusion in the cell sets in, and the scaling is not trivial any more. However, over the full range, a shorter cell always produces a higher count rate of molecules for the same number of collisions. We found from previous experiments and simulations that about 20 collisions are necessary to fully thermalize the molecules with the cell. It appears that a cell with a length of 0.5 cm or even shorter would be best for a high number of thermalized molecules in a beam.

However, there is another constraint: to suppress boosting. In Fig. 2.17, the average number of collisions is depicted depending on the buffer gas density for the different

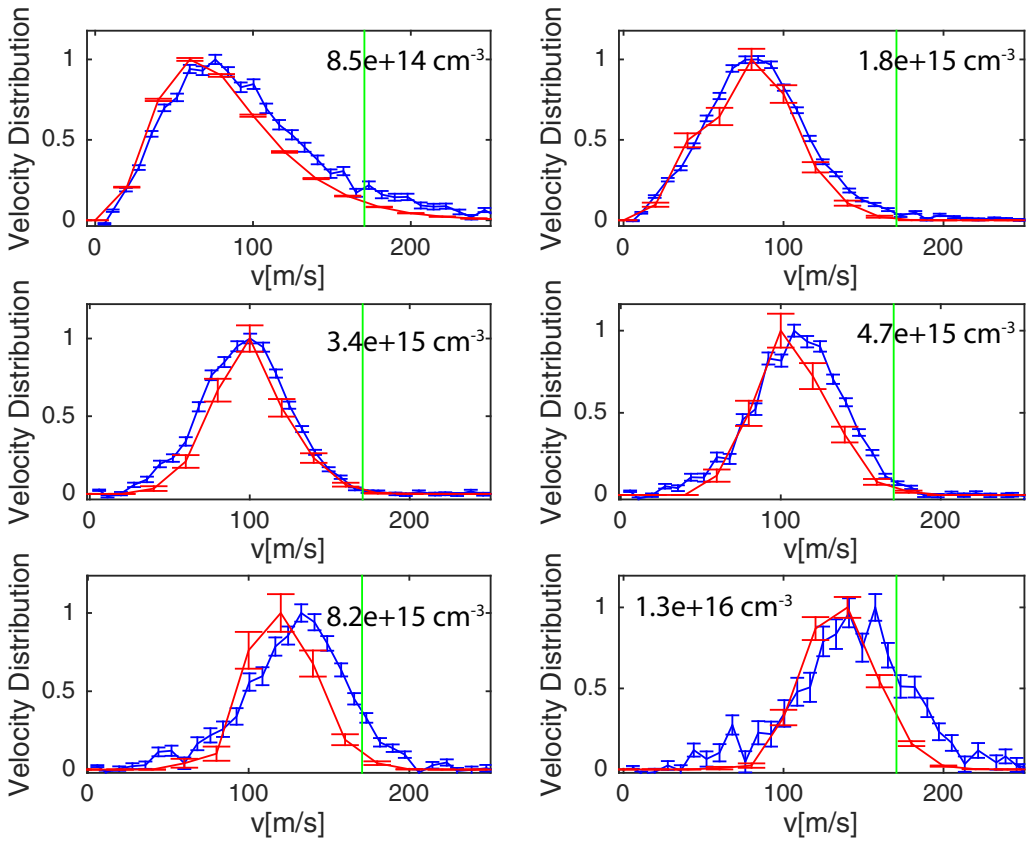

Figure 2.15: Comparison of velocity distributions obtained by simulations and experiment, in red and blue, respectively. a)-f) shows the results for an increasing buffer gas density. a) is the same data as shown in Fig. 2.14. The green line shows the most probable velocity of buffer gas atoms in a Maxwell-Boltzmann distribution at cell temperature. The simulation can correctly predict the shape of the velocity distribution over a range of one order of magnitude in buffer gas density.

cell lengths. It is naively clear that for a shorter cell a higher buffer gas density is necessary to obtain the same number of collisions. From previous simulations and experiments, as shown in Fig. 2.15, it is known that boosting sets in for densities higher than about $3 \times 10^{15}\,\mathrm{cm}^{-3}$. Therefore, to still achieve 20 collisions at this density, the cell should not be shorter than 1 cm. This would be the optimum cell length for the given geometry and boundary conditions.

For shorter cells, the buffer gas density has to be increased even further to maintain enough collisions for thermalization. This directly increases the boosting effect if the nozzle diameter is kept constant. As long as the boosting is not a problem, however, shorter cells can be beneficial. This should be the case if the buffer gas cell is combined with a molecule decelerator, as the Cryofuge setup described in chapter 3. Other experimental boundary conditions, like the maximum buffer gas flux into the vacuum chamber limited by the pumping speed installed, or a possibly

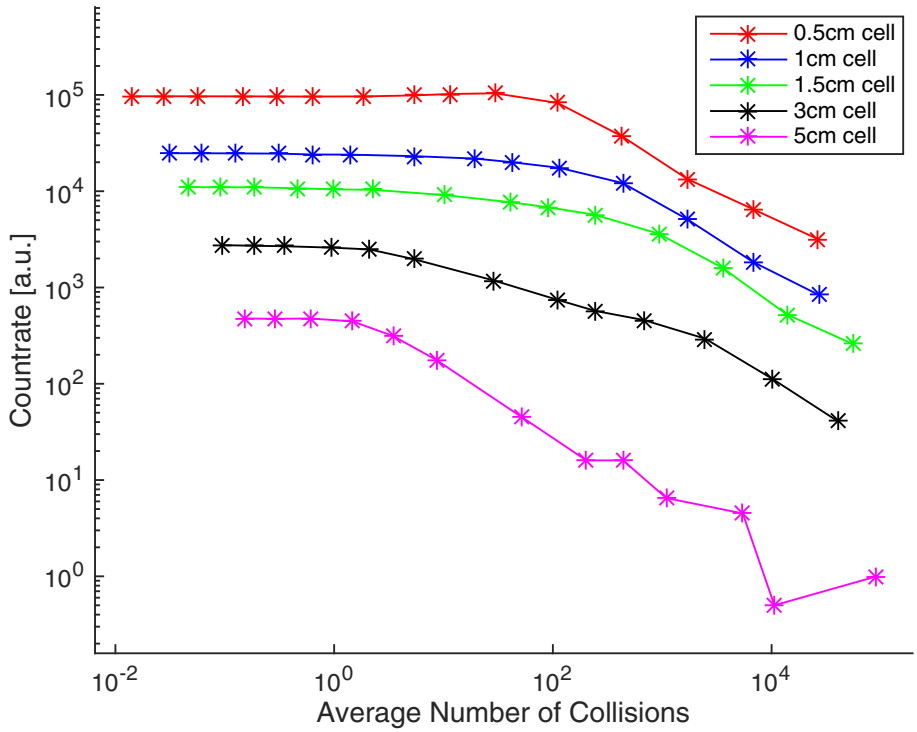

Figure 2.16: Count rate of molecules coming out of the cell versus the average number of collisions per molecule with buffer gas atoms for various buffer gas cell lengths. For less than one collision on average, the count rate is inversely proportional to the cell length. For any given number of collisions, a shorter cell results in a higher molecule count rate.

accelerated freezing of the buffer gas cell are not considered in the simulation, and difficult to predict without empirical testing. For the rest of this thesis, the idea of a shorter cell is not implemented. However, efforts in this direction are currently on the way.

Similar optimizations can be performed for different parameters or cell geometries. Only one setup in the lab is required to fix the total collision cross section for the simulation as described previously. The simulations shown in Fig. 2.16 and Fig. 2.17 took about 10 hours to complete on a standard office PC. Therefore, the tedious and time-consuming setup of different buffer gas cells can be considerably shortened.

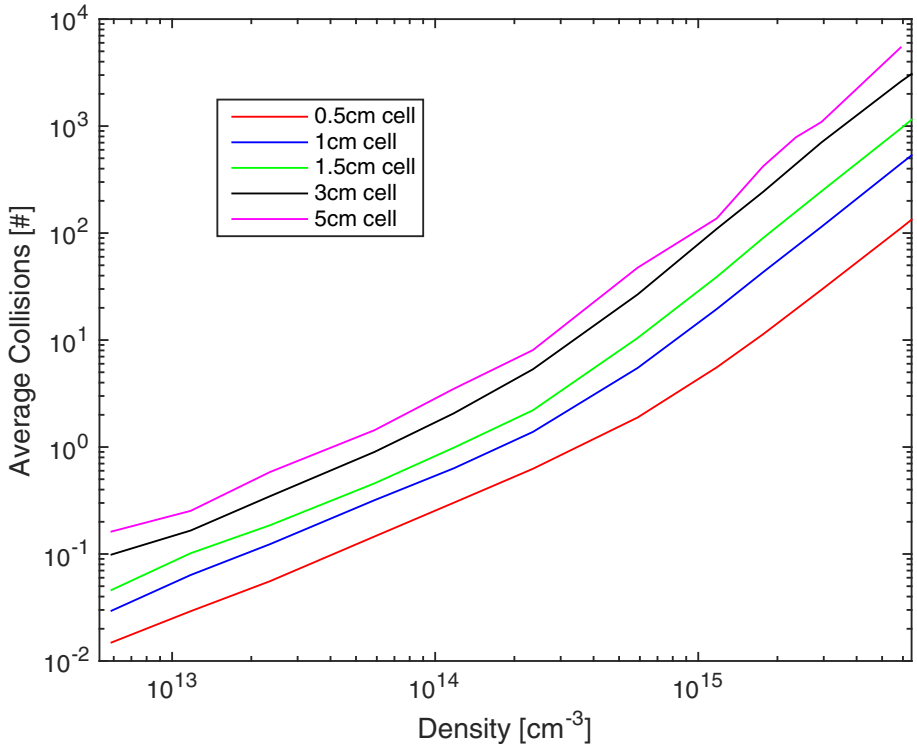

Figure 2.17: Average number of collisions per molecule versus the buffer gas density in the cell for various buffer gas cell lengths. For shorter cells, a higher buffer gas density is necessary to obtain the same number of collisions. For a desired minimum of 20 collisions to achieve thermalization and a maximum density of $3 \times 10^{15}\,\mathrm{cm}^{-3}$ to avoid boosting, the cell should not be shorter than 1 cm.

3 Cryofuge

In this chapter I will describe the experimental setup and the measurements performed on our Cryofuge. Cryofuge is the name given to the combination of a CRYOgenic buffer gas cell and the centriFUGE decelerator, which both have been described previously [CWB+14, Wu17, SvBM+09, vBSM+09]. I will first briefly introduce the main components of the system, the electrostatic quadrupole guides, the buffer gas cell, and the centrifuge. I will also introduce the quadrupole mass spectrometer (QMS), our detection device, together with its issues when used in time resolved measurements. I will then present the results from the setup, including characterization and calibration measurements. This will show the versatility of the device. The Cryofuge is able to decelerate different species of molecules, works on various input velocity distributions and can be easily optimized for different purposes, e.g., trapping of molecules or collision experiments. In the last part of the chapter, the results from our molecule-molecule collision experiments are reported. This includes the description of our measurement scheme, the theoretical background of the measurement, and the comparison of the experimental findings with theoretical predictions.

3.1 Setup

3.1.1 Electrostatic quadrupole guides

The workhorse of the setup is the electrostatic quadrupole guide. It was used before, and is described in detail in various papers and theses. Here, I will only briefly present the basic concepts and equations necessary to understand the following experiments. For a description in greater detail, please refer to [SvBM+09, Mot09, Jun05, vBSM+09].

The molecules we use possess a permanent electric dipole moment $\vec{d}$, which depends on their internal state. In an electric field $\vec{E}$, they experience a potential $V = -\vec{d}\cdot\vec{E}$. The molecular states we guide have their EDM anti-aligned with the electric field, and therefore the potential minimum is at a electric field minimum. These molecules are called low-field seekers. By using high voltages applied to electrodes arranged in quadrupole configuration, we achieve a line-shaped electric field minimum that the molecules follow.

In a straight guide, the molecules are trapped transversely, and can move freely along the axis of the guide. With the Stark shift E_{Stark} at the saddle point between the electrodes given by $E_{Stark,max}$, the maximum transverse velocity at which molecules can still be guided is given by

$$v_{t,max} = \sqrt{2E_{Stark,max}/m_{mol}} \tag{3.1}$$

$E_{Stark,max}$ linearly depends on the voltage applied to the guide electrodes.

However, in a bent guide, the centrifugal force, and consequently also the longitudinal velocity v_l, plays a role. This force is given by $m_{mol}v_l^2/R$, where R is the bend radius. The longitudinal cut-off velocity is then given by $v_{l,max} = \sqrt{E'_{Stark,max} \cdot R/m_{mol}}$ with the maximum slope of the Stark shift $E'_{Stark,max}$. Assuming a perfect quadrupole potential, we can estimate this as

$$v_{l,max} \approx \sqrt{E_{Stark,max}/r \cdot R/m_{mol}} \tag{3.2}$$

with r the inner guide radius. With this simple model, the qualitative behavior of the system can be described. For a rigorous quantitative analysis, a Monte-Carlo simulation can be employed.

3.1.2 Layout of the Experiment

The layout of the experiment was planned on the basis of previously existing setups, and is a combination of two well-established molecule experiments of our group. The buffer gas cell and the centrifuge are described in detail in two theses [Som11] and [Wu17], respectively. Both experiments were designed using the electrostatic quadrupole guide. The two experiments were joined by linking the output of the buffer gas cell setup to the centrifuge, and use it as a source for the centrifuge.

Fig. 3.1 shows the technical drawing of the setup. On the right, the vacuum chamber housing the buffer gas cell is visible. Compared to the system described in [Som11], the vacuum chamber now has a rectangular cross section for easier accessibility, and is dubbed "Cryochamber". The molecules are guided from the cold cell to the edge of the cryochamber by a guide with a 90° bend at a radius of 20 cm.

The guide section between the bend guide in the cryochamber and the centrifuge is referred to as "Connection Guide". The voltages on this guide can be controlled independently from the Cryochamber guide and the centrifuge. Thereby the transversal trap depth can be adjusted, and it will be used to adjust the molecule density in the guide for collision measurements.

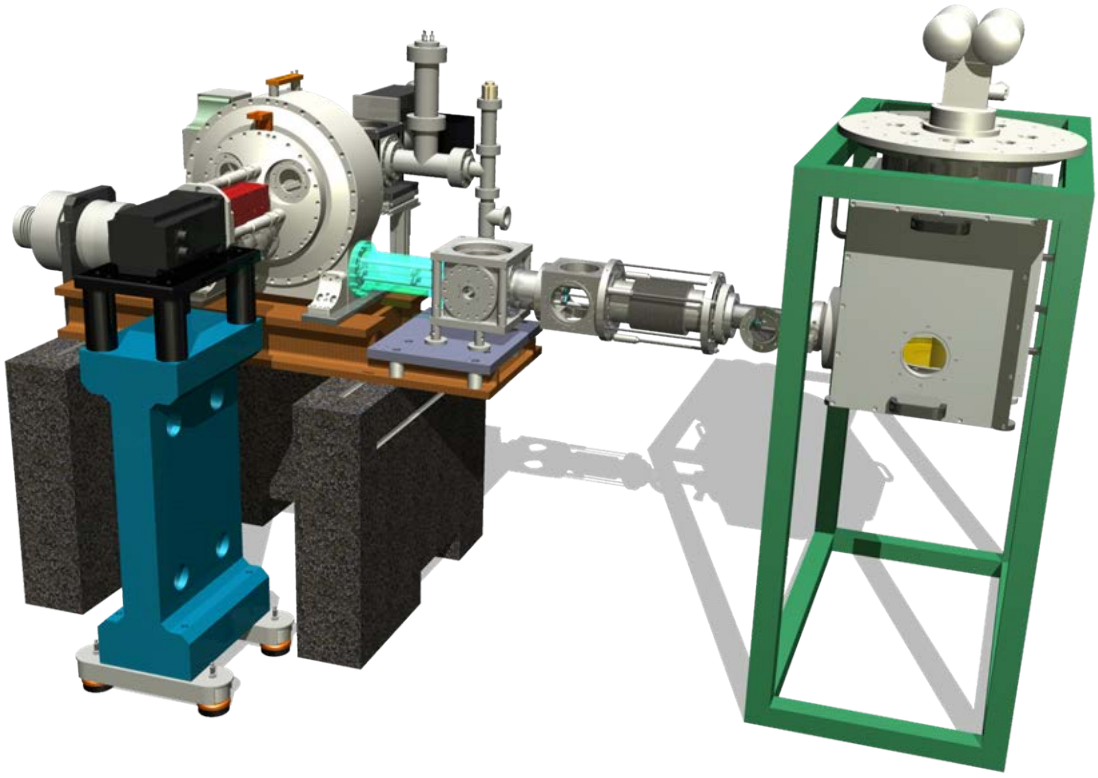

Figure 3.1: Technical drawing of the cryofuge setup. The cylindrical vacuum chamber containing the centrifuge is visible on the left, the rectangular chamber containing the buffer gas cell on the right. The vacuum tube connecting the two chambers contains the electric guide .

The centrifuge itself is unchanged compared to [Wu17], a short description is given in sec. 3.1.4. At the exit, a straight guide with a length of 46 cm is attached to act as a TOF range, allowing us to measure the velocity distribution of the molecules. As in previous experiments, a QMS (Pfeiffer QMG 700) is used to detect the molecules a few millimeters after the exit of the TOF guide.

Fig. 3.2 shows a photograph of the vacuum setup, with the cold source on the left and the centrifuge on the right side.

Several turbo pumps help to maintain the vacuum in the system. Additionally, the cold, charcoal-coated surface around the buffer gas cell provides additional pumping. The pressure is highest in the cryochamber, at just below 1×10^{-6} mbar during operation, due to the flux of buffer gas and unguided molecules into the vacuum. The rest of the system is separated by a differential pumping section, which allows to maintain the pressure in the centrifuge at below 1×10^{-8} mbar. At the QMS detection region, an additional ion pump and a titanium sublimation pump help to maintain a pressure around 5×10^{-10} mbar. The low pressure is particularly

important here to reduce the background count rate.

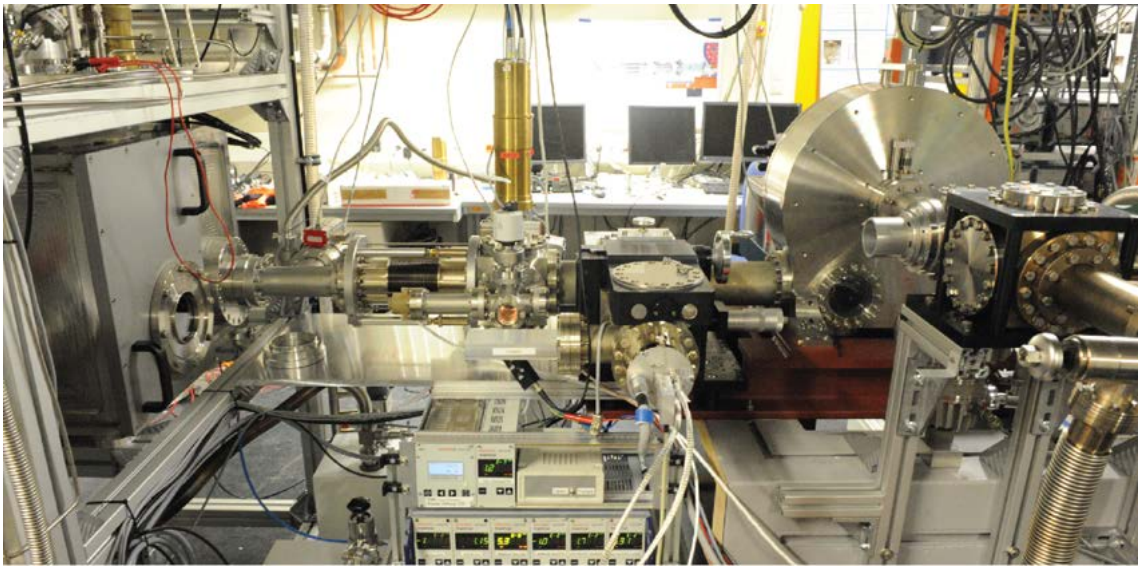

Figure 3.2: Photo of the cryofuge setup. The vacuum chamber housing the buffer gas cell is visible on the right. The circular vacuum chamber on the right holds the centrifuge setup. The QMS is not visible.

A sketch of the buffer gas cell was already presented in chapter 2, and is shown in Fig. 2.3. This setup has been used with slight variations for previous experiments using buffer gas cooled molecules. The cell consists of a copper cylinder with a diameter of 3.5 cm and a length between 1 cm and 2 cm, depending on the cell being used in the effusive or supersonic regime. The length of the cell can be easily changed by adding or removing parts from it. It is optimized to achieve a large molecule flux in a suitable velocity range. The molecules are transported into the cell through a Teflon tube which is thermally isolated from the cell and stabilized to a temperature just above the freezing point of the molecules. The buffer gas feed line is precooled to the cell temperature, allowing a low cell temperature to be maintained, as well as to thermalize the buffer gas atoms before they enter the cell. The buffer gas is delivered by eight symmetrically arranged holes in the cylinder wall vertical to the molecule input, to obtain a homogeneous buffer gas distribution inside the cell. The output nozzle is placed in the center of the plane opposite the molecule input hole, with a diameter of 2 mm.

3.1.3 QMS Space Charge Effect

The QMS used for all experiments described in this thesis uses a cross beam electron impact ionizer to produce the molecular ions. The electron beam is produced by a hot cathode, and vertical to our incoming molecule beam, as well as to the mass filter of the QMS. Several parameters have to be carefully adjusted to achieve a high

detection efficiency. In this section I will discuss the setting of two parameters in detail, the electron emission current controlling the electron flux in the ionization volume, and the cathode voltage, controlling the kinetic energy of the electrons. A high electron emission current leads to a high electron density in the detection region, and therefore to a higher detection efficiency. Unfortunately, a high electron density can also lead to a delayed detection of the molecular ions generated by the electron beam. This effect has been seen before [BH93, BMV74], and was attributed to a space charge effect that can temporarily trap the ions in the detection region. Therefore, the measured velocity distribution would appear to contain more slow molecules. This is detrimental to the good timing precision necessary to measure the velocity of the molecules with the TOF technique.

To avoid these artifacts, the electron emission current was reduced far enough to prevent the space charge trapping of ions. Fig. 3.3 a) shows the velocity distribution of the molecules after the centrifuge taken with two different emission currents, 0.06 mA and 0.12 mA in blue and red, respectively. All other settings were unchanged. The velocity distributions appear identical, as expected. Unfortunately, these emission currents are drastically reduced compared to the 0.6 mA, which is recommended for general application by the manufacturer. Thereby, the detection efficiency of the QMS is reduced, and measurement times increase.

A similar space charge effect could occur for high enough ion densities in the detection region. The envisioned collision experiment depends on measuring molecule velocity distributions for various molecule densities. Therefore, we have to assure that the detection efficiency of the QMS does not depend on the molecule/ion density in the detection region for the relevant settings. To check this effect, we shift the QMS detector away from the end of the guide, increasing the distance from 24 mm to 36 mm. All other settings were unchanged. This reduces the molecule density at the QMS position as it covers a smaller solid angle of the emerging molecule beam. Fig. 3.3 b) shows the point-by-point ratio of the two velocity distribution. The constant ratio for all velocities measured confirms the linear response of the detector.

After completion of the collision measurements, we found a different way to suppress the unfavorable space charge effect. The electron density n_e inside the ion source of the QMS is given by

$$n_e = I_{\text{emi}}/(A \cdot v_e) \tag{3.3}$$

with the emission current I_{emi}, the cross-sectional area of the electron beam A and the velocity of the electrons v_e. Instead of decreasing the emission current to reduce the electron density, the velocity of the electrons can be increased. This can be set by the cathode voltage V_{emi} of the QMS, because $v_e \propto \sqrt{V_{\text{emi}}}$. To test this, the guides to the QMS are switched on at time $t = 1\,\text{s}$, and the evolution of the signal

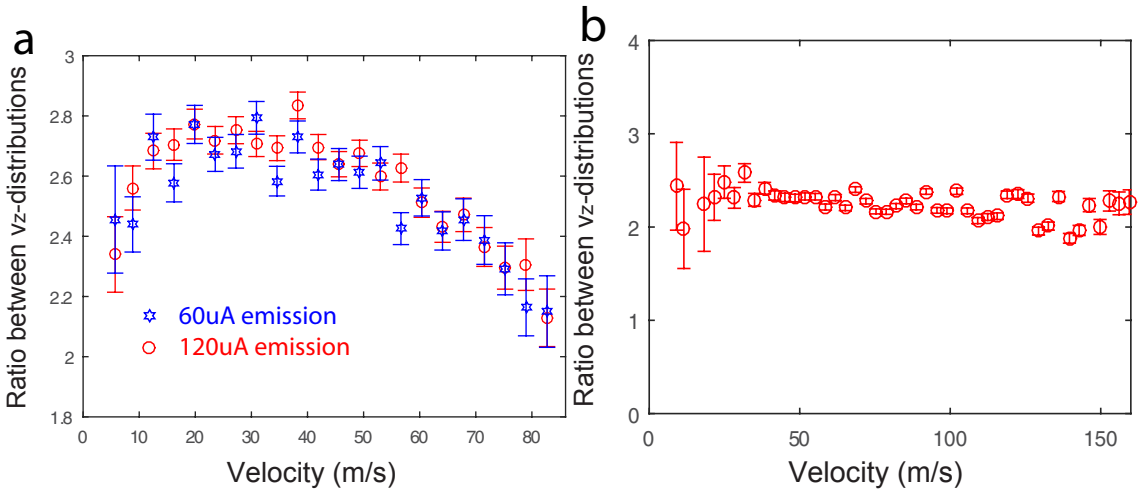

Figure 3.3: a) Velocity distributions taken for different QMS electron emission currents. The blue curves show the data taken at 0.06 mA, red the data for 0.12 mA. Error bars shows 1σ statistical errors. b) Point-by-point ratio of velocity distributions taken with the QMS at different distances from the guide, 24 mm and 36 mm, changing the molecule density in the detection region. The constant ratio shows the independence of measured velocity distributions from the molecule density, for otherwise identical experimental parameters.

is recorded. This is repeated for different emission currents, 0.12 mA, 0.56 mA and 0.8 mA, and two different cathode voltages, 20 V and 40 V. The resulting curves normalized to their final value are shown in Fig. 3.4. The full signal is shown in the inset. The fast rising signal is the TOF signal, and could be used to obtain a velocity distribution. Here, the focus lies on the settling of the signal, which can be delayed by the space charge effect, and the zoom of this detail is shown in the main part of the figure. Error bars are omitted for clarity.

The blue, purple and red curves show the data for smaller cathode voltage of 20 V, for an emission current of 0.12 mA, 0.56 mA and 0.8 mA, respectively. For the low emission current, the signal settles immediately, as expected. For the higher emission current of 0.8 mA, however, the signal level takes more than 5 s to settle, starting from about 90% of its final value. At the intermediate value of 0.56 mA the effect is already strongly suppressed, but still visible. The settling time is reduced to about 3 s, and the signal level before settling reaches 98% of its final value.

The result for the higher cathode voltage of 40 V and an emission current of 0.8 mA is shown in yellow. The combination of cathode voltage and emission current is chosen so that the electron density in the detection area is the same as for the measurement with a cathode voltage of 20 V and an emission current of 0.56 mA according to equation 3.3. As seen in Fig. 3.4, these two measurements shown in purple and yellow give the same results, as expected. Therefore, an increased cathode voltage can be used to suppress the space charge effect instead of a reduced emission current,

leading to a better detection efficiency.

Unfortunately, this was not know when the data shown in the rest of this chapter was taken. However, it will be used for further molecule collision measurements in the trap, where the preparations are shown in chapter 4.

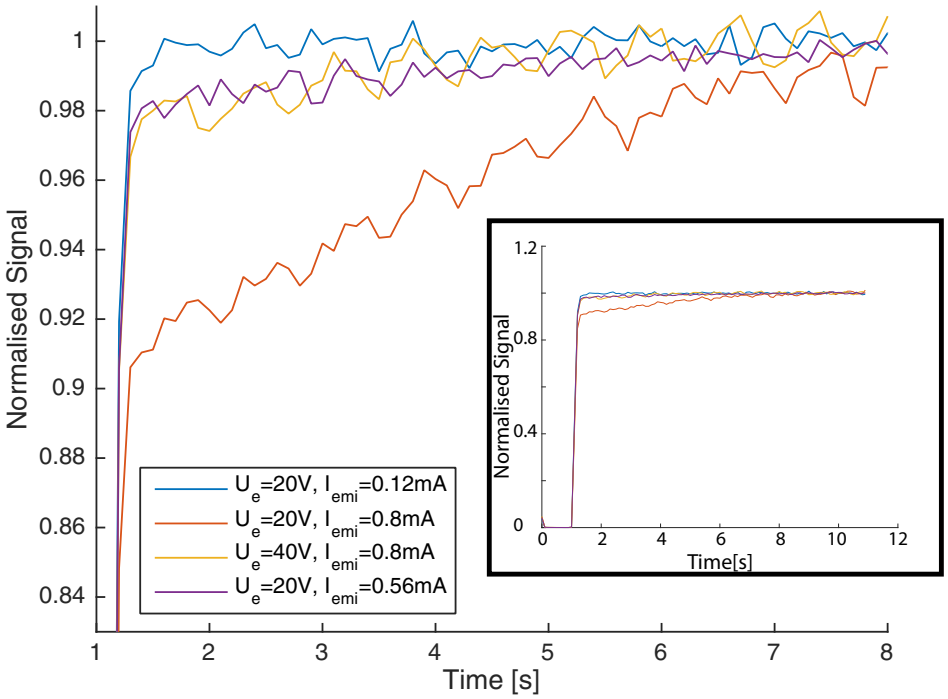

Figure 3.4: Signal settling for different electron emission currents and different cathode voltages. The guides are switched on at time $t = 1\,\mathrm{s}$, and the full curves are displayed in the inset. The main figure shows a zoom in to the data to show the signal settling after the fast increase due to time-of-flight of the molecules. The data for smaller cathode voltage of 20 V and for an emission current of 0.12 mA, 0.56 mA and 0.8 mA are shown in blue, purple, and red, respectively. A settling with an amplitude of about 10% is clearly visible for the highest emission current. The data for larger cathode voltage of 40 V and for an emission current of 0.8 mA is shown in yellow. Here, the settling effect is identical to the purple curve, as expected for identical electron density according to 3.3. Error bars are omitted for clarity.

The delayed detection of molecules due to a space charge effect in the QMS are currently still investigated. Apart from the dependence on the cathode voltage and the emission current, evidence for a dependence on molecule ion density was found. However, the effects are not yet fully understood.

3.1.4 Centrifuge

The Centrifuge was already comprehensively described previously. Here, I will briefly describe the important features. For more details please refer to [Wu17, CWB+14].

The basic principle of the centrifuge is to provide a potential hill, where molecules convert their kinetic into potential energy. The potential is given as $E_{\text{Centrifugal}} = -\frac{m}{2}\left(\vec{\Omega} \times \vec{r}\right)^2$, with m the mass of the decelerated particle, Ω the rotation speed of the centrifuge, and the distance from the rotation axis $\vec{r}$.

A sketch of the setup is shown in Fig. 3.5. The electrostatic guide is bent in a spiral shape, here shown in red and blue, which is optimized to decelerate molecules smoothly. The spiral is rotating to provide the centrifugal potential. The molecules are brought into the rotating spiral by a static quadrupole guide with a sharpened endpoint, dubbed "Injector", shown in green and yellow. The static electrode in yellow around the periphery of the spiral together with the rotating long tail of the spiral in red ensures guiding of molecules until they reach the spiral, and enables a quasi-continuous operation. In the center of the spiral, the molecules are guided out of the rotating plane by the exit bend, so that they leave the centrifuge along its rotation axis. While the radius of the centrifuge R is fixed at 20 cm, and m is given by the molecule we want to decelerate, we can set the height of the centrifugal potential by choosing Ω. This adjustability is crucial to be able to use the centrifuge for different molecules, different buffer gas cell settings, and to produce different output velocity distributions.

Fig. 3.6 shows an illustration of the shifting velocity distribution of the molecules depending on the centrifuge speed Ω. The bottom curve shows the input velocity distribution, which is unchanged, as the centrifuge is at standstill. Nevertheless, the fastest molecules (in red, part A) are lost before they can reach the spiral part of the centrifuge: they are too fast to be guided around the bend formed by the periphery of the centrifuge with a radius of 20 cm, following equation 3.2. These molecules will be lost for any rotation frequency. The blue part (labeled B) of the curve is lost due to the same velocity filtering effect at the exit bend. This bent sets a tighter limit to the molecule velocity, as it has a smaller radius of 5 cm. The portion of molecules lost here can be reduced or even eliminated by operating the centrifuge at higher Ω, as seen in the other curves. The green part (labeled C) of the molecules can exit the centrifuge. In this setting, the centrifuge acts as a simple velocity filter for molecules. As typical for molecules from a buffer gas cell, very slow molecules are missing due to the boosting effect.

The middle curve shows the centrifuge operation close to the optimum. After the prefilter cut-off, the molecule velocity is shifted towards smaller velocities, the portion of molecules in B is reduced, and the number of molecules in C is enhanced, producing molecules down to $0\,\mathrm{m\,s^{-1}}$. The molecules in the orange part of the distribution (labeled D) cannot escape the centrifuge due to their insufficient initial

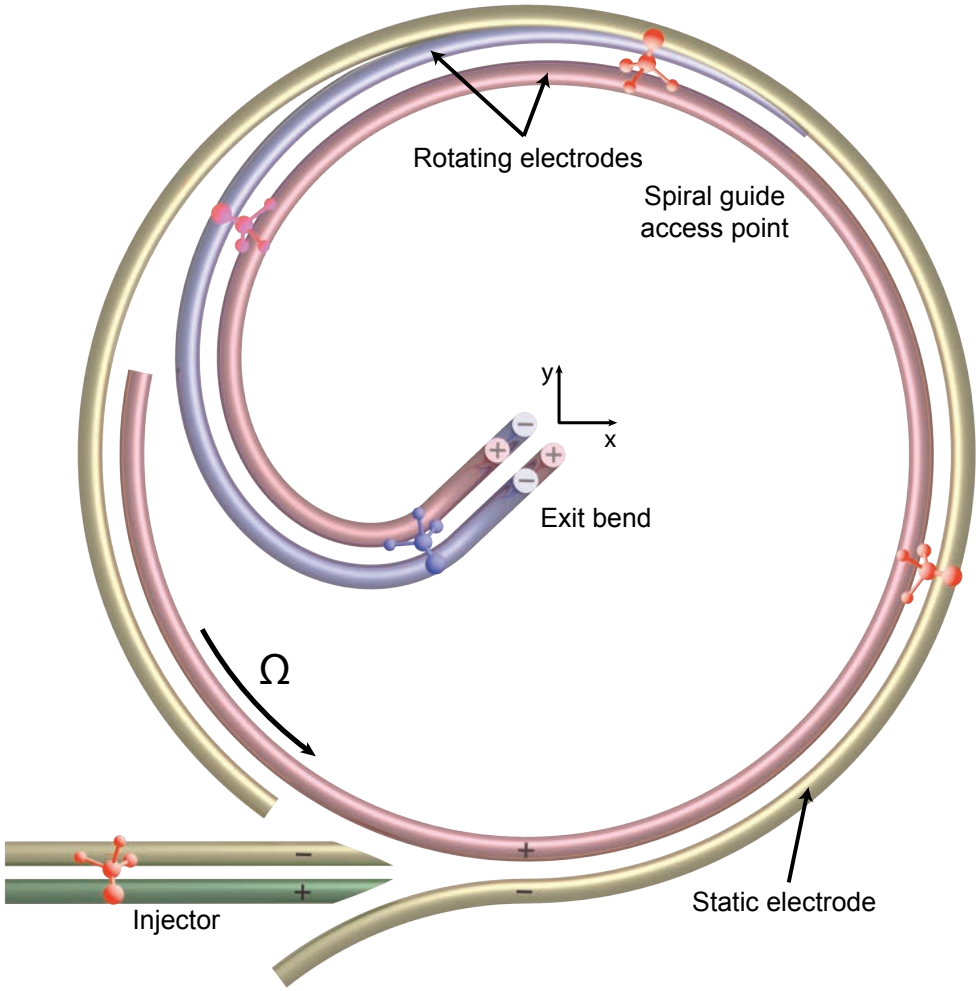

Figure 3.5: Schematic drawing of the centrifuge. Static parts are in green and yellow, rotating parts in blue and red. Sizes are not to scale

kinetic energy. These molecules cannot reach the center of the centrifuge with the highest centrifugal potential, propagate back towards the buffer gas cell, and are eventually lost.

The upper distribution shows the output velocity distribution of the molecules for an even higher rotation speed. The blue part of the curve is completely eliminated, but also the number of molecules exiting the centrifuge in the green part is greatly reduced, and most molecules are sent back towards the source. However, the number of very slow molecules close to $0\,\mathrm{m\,s^{-1}}$ is still increased compared to the middle curve. This shows that the centrifuge has to be optimized, depending on the required output velocities of the molecules, e.g., maximum total flux or maximum flux of slowest molecules.

Note that the velocity distribution broadens as it is shifted towards slower and

slower velocities. This comes from the fact that a purely conservative potential is employed. Therefore only deceleration, but no cooling, can take place, and the phase space density has to be conserved. We find a efficiency of the centrifuge of about $10\% - 20\%$ for optimized settings, depending on the input velocity distribution.

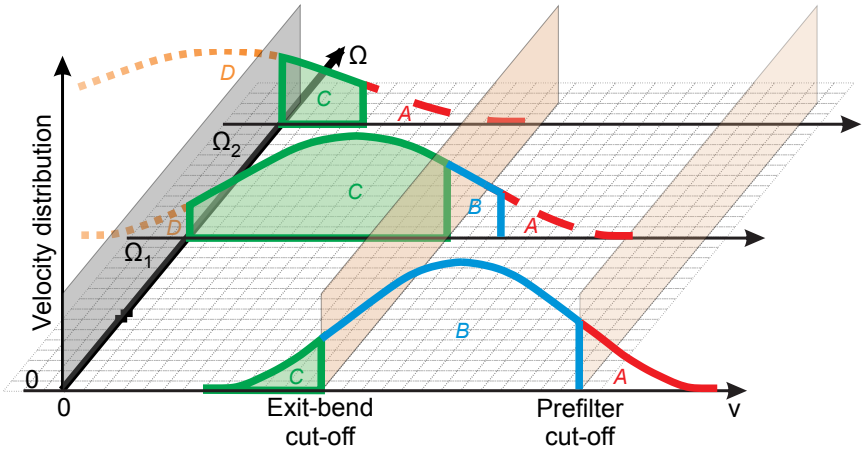

Figure 3.6: Velocity distributions for varying centrifuge speeds Ω. The part of the distribution shown in red is lost due to the prefilter cut-off, the part in blue is lost due to the exit-bend cut-off, the orange section is lost due to insufficient initial energy of the molecules. The green part can exit the centrifuge and is usable for further experiments.

3.2 Characterization

With the main principles of the Cryofuge briefly summarized, the characterization of the setup will be presented in this section. To quantify the molecule flux and density, the calibration of the QMS will be explained. The dependence of the outcoming molecule beam on the buffer gas cell settings, the centrifuge speed and the guiding voltages will be explored. To demonstrate the versatility of the Cryofuge setup, deceleration for several different molecule species will be presented.

3.2.1 QMS Calibration

To be able to quantitatively understand the results of the Cryofuge, we first need to calibrate our QMS. This calibration will be used to convert the count rate of

registered ions cr at the detector to the flux of molecules f in the beam. The conversion factor depends on a number of parameters and experimental settings. The molecule species affects the sensitivity of the QMS, the molecule velocity defines the time a molecule spends in the detection region, and the distance between the QMS and the end of the guide together with the escape angle of the molecules determine the percentage of molecules that reach the detection volume. To understand our measurements, all these factors need to be taken into account. In the following, one example for such a calibration will be shown; for the subsequent parts of the thesis, whenever absolute molecule numbers or densities are given, it will be on the basis of such a calibration.

The first part of the calibration is to connect the QMS count rate to the density of particles in the detection region. Because this strongly depends on the QMS settings, it has to be remeasured whenever these are changed, or when parts of the QMS or its electronics are replaced. It is, however, valid for any QMS position relative to the molecule beam, and for all beam velocities. To measure this sensitivity of the QMS, we introduce molecules into the QMS vacuum chamber, and record the ion count rate. At the same time, we record the pressure in the vacuum chamber on a separate hot cathode gauge. Fig. 3.7 shows a typical linear relationship between the pressure and count rate. The blue squares display the measured values, the red line a linear fit to the data. The offset of the curve results from the non-zero pressure in the vacuum chamber before the start of the calibration, which arises from molecules and atoms of different mass, not detected by the QMS. This offset does not have an impact on the following calculations. The slope of the fitted curve directly links the QMS count rate to the molecular density in its detection region. Employing the ideal gas law and the manufacturer-given molecule sensitivity of the gauge, we link the count rate to a molecular density n in the detection volume of the QMS by a proportionality constant c_{mol}, $n = c_{mol} \cdot cr$.

The next step is to evaluate the beam spread of the molecules between the guide exit and the QMS. A small gap between the electrostatic guide and the QMS is necessary to avoid electrical discharges, therefore, inevitable, some of the molecule will miss the QMS, and are not detected. The probability of a molecule to hit the QMS depends on its longitudinal and transversal velocities. As the transversal velocity distribution of the molecule beam is set by the guiding potential, the biggest influence is the average longitudinal velocity of the molecular beam. Therefore, we repeat this measurement whenever the velocity distribution changes considerably.

To be able to measure the size of the molecule beam, the QMS is mounted on a 3D translation stage. We set the experiment to produce the molecular beam properties of interest, and then shift the QMS in two dimensions perpendicular to the molecular beam. The result of such a scan in one dimension is shown in Fig. 3.8. The blue points show the scan for a centrifuge decelerated beam, the red points show a post-selection by the TOF technique on molecules slower than $20\,\mathrm{m\,s^{-1}}$. The blue and red solid curves are Gaussian fits to the data as guide to the eye. As expected, the slower beam spreads more than the fast beam, for an identical translational velocity

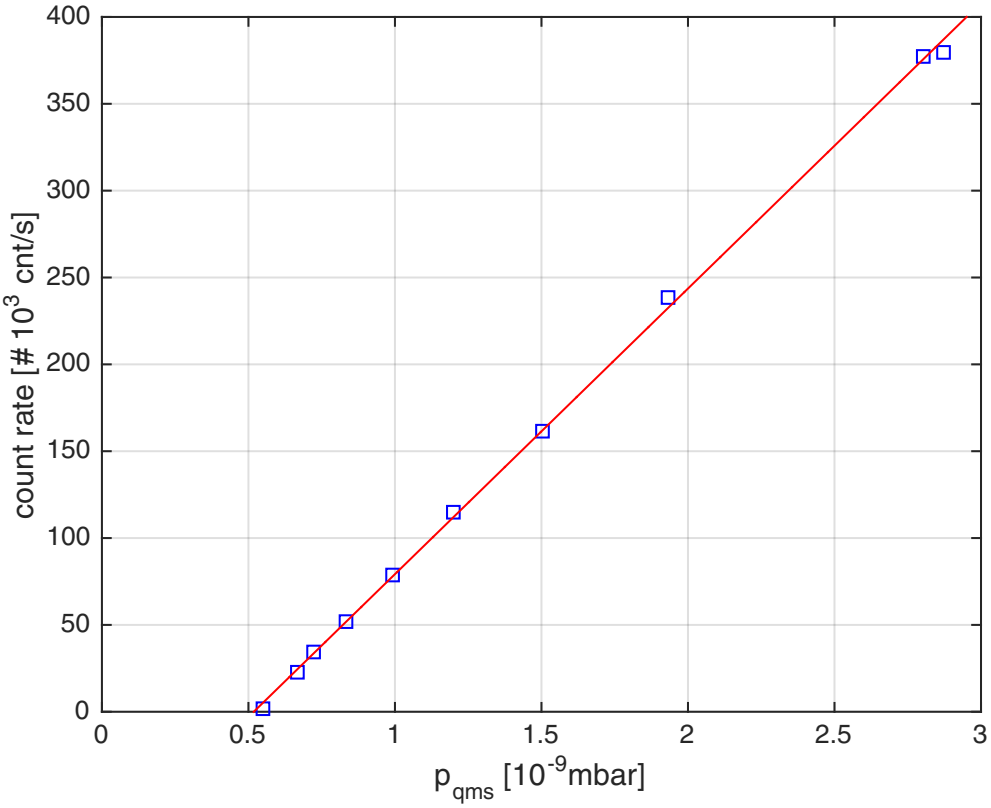

Figure 3.7: Density calibration of the QMS. The recorded count rate of the QMS is plotted as blue squares against the density in the vacuum chamber. The red line is a linear fit to the data. The slope of the curve is used as calibration factor c_{mol}. The offset of the curve results from the non-zero background pressure, and does not have an impact on the calibration.

distribution. From this measurement we can infer what portion of the molecules miss the QMS, giving a geometric correction factor c_{geo}. From the TOF measurement we know the average velocity of the molecules v_{ave}. With this information, we can calculate the flux of molecules as

$$f = cr \cdot c_{mol} \cdot c_{geo} \cdot v_{ave}$$

3.2.2 Optimization of buffer gas density and centrifuge rotation frequency

After we established a way to quantify the molecule flux out of the centrifuge, we now examine the dependence of the resulting molecule beam on the buffer gas density in the cryogenic cell, and the centrifuge rotation speed. As mentioned before (see

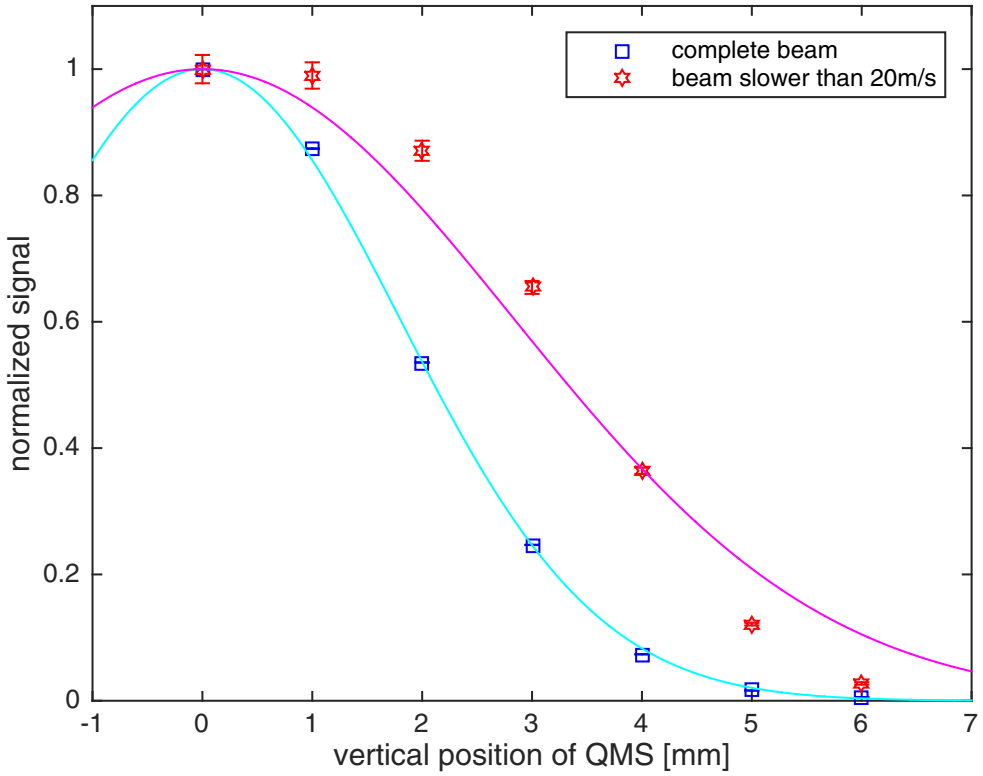

Figure 3.8: Normalized QMS signal level for different QMS positions, in one dimension. Blue points show the data for the full molecule beam, red points the result for molecules slower than $20\,\mathrm{m\,s^{-1}}$. The blue and red lines are Gaussian fits to the data.

Fig. 3.6), the rotation speed has to be optimized for each input velocity distribution independently. As the velocity distribution of molecules out of the cell changes drastically with the buffer gas density, this optimization process is done multiple times. As we are not only interested in a high absolute flux of molecules, but specifically in slow molecules, we measure velocity distribution for all settings. Thus, we can always readjust the centrifuge settings to achieve maximum flux for certain velocity classes of molecules. A particular interest is in molecules with a kinetic energy of less than 1 K, as this is roughly the trap depth we are able to achieve with the electrostatic trap [EMS+11, ZEG+12].

When we perform the centrifuge frequency scan for several different buffer gas densities, we obtain Fig. 3.9. In *a*), we plot the total flux of molecules against the centrifuge rotation speed for different buffer gas densities, while in *b*) we only count molecules below $20\,\mathrm{m\,s^{-1}}$. In red, the flux for the case of no buffer gas is shown. Here, the buffer gas cell does not cool the molecules, and the average molecule input velocity is too high to be effectively decelerated. Nevertheless, an increased flux is

visible for high rotation speeds.

For the lowest buffer gas density investigated here, the molecule flux is shown in pink. With this setting, we achieved the highest total flux as well as the highest slow flux. This would suggest that the lowest possible density of buffer gas would produce the most slow molecules. However, other effects begin to dominate at lower densities. For even lower buffer gas densities, the internal states of the molecules are not thermalized to the cryogenic buffer gas cell, even though the translational degrees of freedom might be. This was investigated before, and presented in detail in [WGZ+16]. Moreover, for lower densities, the buffer gas does not effectively keep the molecules away from the cell walls. This leads to a faster formation of molecule ice at the cell nozzle, and ultimately a drastically reduced measurement cycle.

For higher buffer gas densities, the boosting effect of molecules out of the buffer gas cell is evident from the fact that higher and higher rotation speeds are necessary to obtain the maximum molecule flux. When comparing Fig. 3.9*a* and Fig. 3.9*b*, it is apparent that higher rotation frequencies are required to achieve ideal conditions to create slower molecules, as expected.

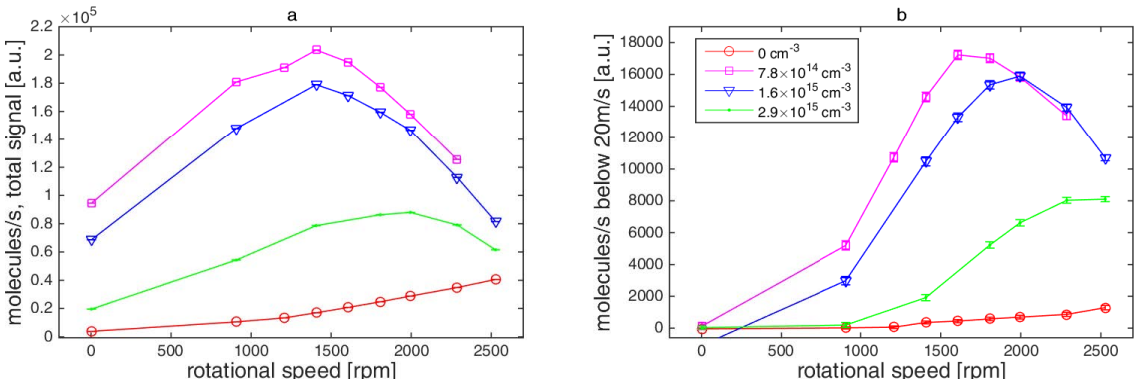

Figure 3.9: Molecule signal after the centrifuge, versus rotation speed, for different buffer gas densities in the cryogenic cell. Figure a) shows the total signal, figure b) only molecules slower than 20 m s^{-1}. The peaks for the slow signal appear at higher rotation frequencies. Higher buffer gas densities result in stronger boosting, and require higher rotation frequencies to achieve ideal deceleration. Without buffer gas (red circles), the molecules are hardly cooled and too fast to be completely decelerated.

Fig. 3.10 shows a 2D map of velocity distributions of CH_3F for various centrifuge rotation speeds from standstill to 45 Hz. The buffer gas cell is operated in the effusive regime, with the Helium flux into the cell fixed at a value of 0.5 sccm, corresponding to a buffer gas density of 1.6×10^{-15} cm^{-3} in the cell. At this flux, the internal states of the molecules can thermalize to the cell temperature, as was shown previously ([WGZ+16]). The figure shows the molecule line density per velocity class, comparable to Fig. 3.6. The white dashed line at 86 m s^{-1} marks the peak velocity of the input molecular beam. The black dashed line corresponds to 1 K kinetic energy

for CH_3F at $22\,\mathrm{m\,s^{-1}}$. Several interesting features are visible in this figure. The cut-off velocity for the centrifuge exit bend guide is at about $100\,\mathrm{m\,s^{-1}}$ for CH_3F, which explains the lack of signal for faster molecules, even for $\Omega = 0\,\mathrm{Hz}$. For a non-rotating centrifuge, there are no molecules slower than $22\,\mathrm{m\,s^{-1}}$ in the beam. Additionally, the total flux of molecules after the centrifuge is rather small. When gradually increasing the rotation frequency, the peak of the velocity distribution is shifting to smaller and smaller velocities. The absolute flux of molecules increases up to an optimum at about 28 Hz, and then decreases. When trying to get a high flux of molecules $< 22\,\mathrm{m\,s^{-1}}$, however, the signal still increases when increasing the centrifuge speed up to 32 Hz. The curve measured at 45 Hz resembles the highest rotation frequency curve in Fig. 3.6: The tail of the velocity distribution is below the cut-off velocity, but the overall flux is already strongly decreased. When we compare the output flux at optimum settings to the input flux, we find an efficiency of the centrifuge of about 20%.

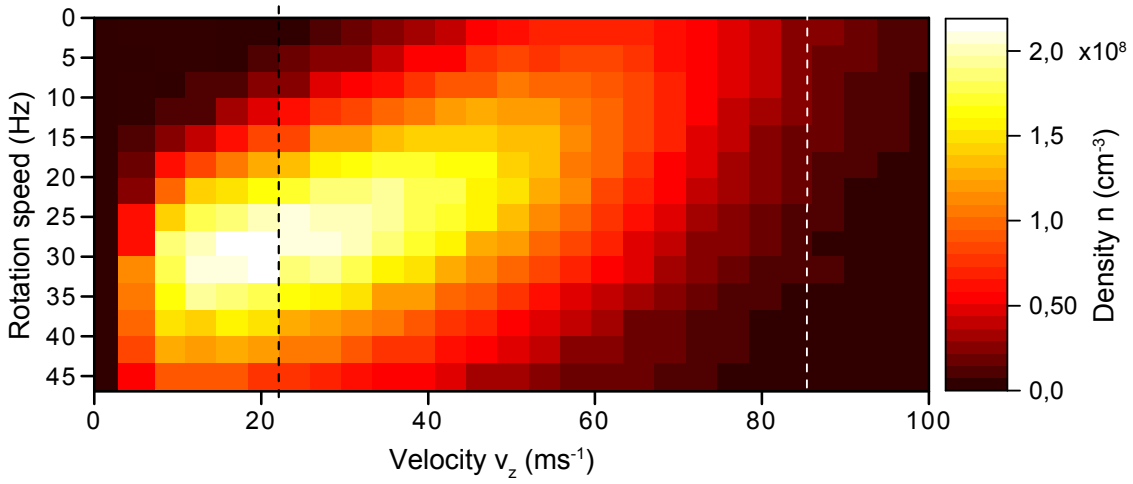

Figure 3.10: Velocity distributions for various centrifuge rotation speeds, as color plot. Each line of the plot is a velocity distribution taken for a certain rotation frequency. The position of the peak of the input distribution is shown as white dashed line. The black dashed line corresponds to 1 K kinetic energy. For higher rotation speeds, the peak of the velocity distribution shifts to lower velocities. The output flux first increases for higher speeds, then decreases. The maximum flux is found at 28 Hz.

By using a supersonic buffer gas beam, the internal temperature of the molecules can be reduced even further. At the settings used here, the internal temperature was measured to be below 3 K, see ([WGZ+16]). However, the molecules from a supersonic expansion will be faster than from an effusive source. This ultimately limits the efficiency of the centrifuge. Fig. 3.11 a) shows the comparison between the input and output velocity distributions of the centrifuge with the buffer gas cell operated in the supersonic regime. The error bars represent a 1σ statistical error. Neon is used as a buffer gas at a flux of 7 sccm, while the cell temperature is stabi-

lized to 17 K. The input data in red is scaled by a factor of 0.2, and fitted with a Gaussian curve. The fit indicates a peak velocity of 165 m s^{-1} and a velocity spread corresponding to an energy of (3.3 ± 0.1) K in the co-moving frame. The blue output curve is overlaid with the expected output obtained by a Monte Carlo simulation. The blue shaded area shows the molecules with an energy corresponding to less than 1 K. Here, the centrifuge was operated at a considerably higher rotation frequency of 62 Hz. With the supersonic beam, the centrifuge achieves an efficiency of approximately 8%. The reduced efficiency comes from the increased input velocities, which results in poorer guiding ability of the bend guide. A centrifuge optimized for supersonic input beams should therefore employ a larger radius. The decline of signal towards zero velocities is due to the gap between the centrifuge output and the TOF guide: The transversal velocity of the molecules is not reduced in the centrifuge, and leads to a larger divergence angle for very slow molecules. This is confirmed with Monte Carlo trajectory simulations.

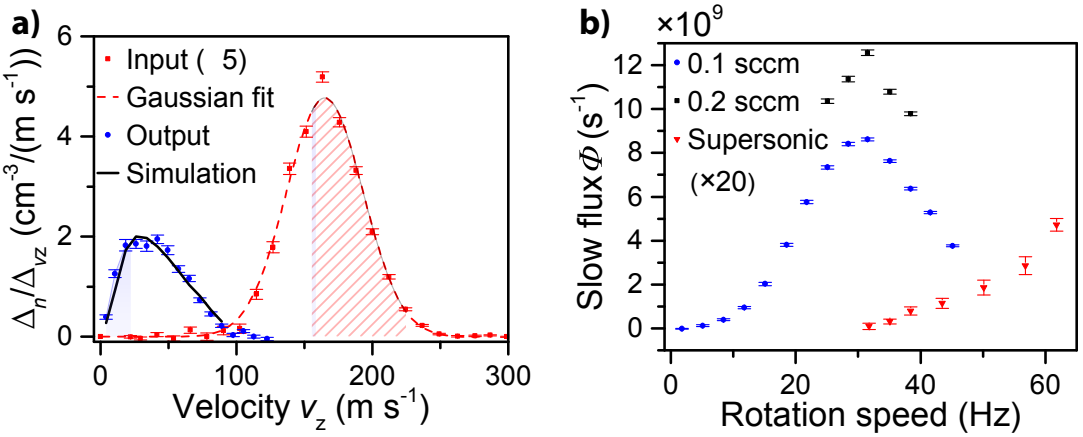

Figure 3.11: a) Velocity distribution at the input and output of the centrifuge in red and blue squares, respectively. The buffer gas cell was operated in the supersonic regime. The input curve is scaled by a factor of 0.2 for clarity. The red dashed line is a Gaussian fit to the input distribution. The black curve is a Monte Carlo simulation, taking the input distribution and centrifuge deceleration into account. The red shaded area shows the molecules that end up with a longitudinal velocity > 0 m s^{-1}. b) Flux of slow molecules versus centrifuge rotation speed, for different buffer gas cell settings. The black and blue curves are measured with a Helium flux of 0.5 sccm, a cell temperature of 6.5 K and a molecule flux of 0.2 sccm and 0.1 sccm, respectively. The red curve is measured for the cell in supersonic regime, with 7 sccm Neon flux, 17 K buffer-gas cell temperature, and 0.1 sccm molecule inflow. The red curve is scaled up by a factor of 20 for visibility.

The main purpose of using the centrifuge decelerator is the production of slow molecules that can be trapped in an electrostatic trap. Fig. 3.11 b) shows the flux of these slow molecules versus the centrifuge speed, for different buffer gas cell settings. Error bars represent a 1σ statistical error. The blue diamonds depict the

flux for the boosted cell, with a Helium flux of 0.5 sccm, a cell temperature of 6.5 K, and a molecule flux into the cell of 0.1 sccm. The peak at about 30 Hz is clearly visible. When even higher molecule densities or fluxes are desirable, the molecule flux into the cell can be increased to 0.2 sccm, the data is shown in black. This hardly changes the velocity distribution, and the position and shape of the peak, but increases the count rate. The drawback, however, is the reduced operational time before the buffer gas cell has to be heated up, as molecule ice forms faster at the cell nozzle. Therefore, the data in Fig. 3.10 was taken at 0.1 sccm molecule flux. The red curves shows the flux of slow molecules for the supersonic cell, 17 K buffer-gas cell temperature, 7 sccm Neon inflow, 0.1 sccm molecule inflow, scaled up by a factor of 20. The flux obtained for the supersonic setting is clearly smaller than for the boosted regime. Nevertheless, if minimal internal temperature of the molecules is crucial, the supersonic beam can be advantageous. For the rest of this thesis, were high molecule densities are essential, the effusive regime is used.

3.2.3 Demonstration of versatility: deceleration of various molecule species

We have shown that the centrifuge can decelerate a beam of molecules cooled in a cryogenic buffer gas cell. The data shown up to here were all obtained for only one molecule species, Fluoromethane (CH_3F). However, cryogenic buffer gas cells have proven to be extremely versatile, as they do not depend on molecular properties like their internal energy structure. Therefore, they have been used for a great variety of different molecule species. The range reaches from small, light and chemically stable molecules like deuterated ammonia (ND_3) ([vBSM$^+$09]), through heavy radicals as Strontium fluoride (SrF) or Thorium oxide (ThO) ([BSD11, VCG$^+$10]), to big biological molecules like trans-cinnamaldehyde ([ZBMS15]), just to name a few.

The guiding technique and the centrifuge deceleration rely only on the interaction of the molecule with a static electric field. Therefore, it is limited to uncharged particles with a reasonably large dipole moment to mass ratio. This a weak precondition, and many different molecules fall into this category. We prove the versatility of the Cryofuge by decelerating a number of diverse molecule species. Symmetric tops are typically best suited, but it is not a necessary requirement, as the deceleration of methanol (CH_3OH) and isopropanol (C_3H_8O) shows.

A typical example for molecules that are suited for buffer gas cooling and deceleration in the Cryofuge is the previously mentioned CH_3F. The dipole moment of 1.9 D and mass of 34 u makes it well-suited for guiding, and consequently for centrifugal deceleration. Therefore, we often use it as first example in our measurements. Additional molecules chosen and their relevant properties are displayed in Tab. 3.1.

For ND_3 and trifluoromethylacetylene (CF_3CCH), both symmetric tops just as CH_3F, a similar flux of molecules of about $1 \times 10^{10}\,s^{-1}$ with a kinetic energy corresponding to below $1K$ was achieved. Out of the molecules mentioned in this thesis,

CF_3CCH is likely to be best suited for subsequent Sisyphus cooling ([ZEG+12]), as shown in [ZMPR09], while ND_3 is expected to have beneficial collision properties. Therefore, considerable effort was used to achieve a high flux for these molecules. The other molecules were used to show the deceleration of non-symmetric tops, and, in the case of methanol, to show the deceleration of molecules which are important in astrophysics ([SBGH13]), or could be used to measure variations in the proton-to-electron mass ratio [BDJ+13]. As there are no immediate plans for further use of these molecules in our experiment, the optimal experimental parameters were not thoroughly investigated here. The main limitation was the low vapor pressure even at room temperature. We expect that such issues could be resolved by addition of an supplementary heater at the molecule inlet tube.

Species	Dipole moment [D]	Mass [u]	Slow flux [s^{-1}]
CH_3F	1.9	34	1.2×10^{10}
ND_3	1.5	20	1.0×10^{10}
CF_3CCH	2.4	94	1.0×10^{10}
CH_3OH	1.7	32	3×10^{8}
C_3H_8O	1.7	60	1×10^{8}

Table 3.1: Properties and maximum achieved flux of slow molecules for various species. The dipole moment is given in Debye D, the mass in atomic mass units u, and the flux of molecules below $20\,\mathrm{m\,s^{-1}}$ in molecules/s.

3.3 Collisions in the guide

With the high density of slow molecules in the electrostatic quadrupole guide, we are now able to observe molecule-molecule collisions at a low energy. In this section, I will first present the theoretical foundation for the measurement, and an estimation on the effect we expect to see. Afterwards, the experimental scheme will be explained. In the end, the collision results will be shown and compared to the calculations.

3.3.1 Theoretical background

There are many different approaches to observe particle collisions. For this experiment, we aim to observe losses, which are a side effect of molecule-molecule collisions in our system. The basic consideration is that the probability for a molecule to be lost from the guide due to collisions p_{loss} is higher for slower molecules, as the time τ spent in the guide before reaching the detector depends inversely on their velocity,

$\tau \propto \frac{1}{v_{||}}$. As the collision rate is constant over time in a continuous beam as produced by the Cryofuge, the loss rate increases for slower molecules, $p_{\text{loss}} \propto \frac{1}{v_{||}}$.

Different mechanisms can contribute to losses due to collisions. Elastic collisions can redistribute kinetic energy between the longitudinal and transversal directions. As the average total kinetic energy of the molecules is bigger than the transversal trap depth, this redistribution can lead to a loss of molecules. This can be pictured as billiard ball like collisions, were fast molecules "kick out" the slower ones. An artists view of this process is depicted on the title page of this thesis.

The second mechanism is inelastic, state-changing collisions that can contribute in two different ways. If the internal state of the molecules is redistributed randomly in an inelastic collision, it can go from its initially low field seeking to a high field seeking state. For these molecules, the guide no longer acts as a guide, but expels them. Furthermore, if molecules are transferred to energetically lower lying states during the collision process, the excess energy is transferred to translational energy, so that the molecules can overcome the guiding potential.

As all these mechanism show up as signal loss from the guide, and we have not used a method to distinguish these two mechanisms, we are not able to distinguish elastic from inelastic collisions. The explanations and calculations given here follow the descriptions in the supplement of [WGK+17].

If a molecule is lost via an elastic collision depends on many different parameters. The transversal position in the guide defines the potential the molecules experience during the collision, and consequently the transversal trap depth, as does the transverse velocity of the collision partners. Their relative longitudinal velocity together with the scattering angle determines how much of the longitudinal energy is transferred to transversal energy.

As the large number of relevant parameters make exact calculations unfeasible, Monte Carlo simulations are used. To do so, we first have to investigate the initial distributions of the molecules in the guide. For the transversal kinetic energy and spatial distribution, a linear electric field strength distribution and linear Stark shift are assumed, ignoring the non-linear field distribution at the edges of the guide as well as quadratic contributions to the Stark shift. With this a assumption, phase-space volume arguments give an transversal energy distribution $\propto v_{\perp}^5$, where $v_{\perp}$ is the transverse velocity of the molecule. The position distribution of a molecule can be written as $R(\rho) \propto \rho(\rho_0 - \rho)$,with the radial position of the molecule ρ and the inner radius of the guide ρ_0. The probability for a collision to occur at a position ρ is then $\propto R(\rho)^2/\rho = \rho(\rho_0 - \rho)^2$. The ρ in the denominator is to account for the azimuthal coordinate of the molecules.

From this starting distribution, two collision partners and a collision position are randomly chosen. For a given relative longitudinal velocity $v_{z,rel}$ and a given scattering angle θ, the resulting velocities of the collision partners is computed, assuming a purely elastic process. If the transverse energy of a molecule after the collision ex-

ceeds the guiding potential depth, the molecule is considered lost. It is important to note that both molecules have the probability to get lost during one collision event. In order to avoid double counting, our model only includes the loss probability of one of the two. With this, we obtain the loss probability for a molecule, for a given $v_{z,\mathrm{rel}}$ and θ. The result is shown in Fig. 3.12a). As expected, the loss probability increases for higher relative velocities as well as for bigger scattering angles, as both result in a higher transfer of energy. The longitudinal velocity distribution is known from TOF measurements, and when taking this into account, the loss probability dependent on the scattering angle $P_{\mathrm{loss}}(\theta)$ can be plotted, see Fig. 3.12b).

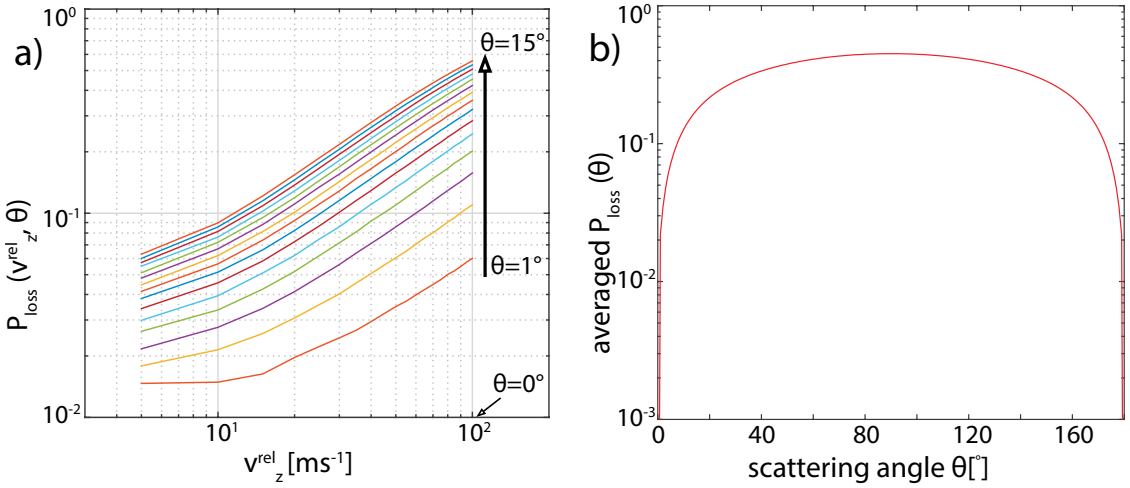

Figure 3.12: a) Loss probability of a molecule in an elastic molecule-molecule collision versus relative longitudinal velocity $v_{z,\mathrm{rel}}$ for various scattering angles θ. b) Loss probability versus θ, for the v_z-distribution measured in the experiment.

To derive the distribution of the scattering angle θ, the eikonal approximation is used. This semi-classical approach strongly favors forward scattering processes, resulting in a small energy transfer. The differential cross section can be calculated depending on the relative velocity. The result is shown in Fig. 3.13a). The decrease of the cross section for increasing $v_{z,\mathrm{rel}}$, and also the dramatic decrease for even moderate scattering angles θ is obvious. As before, the known v_z distribution enables us to calculate the averaged differential cross section for our molecules shown in Fig. 3.13b). Note the logarithmic scale on the vertical axis. From this it becomes clear that most collisions are at small scattering angles, and will not lead to losses. From all these numbers we can finally work out the theoretical loss rate of the molecules $k_{\mathrm{th,el}}$.

In contrast to elastic collisional losses, the losses due to inelastic collisions do not depend on molecule velocities or scattering angles, making the calculations considerably simpler. We estimate the inelastic collision rate by the Langevin capture model, as summarized in [BS09]. If the internal states of a molecule are randomly distributed after an inelastic collision, the molecule has $\sim 50\%$ probability to end

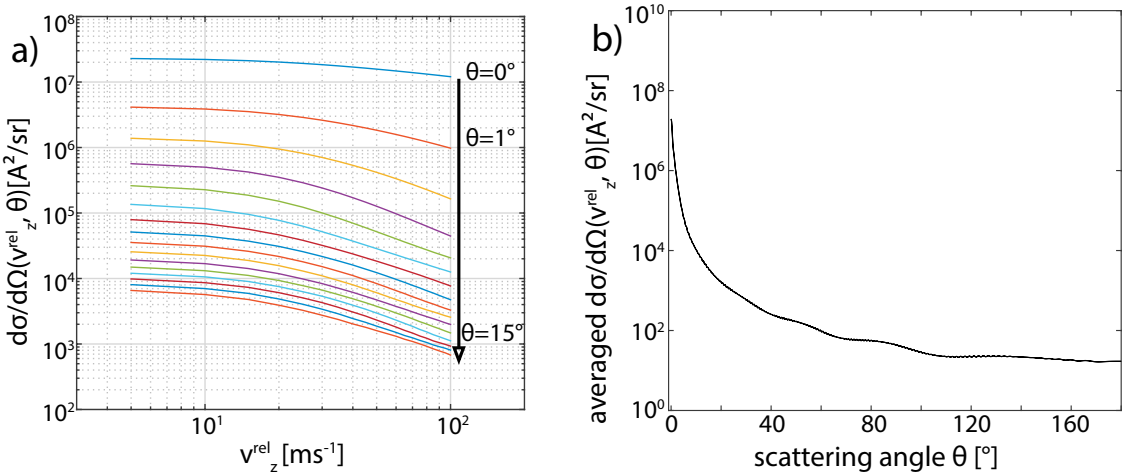

Figure 3.13: a) Differential cross section of the molecule-molecule collision as function of v_z, calculated based on the eikonal approximation. b) Collision cross section versus scattering angle, for the v_z-distribution given in the experiment.

up in a high-field seeking, non-guided state. Therefore we assume one of the two collision partners is always lost during each inelastic collision event.

3.3.2 Effective length of the guide

In sec. 3.3.1 we showed how to find the loss rate of molecules with a given longitudinal velocity in the guide. To compare to the relative loss signal we get from the experiment, we also need to know the distance the molecules travel in the guide. In the straight TOF guide after the centrifuge the molecule travel with a constant velocity in a fixed molecule density. The length of the guide is simply given by the physical length, L_{TOF}. However, molecules can already experience lossy collisions inside the centrifuge. If we ignore this and set this effective length in the centrifuge L_{eff} to zero, it overestimates the collision rate in the TOF guide. To find a realistic value for L_{eff}, we have to include the changing molecule density in the centrifuge n' and the changing loss rate k'_{th}, resulting from the changing velocity distribution. The effective length of the centrifuge is $L_{\mathrm{eff}} = \frac{n'}{n}\frac{k'_{\mathrm{th}}}{k_{\mathrm{th}}}\tau\, v_z$, and $L_{\mathrm{TOF}} + L_{\mathrm{eff}}$ will be used as effective total distance traveled by molecules, assuming the constant density n and constant loss rate k_{th}.

The transient time τ is numerically calculated from the known spiral shape of the molecule trajectory and the input velocity. Using the conservation of energy in the rotating frame, the velocity distribution at any point in the centrifuge can be calculated analytically, and the result is shown in Fig. 3.14a).

The molecule density inside the centrifuge is altered by two different effects: The conservation of flux, and the losses of molecules at the centrifuge exit. As the flux is constant, the deceleration leads to an increase in molecule density. At the

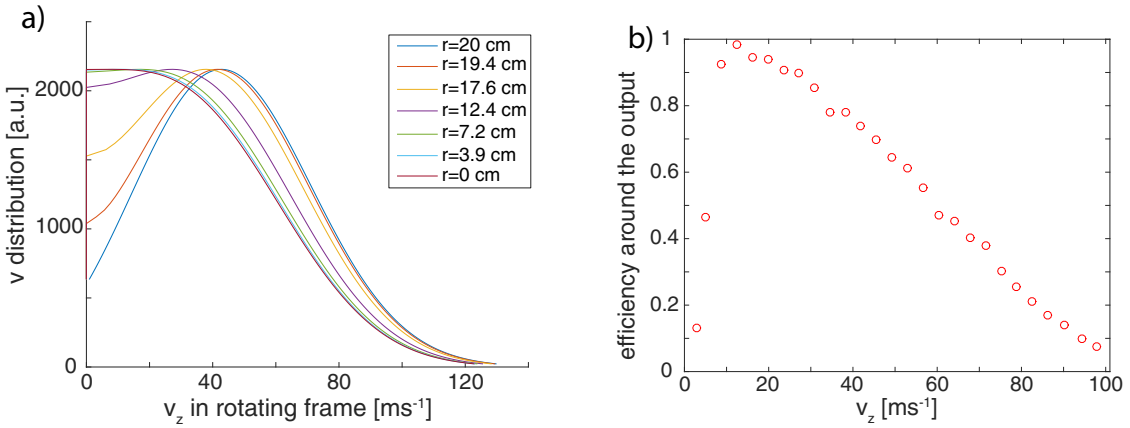

Figure 3.14: a) Velocity distributions of the molecules inside the centrifuge at different distances r from the rotation axis. Curves obtained by numerical calculations. The decelerating effect for decreasing r is clearly visible. b) Calculated guiding efficiency of the centrifuge output. Filtering at the small bend radius reduces the efficiency for fast molecules, while the open gap between the rotating and the static guide opens a loss channel for slow molecules.

exit of the centrifuge, the exit bend with a radius of 0.5 cm is the smallest bend radius in the setup, and therefore contributes the smallest cut-off velocity in the system. Additionally, at the transition from the rotating to the static guide, the slowest molecules are prone to be lost at the 1.2 mm gap. These two effects can be predicted by trajectory simulations and the resulting efficiency of the centrifuge output depending on the molecule velocity is depicted in Fig. 3.14 b). With this, the molecule density in the centrifuge n' can be deducted.

The loss rate k'_{th} can be calculated from the average relative velocity in the beam inside the centrifuge, which is extracted from the varying velocity distributions shown in Fig. 3.14a). The final result for T_{eff} and L_{eff} are plotted in Fig. 3.15a) and Fig. 3.15b), respectively. For molecules leaving the centrifuge at $10\,\mathrm{m\,s^{-1}}$, which make up most of the collision signal, L_{eff} is about 27 cm, smaller than the length of the TOF guide, $L_{\mathrm{TOF}} = 46\,\mathrm{cm}$.

For the estimation of L_{eff}, the calculation neglects the molecule loss along the spiral guide inside the centrifuge. This loss could be due to filtering as the bend radius of the spiral becomes smaller and smaller, or from mixing of longitudinal and transversal velocity in the rotating frame. Both effects should be small, as the centrifuge was designed to guide all molecules that survive the prefilter bend. This leads to a small underestimation of n', and thereby of L_{eff}. In the end, this leads to an underestimation of the expected loss rate.

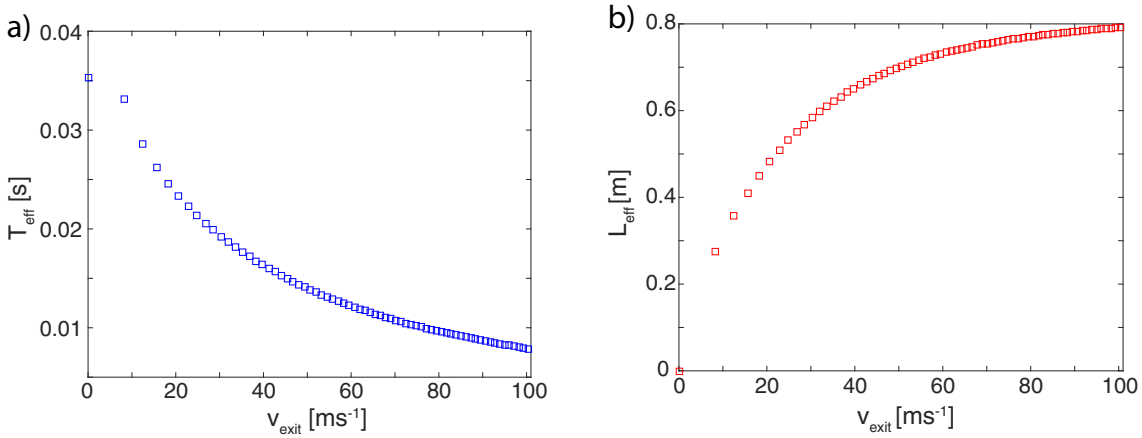

Figure 3.15: a) Effective collision time T_{eff} of molecules inside the centrifuge, weighted by the varied density n' and collisional loss rate k'_{th}. b) The corresponding effective guide length of the centrifuge L_{eff}.

3.3.3 Setting the molecule density

As mentioned, we expect to observe molecule-molecule collisions via velocity dependent losses. We require a technique to measure velocity distributions of molecules coming out of the centrifuge. To see the loss of slow molecules due to collisions, we need a reference velocity distribution without any, or very few collisional losses. This can be found by determining the velocity distribution at lower molecule density. The most straightforward way to vary the density in the guide is to adjust the flux of molecules into the buffer gas cell. This directly changes the flux and density of molecules, as seen in Fig. 3.11b). However, changing the molecule flux slightly changes the buffer gas cell temperature as well as the boosting effect on the molecules, which in turn alters the velocity distribution. The effect is small, but difficult to predict accurately. Consequently, we choose a different method to change the molecule density.

To reduce the molecule density in the guide, we employ our electrostatic guiding technique. Reducing the guiding potential in the straight guide in front of the centrifuge removes transversely fast molecules as shown in equation 3.1, thereby reducing the density. This does not effect the longitudinal velocity distribution. In combination with a bent guide however, velocity distribution variations are possible, but these changes are much easier to predict. Specifically, it is possible to numerically simulate this effect accurately with the help of Monte Carlo simulations. Here, I will present a qualitative explanation of the modified velocity distribution, and the quantitative result of the simulations.

Fig. 3.16 a) shows the potential energy versus the transverse position in the straight guide for different guide voltages typically used in the experiment, 10 kV and 1 kV, in black and gray, respectively. The inner guide radius is given as ρ_0. These two curves are independent of v_z. In the bend guide with a radius R, $R \gg \rho_0$, however, the

effective potential is deformed by the centrifugal force, as depicted in red. This kind of bend is used to guide the molecules out of the buffer gas beam into the connection guide. The deformation of the potential reduces the effective transversal trap depth by the centrifugal energy $E_{\text{cen}} = -mv_z^2\rho_0/R$, which depends on the longitudinal velocity. This velocity dependent reduction of the 2D trap depth is also depicted in Fig. 3.16 b) in red. Here, the velocity independent trap depths of the straight guide at different voltages is shown in black and gray. If a molecule beam is now pre-filtered in the bend guide by the red curve, a reduction of voltages in the straight guide, going from the black to the gray curve, leads to v_z-dependent loss of molecule signal.

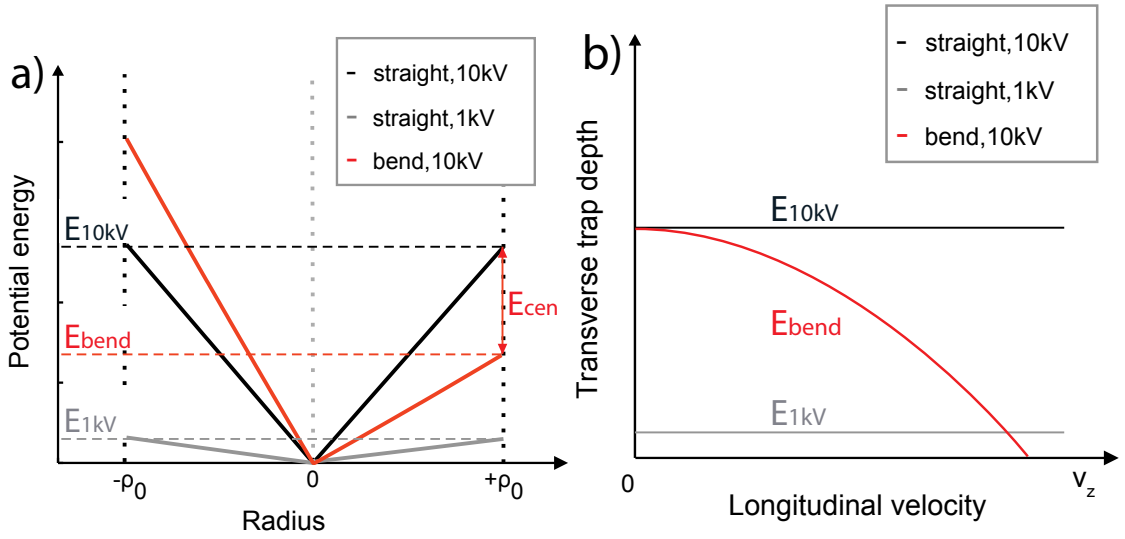

Figure 3.16: a) Potential curve versus radial position in the guide. The black line shows the potential in a straight guide for high guiding voltages of 10 kV, gray line for a straight guide at low voltages of 1 kV, red in a bend guide with a high voltage of 10 kV. b) Transverse trap depth versus v_z. In the straight guide the trap depth does not depend on v_z, shown in black and gray for 10 kV and 1 kV guiding voltage, respectively. The red curves shows the $1/v^2$ dependence for a bend guide due to the centrifugal force.

This effect is quantified by Monte Carlo simulations, as they were used and described in [WGZ+16]. Fig. 3.17 shows simulated point-by-point ratios of v_z-distributions with guiding voltages 10 kV and 1 kV on the straight quadrupole guide, respectively, for CH_3F. Fig. 3.17 a) shows the ratio for the relevant velocities before the centrifuge, Fig. 3.17 b) shows the same ratio, after the molecules are decelerated by a centrifuge with a rotation frequency $\Omega = 33.5$ Hz. The blue squares show the results from the Monte Carlo trajectory simulations, the red lines are smoothing curves. Note that this effect results in a relative signal reduction of fast molecules for high densities. Therefore, it cannot be misinterpreted as the real collision signal, but could only mask the sought-after effect. The simulations are performed for CH_3F

and ND_3, the two molecule species we use for the collision measurements.

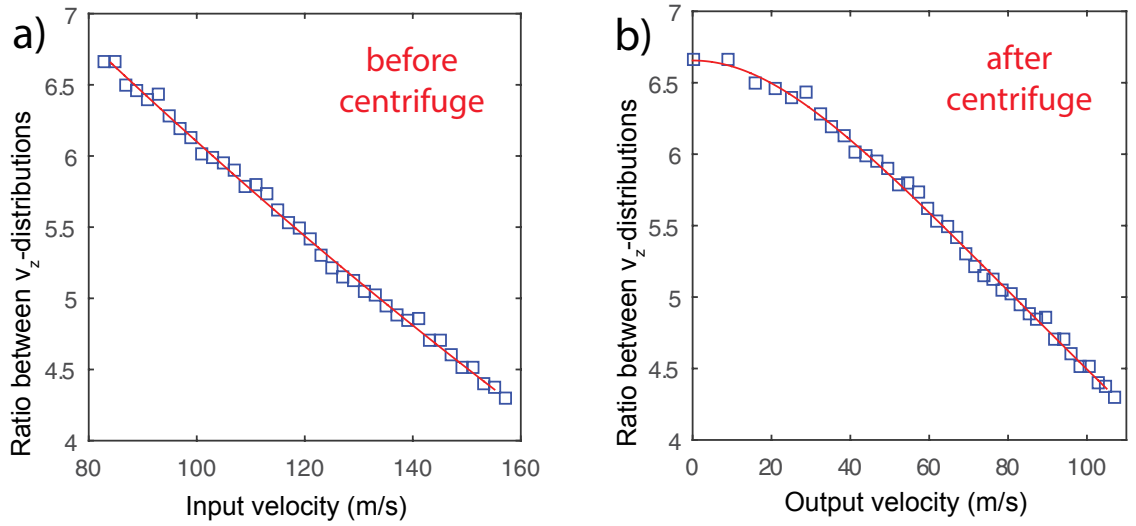

Figure 3.17: Simulated point-by-point ratios of velocity distributions, for high or low guiding voltage, in blue. Solid red lines are smoothing curves. a) shows the ratio for the input distributions, b) the ratio after the centrifuge for the decelerated beams.

3.3.4 Collision measurements

We are now prepared to take data that shows collisional loss for slow molecules. Fig. 3.18 shows the measured point-by-point ratios for the velocity distributions recorded for guiding voltages of 10 kV and 1 kV and consequently different molecule density in the guide. Here, the examined molecule is CH_3F, cooled in the buffer gas cell in the effusive regime. The data in red, blue, and green show the ratios for molecule density differences in the guide of $7.7 \times 10^8\,\mathrm{cm}^{-3}$, $1.8 \times 10^9\,\mathrm{cm}^{-3}$, and $2.4 \times 10^9\,\mathrm{cm}^{-3}$, respectively. The different density differences were obtained by varying the molecule flux into the buffer gas cell, but keeping the same voltages on the connection guide for high and low densities. The simulated velocity distribution ratio without collisional losses P_0, as shown in Fig. 3.17b, is shown by the black dashed line in Fig. 3.18, normalized to fit the high velocity tail of the experimental data. For all molecule densities, a clear signal of velocity dependent loss is visible. This effect is also more pronounced for higher densities. The shape of the ratios P can be described by the simple model $P = P_0 \exp(-\alpha \cdot k_{\mathrm{th,loss}} \cdot n \cdot L/v_z)$, where $k_{\mathrm{th,loss}}$ is the theoretically expected loss rate, n the molecule density difference, L the total effective distance the molecules cover inside the guide, and α the only free fit parameter. Using this model, we fit to the data to find the solid red, blue and green lines in the Fig. 3.18. With an averaged dipole moment for the internal state distribution of CH_3F of $d_{CH_3F} = 0.56\,\mathrm{D}$, using the process described in sec. 3.3.1,

the theoretical expected loss rate is $k_{\text{th}}^{\text{CH}_3\text{F}} = 7.7 \times 10^{-10}\,\text{cm}^3/\text{s}$ at an average collision energy $0.8\,\text{K} \times k_B$,with the Boltzmann constant k_B. The fit gives a value of $\alpha^{\text{CH}_3\text{F}} = 1.4 \pm 0.1$, deviating from a perfect fit to theory by 40%.

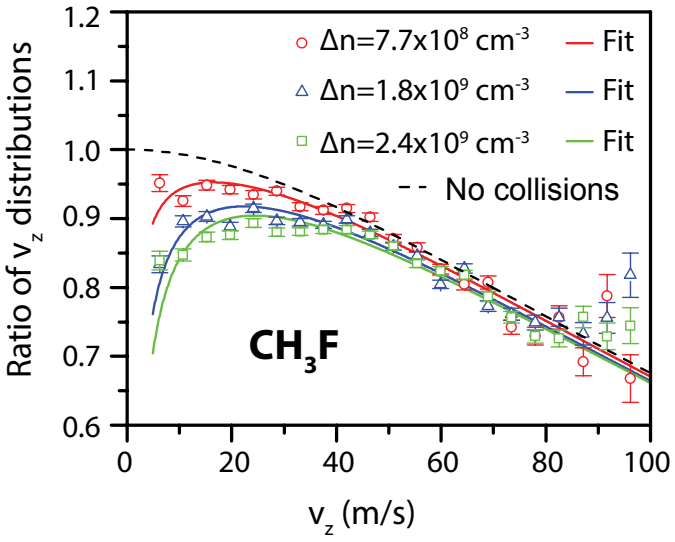

Figure 3.18: Collision measurement for CH_3F. The black dashed curve shows the theoretically expected curve without molecule-molecule collisions due to velocity dependent filtering. The other curves are obtained by taking point-by-point ratios of velocity distribution measured at different molecule densities, set by switching the guiding voltage at the connection guide between 10 kV and 1 kV. The density differences for the red, blue, and green curves are $7.7 \times 10^8\,\text{cm}^{-3}$, $1.8 \times 10^9\,\text{cm}^{-3}$, and $2.4 \times 10^9\,\text{cm}^{-3}$, respectively. The densities are adjusted by changing the molecule flux into the buffer gas cell. The solid lines are fits to the data with one free parameter. Error bars depict 1σ statistical errors.

The same measurement can be performed for ND_3. The results are shown in figure Fig. 3.19. Here, the averaged dipole moment is $d_{ND_3} = 0.77\,\text{D}$ and the expected loss rate $k_{\text{th}}^{\text{ND}_3} = 1.3 \times 10^{-9}\,\text{cm}^3/\text{s}$ at an average collision energy of $1.1\,\text{K} \times k_B$. The data was taken for a density difference of $2.1 \times 10^9\,\text{cm}^{-3}$. The fit to this curve gives $\alpha^{\text{ND}_3} = 1.6 \pm 0.3$. Notably, $\alpha^{\text{CH}_3\text{F}}$ and α^{ND_3} agree within their error bars. Therefore, we attribute the main reason for this discrepancy to a global effect. This can come from an underestimation of the density of molecules in the guide, stemming from uncertainties in the calibration, or the imprecision of the theoretical models.

It is interesting to note that according to the simulations, although the total elastic cross sections are large, calculated to be $\sigma_{CH_3F}^{el} = 2.0 \times 10^{-12}\,\text{cm}^2$ and $\sigma_{ND_3}^{el} = 2.5 \times 10^{-12}\,\text{cm}^2$, the loss ratio is small: Only about 1 in 17 elastic molecule-molecule collisions lead to detectable loss.

To underline the fact that we indeed examined the long-range dipole-dipole interaction of our chemically stable polar molecules, we compare the dipolar interaction strength $V_{dd}(r) = -d^2/4\pi\epsilon_0 r^3$ to the van der Waals interaction strength

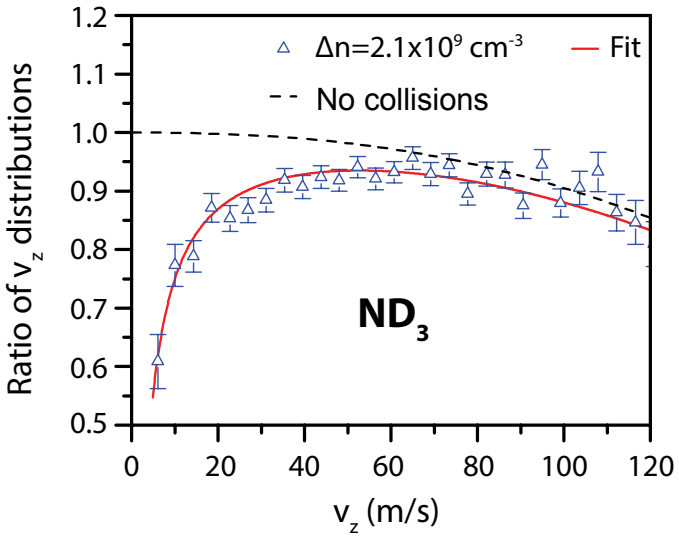

Figure 3.19: Collision measurement for ND_3. The black dashed curve shows the theoretically expected curve without molecule-molecule collisions due to velocity dependent filtering. The blue triangles show the ratio of velocity distributions taken at a density difference of $2.1 \times 10^9\,\mathrm{cm}^{-3}$. The solid red line is a one parameter fit to the data. Error bars depict 1σ statistical errors.

$V_{vdW}(r) = C_6/r^6$, with the van der Waals C_6 coefficient and the intermolecular distance r. The C_6 coefficients for CH_3F and ND_3 can be estimated to 100 and 55 atomic units, respectively, using the London formula [AF11]. At an interaction distance of 4 nm to match the observed loss cross section of $\sigma_{loss} = 0.5 \times 10^{-12}\,\mathrm{cm}^2$, the dipole-dipole interaction strength dominates by a factor of ~ 200. The measured collision rate of 10 Hz implies a thermalization rate in the order of 1 Hz for the investigated molecule sample.

4 Electrostatic microstructured trap

The Cryofuge was set up to achieve a large flux of cold and slow molecules. The successful implementation was described and demonstrated in chapter 3. The density of molecules in the electric guide was large enough that collisions could be observed even for the short time the molecules spent in the TOF guide after the centrifuge. A trap would drastically increase the interaction time between the molecules, and enable much more detailed collision studies. When the Cryofuge was designed and build, it was always optimized to produce molecules that can be trapped in the electrostatic trap that was demonstrated before [EMS$^+$11].

The setup of the trap is now successfully realized. The system and the most important features will be described in the first part of this chapter. Afterwards I will describe the efforts that were undertaken to maximize the number of trapped molecules, and thereby the molecule density for collision experiments. To conclude the chapter, I will show the measurement of the trap lifetime at different settings and demonstrate the "RF-knife" method to measure energy distributions of molecules in the trap.

4.1 Setup

First I will describe the setup used for trapping molecules cooled and decelerated by the Cryofuge.

4.1.1 Principles of the trap

A detailed description of the electrostatic trap has already been shown in [Zep13, EMS$^+$11], therefore, I will only briefly show the most important information necessary to understand the following chapter. The description follows the one given in [EMS$^+$11]. For more information about the trap, refer to [EMS$^+$11, Eng13, ZEG$^+$12, Zep13].

Fig. 4.1a) shows a schematic top view of the trap. The trap is designed to be easily integrated into the quadrupole guide setup. Molecules arrive through the quadrupole guide from the left, and reach the trapping region, where two of the electrodes bend to form the perimeter electrodes around the trapping region to create a 2D trap. This part of the trap is dubbed "ring electrode". The other two electrodes of the

quadrupole guide that are omitted in this figure are terminated when they reach the microstructure, which is schematically shown in red and blue. Above and below the ring electrode, two parallel metal coated glass substrate layers form the plates of a plate capacitor. That capacitor structure can be used to apply a homogeneous electric field ("offset field") in the trap. The two halves of the trap, divided by the black dashed line in the figure, can be controlled individually. This gives the possibility to open a loss channel for the molecules.

To keep the molecules away from the two plates, and to provide a trapping potential in the third dimension, the electrodes on the plates are microstructured to support two electric voltages with opposite polarities. A side view can be seen in Fig. 4.1c). The alternating electric potentials on the plates create a high electric field close to the plate, that decays exponentially towards the center of the trap. On the edges of the plates the electrodes are curved back into the trap to avoid escape ways for the molecules. A close-up of this region is shown in Fig. 4.1b). The shape of the electrodes and the ratios of the applied voltages are optimized to minimize the space in the trap where the electric field goes to zero. These zero field points are problematic, as molecules do not have a defined orientation relative to the electric field vector, and can flip their state from low-field seekers to high-field seekers, and get lost from the trap. This event is called Majorana flip, and is a similar mechanism as for example for atoms in magnetic traps [BMK$^+$89].

4.1.2 Layout of the setup

The trap is a necessary addition to the Cryofuge setup to achieve longer molecule-molecule interaction times to make detailed studies and further cooling possible. As both the Cryofuge as well as the trap are based on the electrostatic quadrupole guiding technique, the combination is rather straightforward. In principle, the trap is simply inserted into the guide between the exit of the centrifuge and the QMS. A side view on the additional part of the setup in the technical drawing is shown in Fig. 4.2. On the left, the cut through the centrifuge is visible. It is unchanged compared to the Cryofuge setup. The molecules exit at the center of the centrifuge, and are first guided through a differential pumping section. Subsequently, the molecules advance through a piece of guide that is formed in a shape of an 's', therefore dubbed s-piece. The voltages on this section can be controlled independently from the straight sections before and after. These voltages are used to set the cut-off velocity according to equation 3.2, following the ideas of [SMC$^+$10]. The next straight guide delivers the molecules to the trap. In doing so, it bridges a part of the vacuum chamber that is held by an elastomer that is designed to decouple possible vibrations of the centrifuge from the trap. Before and after the trap the molecules pass additional differential pumping sections, before they travel through the TOF section and are detected by the QMS.

The vacuum between the centrifuge and the trap is achieved by a turbo pump. To achieve even lower pressures, different pumping technologies are used. The trap and

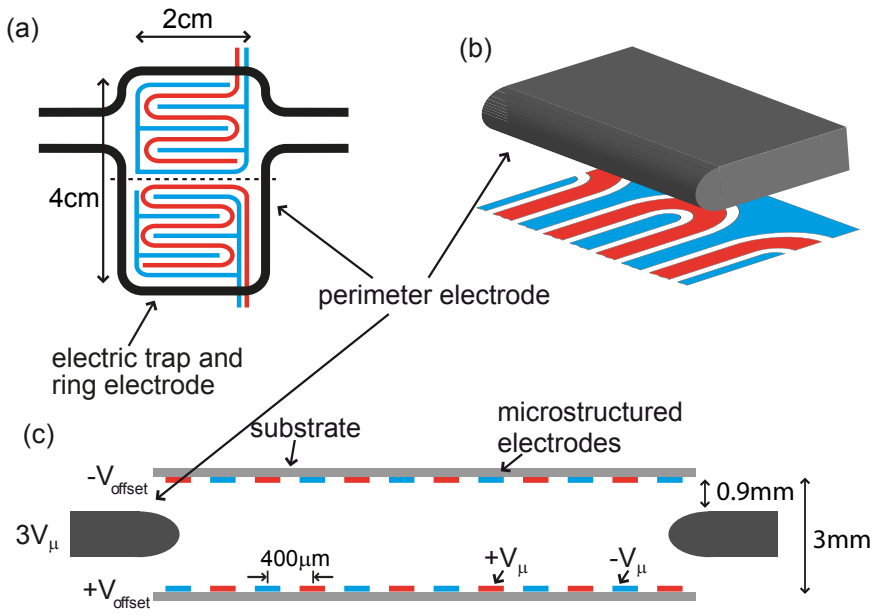

Figure 4.1: Schematic picture of the trap, from different perspectives. a) shows a top view of the trap, as it is integrated into the quadrupole guide. b) shows the detailed shape of the electrodes in the edge region of the trap. The bend of the electrodes back towards the trap center closes possible loss channels for the molecules. c) shows a side view of the trap, displaying the glass substrate plate, the microstructured electrodes charged to opposite polarities $+V_\mu$ and $-V_\mu$ lead to a high electric field close to the plates, which forms the desired box-like potential. The perimeter ring electrodes that generate the trapping potential in plane. The ring electrode voltage is adjusted to be three times the microstructure voltage. An offset voltage $-V_{\text{offset}}$ and $+V_{\text{offset}}$ is applied to the electrodes on the top and bottom electrodes, respectively. This offset produces a homogeneous field between the plates to avoid Majorana flips. Figure is taken from [EMS+11].

QMS regions are only connected to the centrifuge chamber via differential pumping sections. The vacuum is improved by an ion pump and a titanium sublimation pump each in both the trap chamber and the QMS, which are again separated from each other by a differential pumping section. A low pressure is necessary in these parts for different reasons. In the trap chamber, a high background pressure could reduce the lifetime of the molecules in the trap. In the QMS chamber, a low background pressure results in a low background count rate which is important to reach a high signal-to-noise ratio in our measurements. With this setup, we reach pressures of 8×10^{-11} mbar and below in both, the trap chamber and the QMS chamber. These pressures are fully sufficient for the planned purposes.

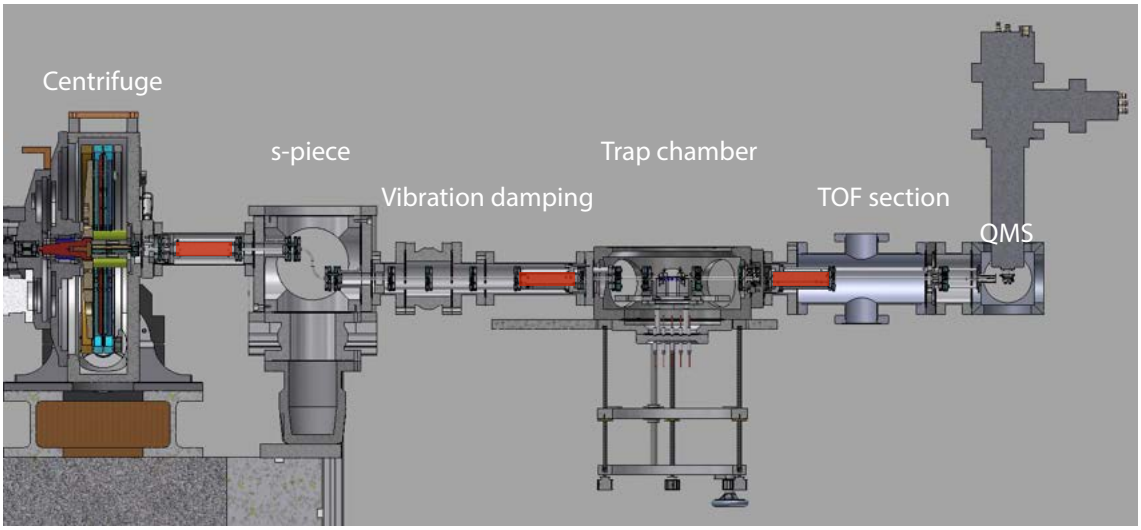

Figure 4.2: Technical drawing of the trap setup. From left to right: Centrifuge and centrifuge exit guide, s-piece guide for velocity filtering, straight guide through vibration isolation, trap chamber and trap, TOF guide, and QMS detector. Differential pumping sections are highlighted in red.

4.1.3 RF connection to the trap

To gain control over the internal states of the molecules and to measure their energy distribution in the trap, radio frequencies (RF) are necessary and are applied to two of the ground planes of the microstructure. In a previous setup used in [GPE+15], this connection was done via high voltage feed-troughs and kapton isolated copper wires. This limited the frequency that could efficiently be applied to about 6 GHz. In our setup, the RF is fed into the vacuum via a ultra high vacuum compatible SMA feed-through, and to the trap by a coaxial cable. Only the last few centimeters are bridged by single-stranded wires. As presented later in this chapter, this enables us to manipulate the molecules at considerably higher frequencies.

4.2 Characterization of the combined setup

With the new setup in place, I will now show different characterization and optimization measurements, to understand its properties and to reach its full potential. The aim is to trap the maximum number of molecules possible, which leads to a high density in the trap, and therefore a larger interaction rate. This is important for more detailed molecule collision studies.

4.2.1 Typical trapping sequence

Here I will explain the typical sequence we use in our experiments. A typical run of the experiment consists of three parts: Loading the trap, trapping and manipulating the molecules, and unloading and detecting the molecules. In between two runs, we briefly switch off all guides and the trap for 0.2 s to get rid of lingering molecules, that potentially increase the background signal for the next run.

During the loading process, all guides up to the trap are switched to guiding configuration, to achieve the maximum number of molecules inside the trap. The TOF guide between the trap and the QMS is set in guiding configuration, but with a high offset compared to the trap. Therefore, molecules that are slow enough to be trapped are still reflected at the gap between trap and guide. Faster molecules, however, that cannot be trapped, can still be guided towards the detector. This effect of reflecting slow molecules at a gap in the guide will be explained in sec. 4.2.2. It will be used to maximize the number of trapped molecules, while having access to the molecule signal during the full experimental sequence. The signal of molecules that pass straight through the trap is referred to as "straight signal", and can be used as reference to understand long term drifts of the system during the day as it does not depend on the settings during trapping.

To go from the loading to the trapping configuration, the guide in front of the trap is switched off. This stops molecules from reaching the trap, and provides an offset voltage in the gap between the guide and the trap. During trapping, the voltages on the trap can be changed when switching from loading to trapping. This can be used to increase the trap depth, and therefore the lifetime. The trapping time is freely adjusted, or even completely omitted.

During the unloading process, the voltages on the TOF guide are set to fit the trap voltages. Molecules can escape the trap through the TOF guide towards the QMS. The voltages and unloading time are adjusted to maximize the resulting signal for a given measurement. To measure velocity distributions of the molecules coming out of the trap, the TOF guide is switched on and off multiple times during the unloading process. With this technique, the rising signal that contains the TOF information to calculate a velocity distribution can be obtained several times per experiment run, which ultimately leads to a decreased measurement time, or smaller statistical error bars.

For some of our measurements, the signal is rather small, and we have to carefully pay attention to background signal. Unfortunately, it is not sufficient to determine the count rate on the QMS while the system is switched off: the background count rate also depends on how many molecules have reached the detection chamber, or even the trap chamber, in previous experimental cycles. Therefore, in a sequence of repeated measurements, the background can change over time. To clearly distinguish trapped signal from background, we add another run to the experiment, which is called "half trap measurement". For that, we repeat the same sequence again,

but only one half of the trap is switched on. On the other half, below the black dashed line in Fig. 4.1a), all microstructure electrodes are grounded, and therefore cannot provide a trapping potential. The number of the molecules reaching the trap and QMS chamber as straight signal, however, is identical. The difference in the unloading curves for the full trap and half trap measurements is used as pure trapped signal. Tab. 4.1 shows a short summary of the different parts of the sequence.

	Guides before trap	Trap structure	TOF guide
Loading	On, no offset	On/Half On	On, with offset
Trapping	Off	On/Half On	On, with offset
Unloading	Off	On/Half On	On, no offset
Recover	Off	Off	Off

Table 4.1: Summary of the guide settings for a typical measurement run. Offset is always defined compared to the trap voltage. The "Half On" setting of the trap is used to accurately measure the background count rate, if necessary. "Recover" is used to reset the system to its low background count rate, and to expel all the molecules from the guides before the next run.

Fig. 4.3 shows the raw signal of a typical measurement sequence. The loading time is set to 6 s. The fast signal increase within about 100 ms is from the time-of-flight of the molecules that have to pass the guides and the trap before they can be detected by the QMS. Afterwards a slower increase on a timescale of about 2 s is visible. This is generated by the build up of molecule density in the trap, that can affect the QMS count rate as molecules manage to escape the trap. For the last seconds of loading the trap, the build-up of molecule background in the QMS chamber due to the straight signal leads to a slowly increasing signal.

After loading, the molecules are briefly trapped for 0.1 s. The signal rapidly drops as soon as the guide before the trap is switch off, and the straight signal is extinguished.

After 6.1 s the offset to the TOF guide is set to zero, and molecules are guided towards the QMS. The slowly decreasing signal during the 6 s of unloading results from the slowly emptying trap. After the short recovery time, the half trap run is started. Here, the straight signal is smaller, as the build-up of trapped molecule signal is missing. All the molecules in the trap get lost in the grounded half of the trap. The small slope on the signal level stems from the increased background count rate due to the straight signal. The unloading signal is much smaller as well, as the trap is already empty and only the background is detected, as intended.

4.2.2 Electric potential offset between quadrupole guides

In the previous section it was already mentioned that the gaps between the electric guides can lead to losses of the molecules. While the straight as well as the bent

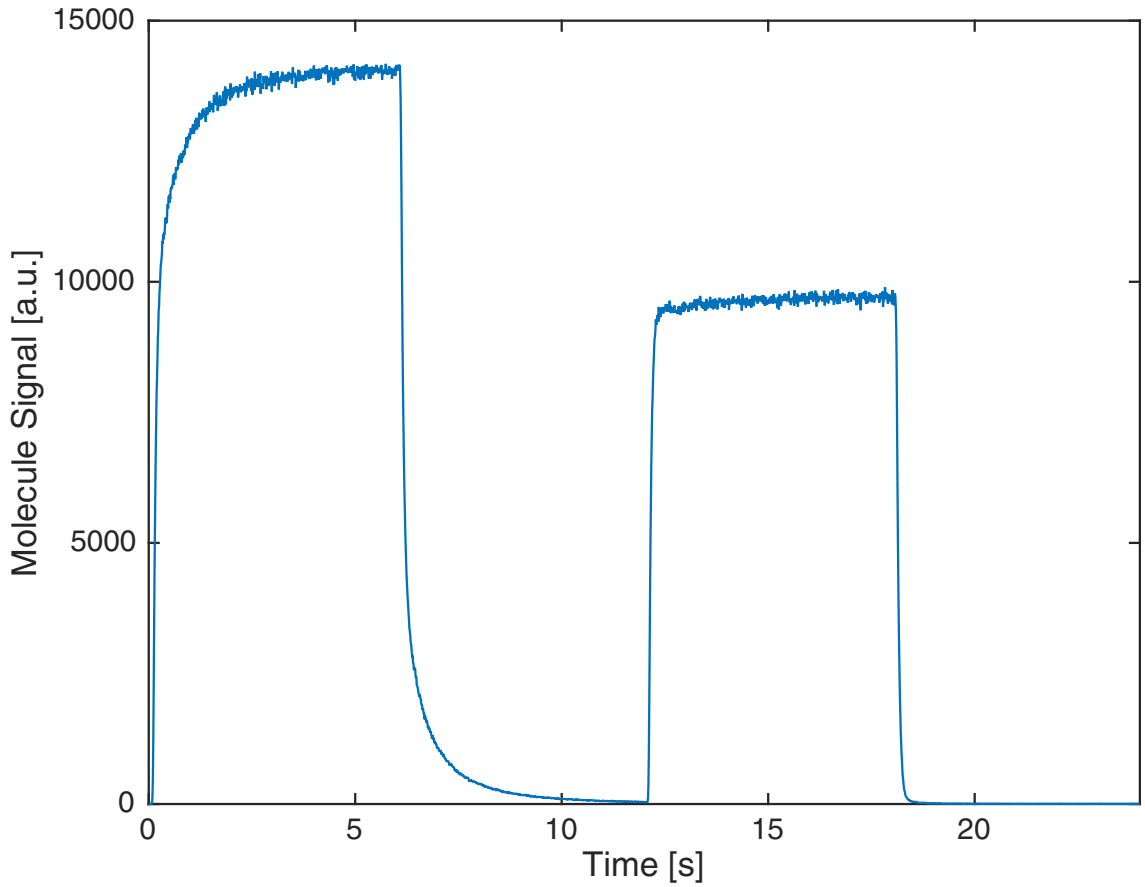

Figure 4.3: Raw signal for a typical experimental run. During the first 6 s, the straight signal is recorded at the QMS. After a brief trapping time of 0.1 s, the unloading signal is detected for 6 s. After 0.2 s recovery time, the same sequence is repeated as half trap measurement.

guide have essentially an efficiency of 100% excluding velocity filtering, molecules are prone to be lost at the gaps between two consecutive guides, especially when their longitudinal velocity becomes comparable or even smaller than their transversal velocity. This effect does not only depend on the geometry of the electrodes in the gap region, but also on electric potentials between the different parts of the guide.

Fig. 4.4 shows the distribution of the electric field strength transverse to the guide. Voltages between neighboring electrodes are 8 kV. For easier visualization, (a) shows the plane that intersects the guide in red, for which the distribution is depicted in color code in (b). As the plane is far away from the gap, it shows the undisturbed potential surface in quadrupole guiding configuration. The molecules follow the electric field strength minimum along the center line between the electrodes. As the guide is translational symmetric, the molecules can move freely along the guide.

The picture changes when the molecules approach a gap. Fig. 4.5 shows the electric field strength distribution in a plane parallel to the guides, see (a). Both of the

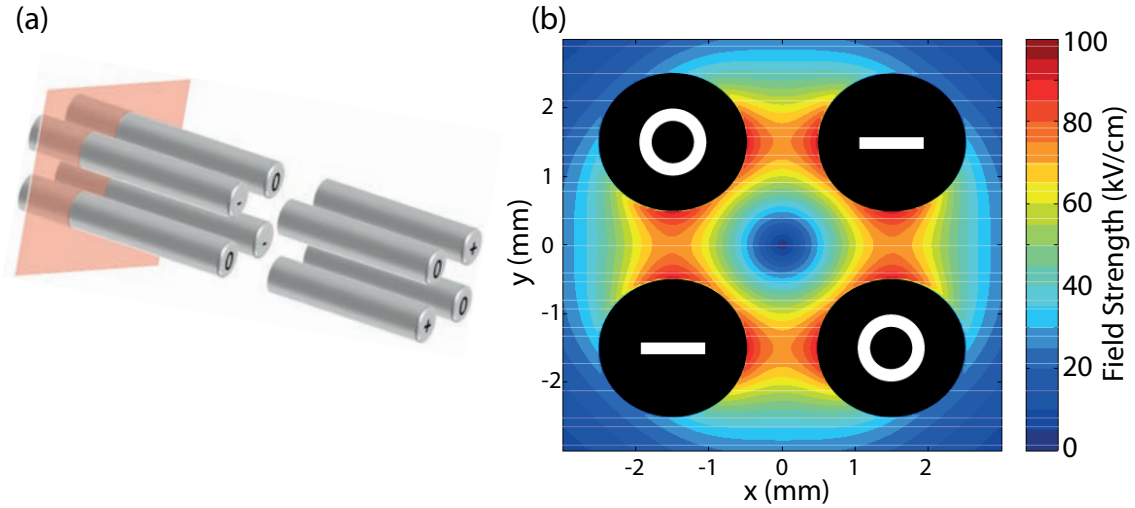

Figure 4.4: Electric field strength distribution in the guide. a) shows the plane perpendicular to the guide, far away from the gap. b) shows the electric field strength distribution in this plane, in color code. The guiding "tube" in the center of the four electrodes is visible.

guides are operated at quadrupole guiding configuration, with an identical trap depth. However, the voltages on the guide are not symmetric around the ground potential, but are offset with a different polarity. This potential difference over the gap leads to an electric field between the two parts of the guide, which appears as potential barrier for the low-field seeking molecules. Fig. 4.5b) clearly shows this barrier, which hinders molecules to pass from one guide to the next. The height of this barrier can be adjusted by setting the voltage offset difference between the guides.

This effect was known previously, but did not have an impact on the experiments because the longitudinal kinetic energy of the molecules was typically large compared to the barrier height. In the figure, it is also apparent that the potential barrier in the gap is smaller than the depth of the quadrupole potential, even for large offset fields as shown here. Therefore, only slow molecules are strongly affected by the barrier. As slow molecules are supposed to be trapped, it is important to investigate this effect, and to optimize our settings for maximum flux of slow, trapped molecules.

To verify the effect of the barrier, we scan the offset voltage in the gap in the connection between the centrifuge and the trap. For each setting, we record the number of molecules in the straight signal and the number of molecules trapped for 100 ms. As the trap depth is smaller than the maximum kinetic energy of the molecules, the measurement of trapped molecules is effectively a measurement on slower molecules. Apart from the offset voltage, all parameters for the measurement are kept constant. The result is shown in Fig. 4.6. All curves are normalized. Blue and red crosses show the trapped signal and straight fly-through signal, respectively. The error bars show the 1σ error due to counting statistics. To exclude other effects,

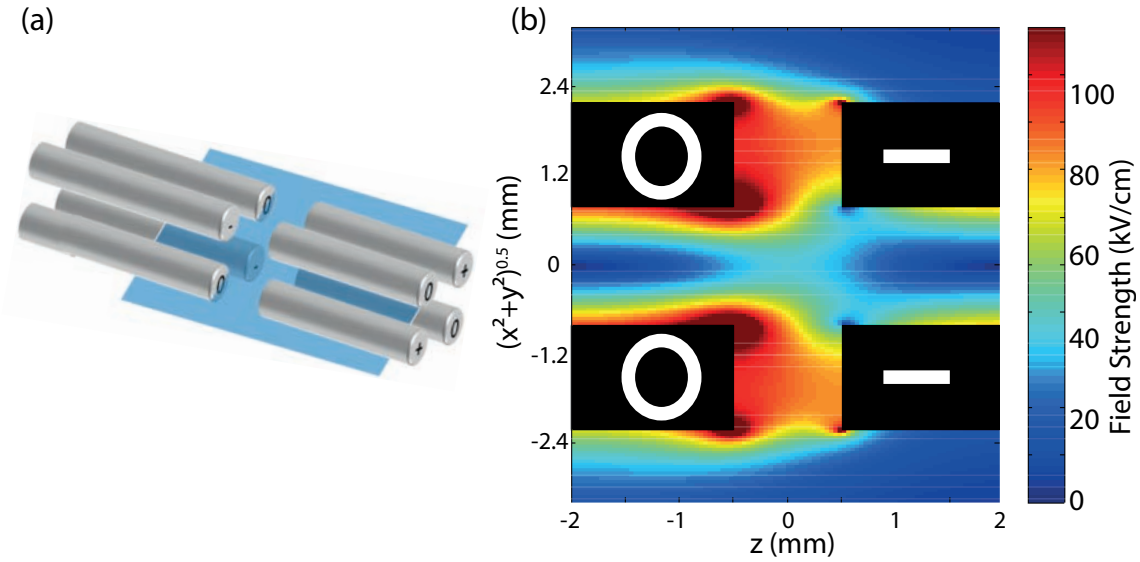

Figure 4.5: Electric field strength distribution in the guide. a) shows the plane parallel to the guide, across the gap. b) shows the electric field strength distribution in this plane, in color code. The saddle point of the potential that separates the two guides is clearly visible. This effect comes from a potential drop over the gap, even though both of the guides are in guiding quadrupole configuration, with identical depth.

the measurement was repeated, with several parameters changed. Fig. 4.6a) shows the results taken with CH_3F, a positive voltage difference across the gap, and a centrifuge rotation frequency of 28 Hz, while the data in Fig. 4.6b) is taken with CF_3CCH, a decrease in electric potential and a centrifuge rotation frequency of 22 Hz. Data at identical offset voltages are taken at different times to check for long term drifts in the setup. A slight offset on the x-axis is added in the plot for these points for better visibility.

Qualitatively, the results of the two measurements agree. Both show a maximum of the signal for trapped as well as for guided signal without offset voltage. Additionally, it becomes clear that the slower molecules are affected more severely than than faster ones. Quantitatively, small differences are visible between the two measurements, which might be explained by the different dipole moment or velocity distributions, but detailed analysis or simulations were not performed.

With this knowledge in mind the following experiments were performed to optimize the signal. During the loading time of the trap, all guide voltages between the cryogenic cell and the trap were chosen to avoid an electric potential offset, while an offset was applied between the trap and the exit towards the TOF guide. To achieve best possible trapping, we applied an offset both at the input and the exit guide during trapping. For unloading the trap, the offset on the exit guide was set to zero.

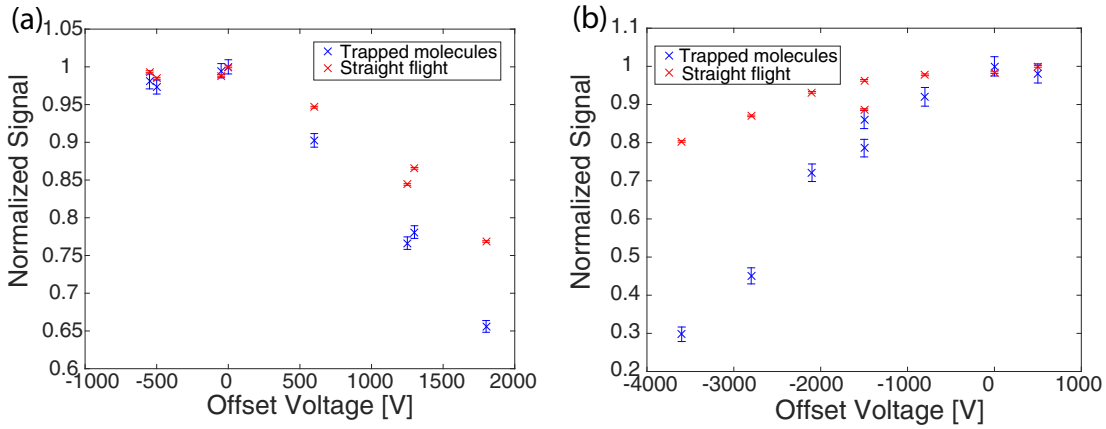

Figure 4.6: Offset voltage scan at the gap between the guide from the centrifuge and the trap. The trapped and the straight signal are depicted in blue and red, respectively. In a), data was taken with CH_3F, a positive voltage difference across the gap, and a centrifuge rotation frequency of 28 Hz. b) was measured with CF_3CCH, a negative voltage difference across the gap, and a centrifuge rotation frequency of 22 Hz.

4.2.3 Offset electric fields in the trap

As mentioned before in sec. 4.1.1, points in space with very small electric fields are problematic, as molecules can go from their trapped low-field seeking state to an untrapped high-field seeking state. In the electric guide this is not an issue, as the electric field minimum is only in the center region, and electric field strength increases rapidly towards the electrodes. The volume where Majorana flips can happen is therefore very small. In the trap, however, the electric field strength in most of the trap volume is designed to be small. To avoid Majorana flips there, a potential is applied between the two capacitor plates, producing a homogeneous field in between.

To test this effect and further optimize the number of trapped molecules, we vary the electric field in the trap by changing the voltage offset between the two plates. This voltage offset is given relative to the voltages used on the microstructured electrodes. Here, these voltages were 0.6 kV and −0.6 kV on the positive and negative electrode, respectively. An offset of 5 % means, that the voltages on one plate are 0.57 kV and −0.63 kV and on the other plate 0.63 kV and −0.57 kV. We will refer to this a trap voltage of 0.6 kV±5 %. Therefore, the average potential difference between the two plates is 60 V. This potential drop then generates an electric field to avoid Majorana flips. The other experimental parameters were kept constant. The fluxes of CH_3F and helium into the buffer gas cell were 0.08 sccm and 0.5 sccm, the voltage differences on the guides were set to 3 kV, the loading and unloading time were both set to 6 s, and the trapping time was set to zero.

Fig. 4.7 shows the offset scanned up to 40 % for both polarities. It is clearly visible

that the number of molecules in the trap is reduced, if no offset is used, and the electric field strength between the two plates is zero. For higher offsets, we cannot detect any variations of molecules numbers within the error bars.

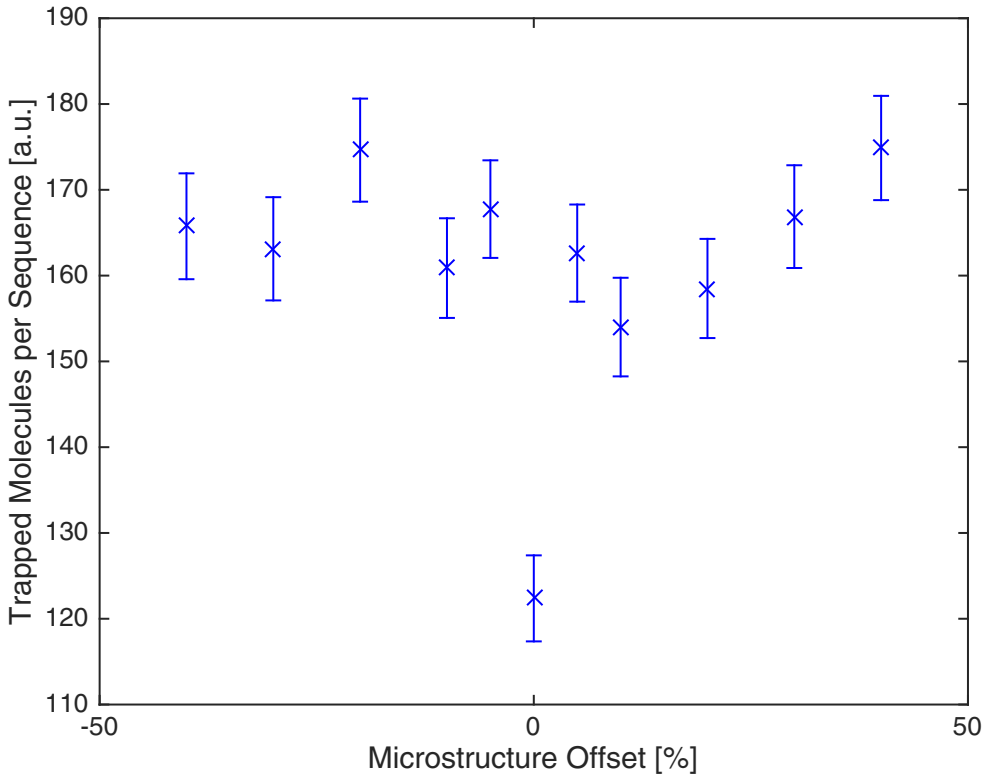

Figure 4.7: Scan of the voltage offset between the to trap plates. Electric fields produced by this offset are necessary to avoid Majorana flips.

Fig. 4.8 shows the same scan as before, but over a smaller range. For zero or small offset fields, the number of trapped molecules is reduced, but as soon as the offset is 3 % or higher, the molecule number is constant. The direction of the applied field does not have a significant impact, as expected.

For the rest of this thesis, an offset will always be used, and is varied between 5 % and 30 %.

4.2.4 Optimization of molecule flux, buffer gas flux and centrifuge rotational speed

The last optimization step is the adjustment of the molecule and buffer gas fluxes into the cryogenic cell and the rotation frequency of the centrifuge. The buffer gas flux and the centrifuge speed have to be adjusted simultaneously. From previous

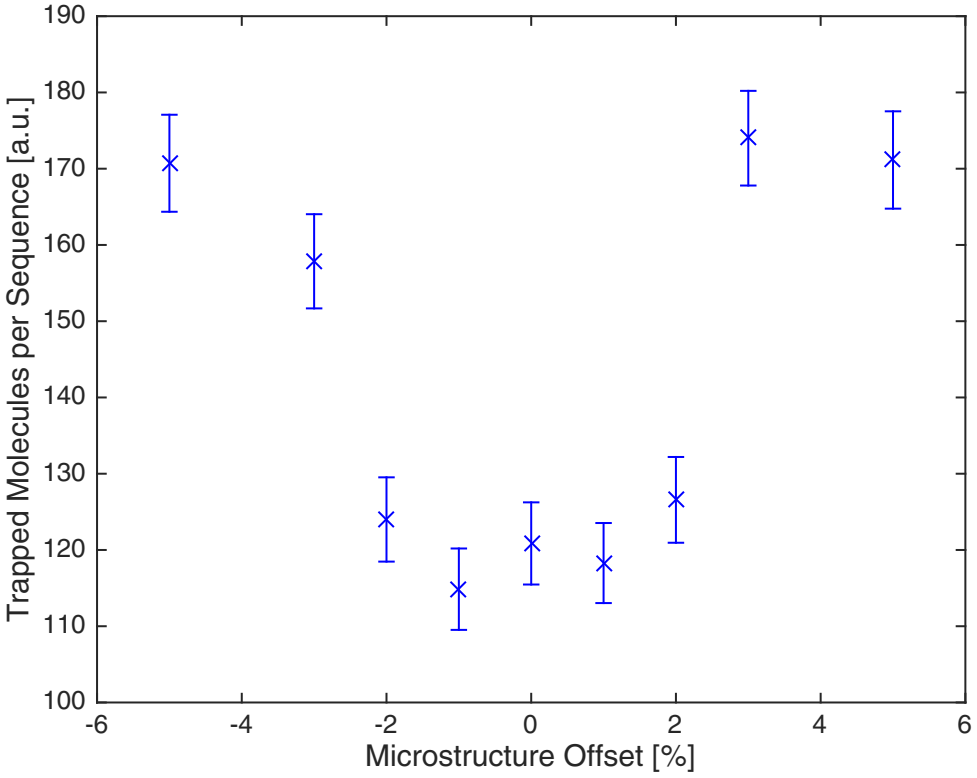

Figure 4.8: Scan of the electric field strength in the trap. An offset of 3 % is enough to avoid Majorana flips, higher offsets do not increase the number of trapped molecules any further.

experiments with the buffer gas source and the Cryofuge in sec. 3.2.2, we know that the magnitude of the buffer gas flux can strongly influence the velocity distribution of molecules in the guide. The optimization shown here is performed for CH_3F, at a buffer gas cell temperature of 7.1 K, a trap voltage of 1.2 kV and a guiding voltage difference of 4.6 kV. Whenever the molecule species or any of the relevant experimental parameters are changed, this optimization is repeated.

Fig. 4.9 shows the straight signal versus the centrifuge rotation speeds, for various buffer gas densities. Each of the curves shows a clear peak. For higher buffer gas densities, the peak shifts to higher rotational frequencies, as a stronger deceleration is necessary to compensate the additional boosting. Moreover, for higher densities, the signal decreases more and more. This suggests that smaller buffer gas densities would be best suited to produce maximum molecule flux. However, for very small very low buffer gas densities molecules cannot be thermalized to the cell temperature. This effect has been discussed in chapter 2. Additionally, the buffer gas cell cannot be operated stably at very low buffer gas densities, as molecule ice forms very quickly. This is why for the data taken at lowest buffer gas density of $3.4 \times 10^{14}\,\mathrm{cm}^{-3}$, the

curve does not look smooth. As a compromise between maximum signal per run, and long measurement times and signal stability, a typical helium density of about $1.3 \times 10^{15}\,\mathrm{cm}^{-3}$ is used, corresponding to the green curve.

The data shown in Fig. 4.10 was taken for the same experiment, but here the number of trapped molecules per run is plotted. Qualitatively, the trends follow the ones for the straight signal, however, the peak positions are shifted to higher centrifuge rotation speeds. This comes from the fact that the trap can only capture the slowest molecules out of the beam, and therefore, a stronger deceleration is beneficial even on the expense of total straight signal. As we are interested in trapped molecules for most of our measurements, the peak positions from this measurements are usually used.

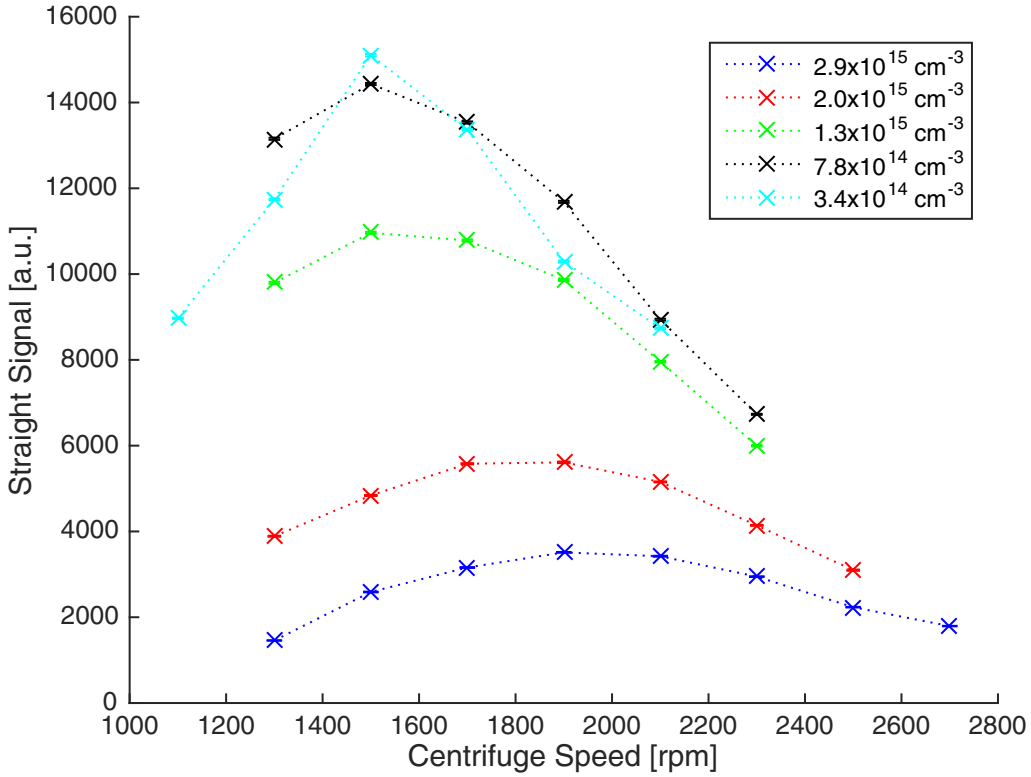

Figure 4.9: Molecule signal guided straight through the trap versus the centrifuge rotation speed, taken for different helium densities in the buffer gas cell. The acceleration effect of higher buffer gas densities is apparent from the shifting peaks of the curves. The reduced signal for high buffer gas density is similar to the measurements on the Cryofuge setup.

The molecule flux can be optimized separately, as it only weakly affects the velocity distribution of the molecules in the guide. This is known from previous velocity distribution measurements, and was cross checked by centrifuge rotation frequency

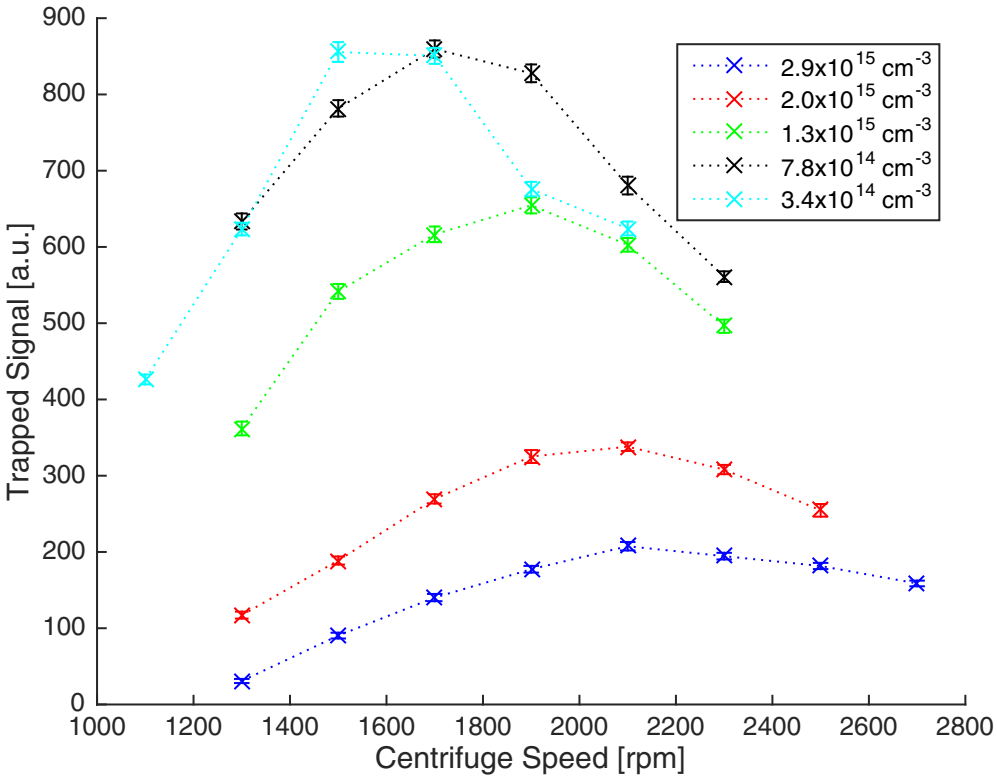

Figure 4.10: Signal of trapped molecules per experimental run versus the centrifuge rotation speed, taken for different helium densities in the buffer gas cell. The trend of reduced signal and shifting peak looks similar to the straight signal. The peak appears at higher rotation speeds due to the selection of slower molecules by the trap depth.

scans at various molecule fluxes. Fig. 4.11 shows the number of molecules guided and trapped depending on the molecule flux into the buffer gas cell, in red and blue, respectively. For easier comparison, both curves are normalized. The error bars show a one sigma statistical error due to counting statistics.

For small molecule flux, the signal level is roughly proportional to the molecule flux into the cell, and the ratio of trapped to guided molecule number is constant, as would be expected for an unchanged velocity distribution. For higher molecule flux however, the signal levels off and even decreases for higher flux, as the higher flux of warm molecules amplifies the boosting effect out of the buffer gas cell and accelerates molecules so much that they cannot be guided any more. Additionally, the trapped to guided molecule ratio changes. This can be explained from the collision effect in the guide as seen in section sec. 3.3, which is stronger for slow, trappable molecules.

Another issue of higher molecule flux into the cell is the shortening of measurement time due to faster ice formation. Due to this effect, most measurements are

performed at a molecule flux of 0.2 sccm, slightly below the peak value found in Fig. 4.11.

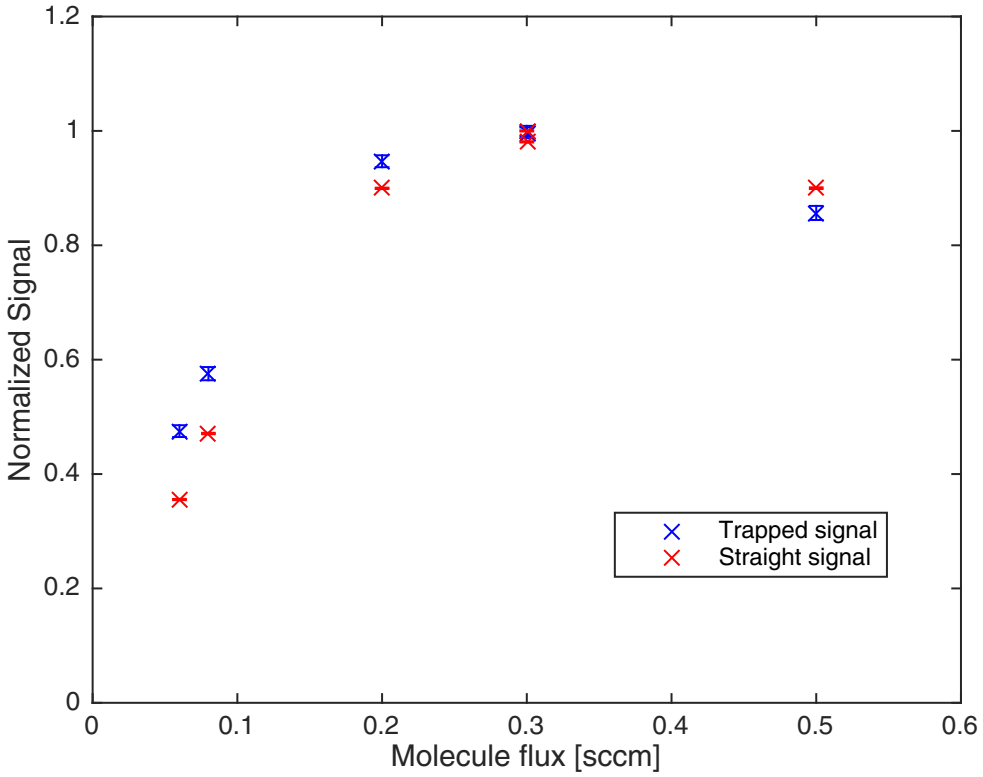

Figure 4.11: Count rate for guided and trapped molecules versus the molecule flux into the buffer gas cell, in red and blue, respectively. For low flux, the signal is linear in molecule flux. The decrease for higher flux is due the onset of stronger boosting. The trapped signal is affected stronger than the guided signal, as boosting is more pronounced for slow molecules, as well as due to the molecule-molecule collision effect in the guide depleting the slow molecules.

4.2.5 Performance after optimization

Up to now, all optimization results showed the improvement of the optimization steps only qualitatively. For future operation, knowing the absolute number of molecules in the trap, and thereby their density, will be crucial. Therefore, we use the settings found during the optimization process, and the QMS calibration as described in chapter 3. With the optimum settings, we can routinely reach about 2×10^7 molecules in the trap. As the trap volume is fixed to 2.4 cm^3, this results in a density of $8 \times 10^6\,\mathrm{cm}^{-3}$. This density is lower than the density of slow molecules in the guide of $1 \times 10^9\,\mathrm{cm}^{-3}$ as found in chapter 3. However, the average molecule

kinetic energy here is even lower due to the filtering of the trap, and the investigation time is prolonged due to the full 3D trapping. Below we will examine these two properties of the trapped molecule sample in greater detail.

4.3 Trapping and investigation of molecules

After rigorous optimization of the experimental parameters, we are now ready to examine the lifetime of the molecules in the trap, one of the most important figures of merit of any trap. For us, a long lifetime is particularly important to trap the molecules long enough that they have time to undergo collisions. In the long term, a long lifetime will also be necessary to be able to implement the envisioned Sisyphus cooling scheme [ZEG+12].

Additionally, we will investigate the behavior of the molecules in a RF-field. It allows us to measure the energy distribution of molecules in the trap, using the RF-knife technique. Later, understanding the properties of the RF are also important to address different rotational states of the molecules.

4.3.1 Trap lifetime

We measure the trap lifetime by repeating the same experimental sequence as explained in sec. 4.2.1, and vary the trapping time. As test molecule we use CH_3F, the other parameters are optimized for maximum signal as explained in the previous chapters. Additional to this maximum signal measurement, we also perform lifetime measurements with a reduced guiding voltage at the s-piece, to selectively only load the slowest molecules into the trap. Thereby we expect to achieve longer trap lifetimes.

Fig. 4.12 shows the results of these measurements. The trapping times used are 0.01 s, 0.1 s, 0.3 s, 1 s, 3 s, and 10 s. To be able to compare the outcome for the different s-piece voltages, all curves are normalized to the value with a trapping time of 0.01 s. The figure shows the data for s-piece voltages of 0.5 kV, 1.5 kV, and 5.5 kV as blue, red, and green crosses, respectively. The error bars depict the one sigma statistical error. The solid lines are exponential fits, shown in their respective color.

The decrease in lifetime is clearly visible for increasing s-piece voltage. The 1/e lifetimes obtained from these fits are 3.0 s, 1.6 s, and 0.9 s from lowest to highest voltage. For the 1.5 kV and 5.5 kV measurements, the error bars are small enough to see a clear deviation from the simple exponential decay model. The reason for this deviation is not yet fully understood, and needs additional investigation. A possible explanation would be the presence of molecules in different velocity classes or internal states, each with a distinct lifetime. An alternative reasoning could be

a collision-limited lifetime, that effects the molecules mostly in the beginning of the trapping, when the densities are highest.

The inset in Fig. 4.12 shows how the trapped molecule signal level changes with the applied voltage on the s-piece. The longer lifetimes are traded off for a smaller signal. In particular, the longest lifetimes are achieved with the lowest voltages, where only about 1 % of the signal is left compared to the highest voltages used.

In the future, the limitation of the short lifetime can be overcome by cooling the molecules. A lifetime of 27 s has been demonstrated in the same type of trap by applying Sisyphus cooling [ZEG+12].

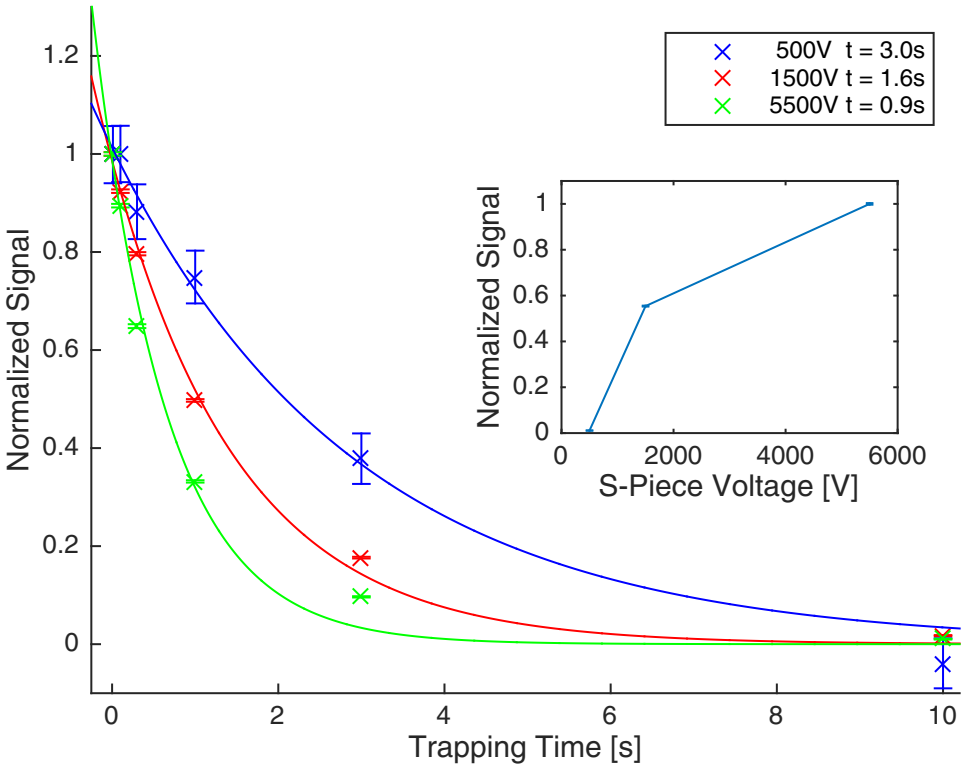

Figure 4.12: Trap lifetime measurements for different molecule energy distributions, set by the s-piece voltage of 0.5 kV, 1.5 kV, and 5.5 kV in blue, red, and green, respectively. Crosses are measurements after various trapping times, shown with one sigma error bars. Solid lines are single exponential fits. Lower average energy of the molecules leads to increased trap lifetimes. The inset depicts the signal level after the shortest trapping time for the different s-piece voltages.

4.3.2 Energy selective RF depletion

To understand the energy distribution of molecules in our trap we use energy selective RF depletion that has been used previously [ZEG+12], and is similar to the

technique used for forced evaporation of atoms in a magnetic trap [DMA$^+$95]. In our system, the trapped and untrapped M-levels of a $|J, K>$ state are coupled at high electric fields by a radio frequency (RF). Only if trapped molecules have a high enough kinetic energy to reach these fields, they can be pumped to untrapped states by the RF. When we compare the measurement with and without RF applied, we can infer the number of molecules with an energy high enough to reach the electric fields necessary to make a resonant state transfer. Unfortunately, the resonant electric field strength depends on the internal state of the molecule, and we cannot directly obtain the real energy distribution. However, the molecules after buffer gas cooling are mostly in few, energetically low-lying rotational states, and this RF depletion method can still provide an idea of the energy distribution.

Fig. 4.13 shows the result of a typical RF depletion measurement. To be sure that all molecules with a sufficient energy have enough time to be pumped to a high field seeking state and consequently be lost from the trap, we vary the time the RF is applied to the trap, and record the depletion of the molecule signal. The RF times used are 0 ms, 10 ms, 20 ms, 50 ms, 100 ms, 200 ms, 500 ms, and 1000 ms. The trapping time is always kept at 1000 ms. Additionally, the RF is varied in several steps between 1 GHz and 15 GHz. From the figure it is apparent that about 200 ms to 500 ms are necessary to fully saturate the signal, or even longer for the smallest frequencies applied.

To see if the RF really selectively depletes the molecules with the highest energy, we measure velocity distributions of trapped molecules, when the RF is or is not applied during the trapping time. We use a frequency of 6 GHz to achieve a reduction of count rate of about 50 % according to Fig. 4.13. We trap the molecules and apply RF for 200 ms.

To obtain a velocity distribution of the trapped molecules, we switch the TOF guide off and on during the unloading period several times. For each switch-on event, we retrieve a TOF signal, which can be converted into a velocity distribution. The final result of this measurement is shown in Fig. 4.14. Blue shows the signal for a non-depleted distribution, red with the RF applied. Error bars give a statistical error of 1σ, both curves are normalized. Clearly, fast molecules are efficiently ejected from the trap, while slow molecules are hardly affected. This supports the statement that RF can remove fast, high energy molecules from the trap. The cut-off is not sharp because molecules still populate several different internal states, which affects the relation between velocity and energy in the electric field. This means the cut-off velocity is different for each internal state.

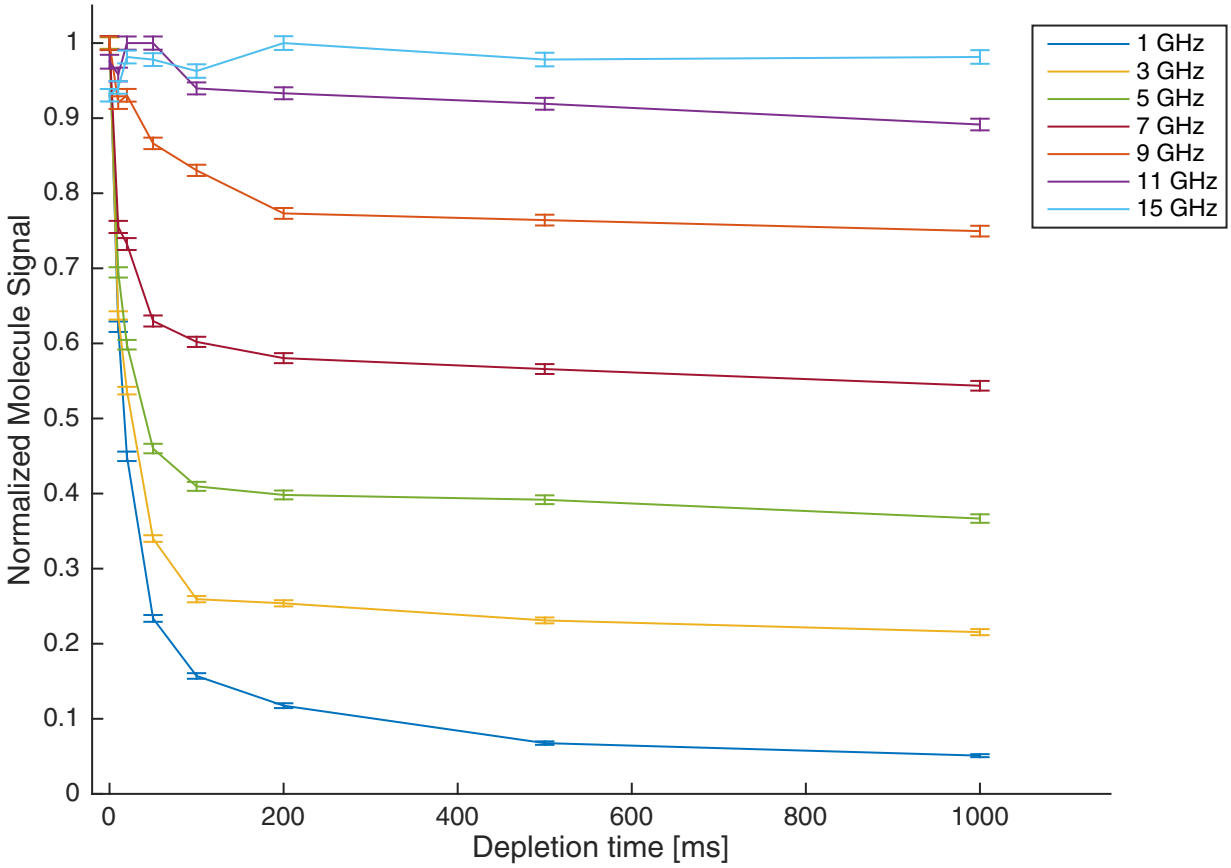

Figure 4.13: Molecule signal after one second trapping versus the time RF is applied, for various frequencies. For smaller frequencies, more molecules can be addressed, and the final signal is reduced. Full depletion takes at least 500 ms.

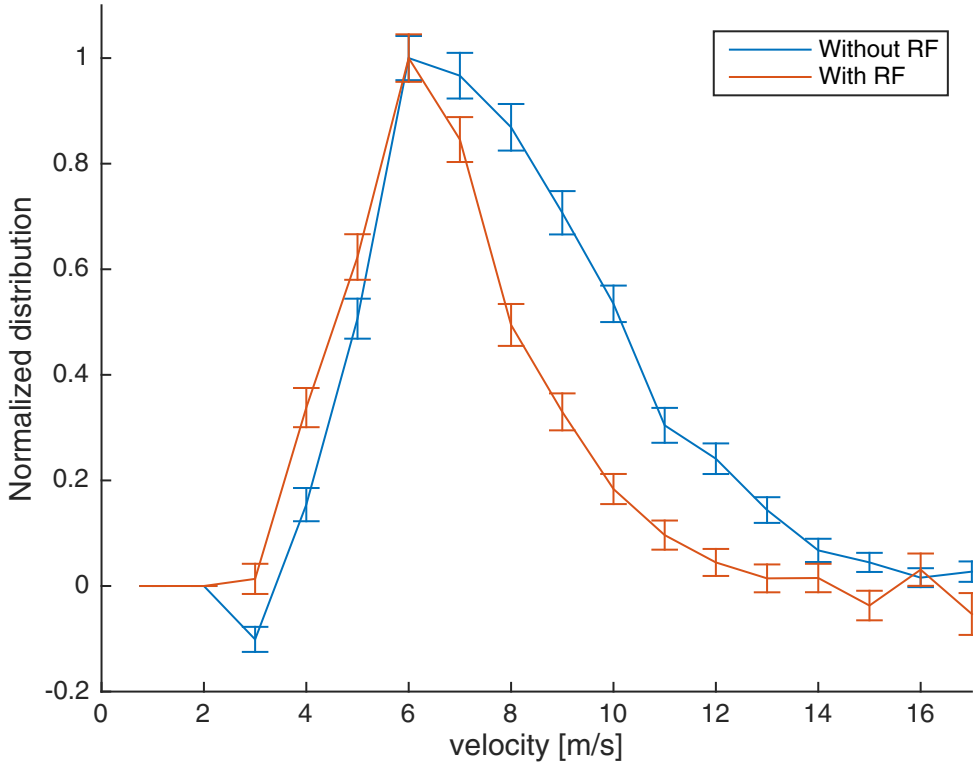

Figure 4.14: Velocity distributions of trapped molecules, with and without applied RF of 6 GHz during the trapping time in red and blue, respectively. Error bars show 1σ statistical errors. The applied RF clearly depletes the fastest, highest energy molecules, while slower molecules remain unaffected.

5 Outlook

This thesis covered three diverse topics: Simulations to understand a buffer gas cell in the effusive regime, the Cryofuge and its ability to produce a large flux of slow molecules and to investigate dipolar molecule-molecule collisions, and the extension of the setup by an electrostatic microstructured trap. All these efforts were targeted to the goal to produce slow, cold and dense samples of molecules that can be investigated and better understood. They can also serve as a starting point towards even colder and better controlled molecules, and ultimately even pave a way towards a molecular quantum degenerate gas. During the design of all the diverse parts of the experiment, the different possible applications that were pointed out in the introduction were kept in mind. It was clear that all these various prospects would rely on different kinds of molecules. Therefore, it was always sought to work as general as possible. And indeed, all the techniques shown in this thesis only rely on a strong interaction of the molecules with an electric field, and can therefore be applied to a great variety of molecules.

Optimizing the buffer gas cell In chapter 2, a simulation to understand the properties of a buffer gas cell was presented. As mentioned, this simulation can be used to optimize the buffer gas cell to a certain application. However, as these simulations were only finalized towards the end of the thesis, no optimization steps had been undertaken on the Cryofuge setup. However, a clear way to substantially increase the molecule flux and consequently the number of trapped molecules has been found. The steps towards this enhancement are currently planned. With their implementation, the investigation of low-energy molecule-molecule collision could be considerably simplified.

Molecule-molecule collisions In chapter 3 we already investigated collisions between dipolar molecules, and found a good agreement with theoretical predictions. This proved that the densities of slow molecules produced by the Cryofuge are very high, and investigations of collision cross sections of various molecules are possible. Unfortunately, the collisions could only be observed as losses from the molecule beam, and it was not possible to distinguish elastic and inelastic collisions. The important question, if or which molecules can efficiently be cooled evaporatively could not be answered, as this depends on the ratio between elastic and inelastic collision rate [KVD+96]. With the addition of the trap to the system this issue can be solved. As it was shown in the end of chapter 4, we can now distinguish molecules

with different energies, either by applying a radio frequency, or by measuring their velocities. When now first removing molecules of a certain energy class from the trap, and seeing this energy class being repopulate, we can conclude to see elastic collisions that lead to a thermalization of the trapped sample. Similarly, density dependent losses from the trap can be recorded to access the inelastic collision rate. Repeating this procedure for different molecules can reveal the ideal candidate for evaporative cooling.

Although the internal state distribution of the molecules in the electric quadrupole guide after cooling by a buffer gas cell has already been measured in this setup [WGZ$^+$16], the collision measurements were not state sensitive and could only display cumulative effects. In the trap it was demonstrated that internal states can be addressed and detected selectively [GPRZ15]. With this tool, investigating the collision cross sections of the different internal molecule states becomes feasible. These results could uncover the quantum nature of the collisions at low temperatures.

Sisyphus cooling The electrostatic trap implemented here is a duplicate of the trap described in [ZMPR09]. It generates a box-like potential for the molecules so that they spend most of the time in small electric fields, and only briefly enter regions of high electric fields at the edge of the trap. The design is optimized to trap dipolar molecules for a long time, and importantly, to implement opto-electrical Sisyphus cooling, as it was achieved in 2012 [ZEG$^+$12]. Therefore it is the next obvious step to realize Sisyphus cooling in our system as well. Some of the molecules that were decelerated and trapped have already been Sisyphus cooled before, like CH_3F [ZEG$^+$12], or are expected to be coolable, like CF_3CCH [ZMPR09]. Other molecules proposed in this paper have not been investigated yet, but posses a favorable dipole-moment to mass ratio, and can be decelerated by the centrifuge as well.

New traps for molecules Cooling the molecules to temperatures close to or even below 1 mK enables the use of different traps, like microwave cavities or optical dipole traps. Further cooling in the microstructured trap is not beneficial as the optical access in this trap is poor. For most of the envisioned further steps it is important to manipulate the molecules with lasers or more radio or microwave frequencies. Additionally the box-like trap is not well suited for runaway evaporation that has been extremely successful for atoms. The runaway cooling relies on a density increase for decreasing temperatures, so that the collision rate given by the product of density, cross section, and particle velocity is constant or even increases during cooling. For a box-like potential however the density $n = \frac{N}{V}$ is given by the particle number$N$ and the trap volume V, and constant for varying temperature. Ultimately, this would density decrease due to the inevitable particle loss during evaporation. A different trap design like a microwave trap, without a flat bottom, is therefore necessary.

New detection schemes The currently used QMS detector is a very versatile tool, and allowed us to try and test the different parts of the setup for a large variety of molecules. To do so, we only changed the mass channel at the detector. However, the detection efficiency of a QMS is poor, and makes systematic measurements with small count rates time consuming and laborious. Moreover, the detection is state independent, so that the state dependent measurements always had to rely on depletion analysis. As soon as a molecule species is chosen for further experiments, it can be worthwhile to sacrifice the versatility of the QMS for higher detection efficiencies and state dependent detection.

Currently two other detection schemes are explored in our group. The first is based on light induced fluorescence (LIF), and is designed to increase the detection efficiency for a continuous beam of slow molecules. It is expected to improve the detection efficiency for formaldehyde as currently used in that setup by a factor of 30. At the same time, LIF is state dependent, and different states can be detected by tuning the laser frequency. LIF was implemented in our group during the last year, and first characterization measurements look promising.

At the same time, a new detection method was proposed by Zeppenfeld [Zep17]. It is based on an energy transfer from a molecule to a Rydberg atom via a Förster resonance. The change of the internal state of the Rydberg atom can be detected with a high efficiency by electric field ionization. The detection efficiency was calculated to be up to 8%. Very recently, the first results showing the detection of a room temperature gas of ammonia molecules have been presented [JZ18]. A setup showing the detection of cold molecule beam from a liquid nitrogen cooled nozzle in a dense cloud of Rydberg atoms is underway.

Different molecule species All the results presented in this thesis have been taken with molecules that are chemically stable, and can be purchased commercially in a gas bottle. While this procedure is very convenient as it allows for an easy exchange between molecule species, and a simpler buffer gas cell design, some of the possible future molecule experiments might need to employ molecular radicals. In fact, the precision experiments performed in search for the eEDM work with these species already [AH18]. The precision of these measurements is limited by the interrogation time. As the molecules used there are taken directly from a buffer gas cell without further deceleration, this time is short, limited by the velocity of the molecules. The implementation of the Cryofuge, or even the trap, on such an experiment could boost the precision of these measurements, and rule out or confirm more theories about fundamental physics.

Bibliography

[AAB+18] Loïc Anderegg, Benjamin L Augenbraun, Yicheng Bao, Sean Burchesky, Lawrence W Cheuk, Wolfgang Ketterle, and John M Doyle. Laser cooling of optically trapped molecules. *arXiv preprint arXiv:1803.04571*, 2018.

[AAC+17] Loïc Anderegg, Benjamin L Augenbraun, Eunmi Chae, Boerge Hemmerling, Nicholas R Hutzler, Aakash Ravi, Alejandra Collopy, Jun Ye, Wolfgang Ketterle, and John M Doyle. Radio frequency magneto-optical trapping of caf with high density. *Physical review letters*, 119(10): 103201, 2017.

[AAH+10] K Aikawa, D Akamatsu, M Hayashi, K Oasa, J Kobayashi, P Naidon, T Kishimoto, M Ueda, and S Inouye. Coherent transfer of photoassociated molecules into the rovibrational ground state. *Physical review letters*, 105(20): 203001, 2010.

[AAK+88] A Aspect, Ennio Arimondo, R e a1 Kaiser, N Vansteenkiste, and C Cohen-Tannoudji. Laser cooling below the one-photon recoil energy by velocity-selective coherent population trapping. *Physical Review Letters*, 61(7): 826, 1988.

[ACH+10] Stephen J Asztalos, G Carosi, C Hagmann, D Kinion, K Van Bibber, M Hotz, LJ Rosenberg, G Rybka, J Hoskins, J Hwang, et al. Squid-based microwave cavity search for dark-matter axions. *Physical review letters*, 104(4): 041301, 2010.

[ADD+06] A. André, D. DeMille, J. M. Doyle, M. D. Lukin, S. E. Maxwell, P. Rabl, R. J. Schoelkopf, and P. Zoller. A coherent all-electrical interface between polar molecules and mesoscopic superconducting resonators. *Nat. Phys.*, 2(9): 636–642, September 2006, http://dx.doi.org/10.1038/nphys386.

[ADVT18] Asimina Arvanitaki, Savas Dimopoulos, and Ken Van Tilburg. Resonant absorption of bosonic dark matter in molecules. *Physical Review X*, 8(4): 041001, 2018.

[AF11] Peter W Atkins and Ronald S Friedman. *Molecular quantum mechanics*. Oxford university press, 2011.

[AH18] Vitaly Andreev and NR Hutzler. Improved limit on the electric dipole moment of the electron. *Nature*, 562(7727): 355–360, 2018.

[AKS+17] Nitzan Akerman, Michael Karpov, Yair Segev, Natan Bibelnik, Julia Narevicius, and Edvardas Narevicius. Trapping of molecular oxygen together with lithium atoms. *Physical review letters*, 119(7): 073204, 2017.

[ARM+95] M. H. Anderson, Ensher J. R., M. R. Matthews, C. E. Wieman, and Cornell E. A. Observation of bose-einstein condensation in a dilute atomic vapor. *Science*, 269: 198–201, 1995.

[Bal16] N Balakrishnan. Perspective: Ultracold molecules and the dawn of cold controlled chemistry. *The Journal of Chemical Physics*, 145(15): 150901, 2016.

[BBM99] Hendrick L. Bethlem, Giel Berden, and Gerard Meijer. Decelerating Neutral Dipolar Molecules. *Phys. Rev. Lett.*, 83: 1558, 1999, http://dx.doi.org/10.1103/PhysRevLett.83.1558.

[BDJ+13] J. Bagdonaite, M. Daprà, P. Jansen, H. L. Bethlem, W. Ubachs, S. Muller, C. Henkel, and K. M. Menten. Robust constraint on a drifting proton-to-electron mass ratio at z=0.89 from methanol observation at three radio telescopes. *Phys. Rev. Lett.*, 111: 231101, Dec 2013, http://link.aps.org/doi/10.1103/PhysRevLett.111.231101.

[BDPZ12] M. A. Baranov, M. Dalmonte, G. Pupillo, and P. Zoller. Condensed matter theory of dipolar quantum gases. *Chem. Rev.*, 112(9): 5012–5061, Sep 2012, http://pubs.acs.org/doi/abs/10.1021/cr2003568.

[BDZ08] Immanuel Bloch, Jean Dalibard, and Wilhelm Zwerger. Many-body physics with ultracold gases. *Rev. Mod. Phys.*, 80: 885, 2008, http://dx.doi.org/10.1103/RevModPhys.80.885.

[BH93] R. Braun and P. Hess. Optimization of a commercial quadrupole mass spectrometer for time-of-flight measurements of laser desorption. *International Journal of Mass Spectrometry and Ion Processes*, 125(2): 229 – 239, 1993, http://www.sciencedirect.com/science/article/pii/016811769380045G.

[BMDM04] BB Blinov, DL Moehring, L-M Duan, and Chris Monroe. Observation of entanglement between a single trapped atom and a single photon. *Nature*, 428(6979): 153, 2004.

[BMK+89] T. H. Bergeman, Patrick McNicholl, Jan Kycia, Harold Metcalf, and N. L. Balazs. Quantized motion of atoms in a quadrupole magnetostatic trap. *J. Opt. Soc. Am. B*, 6(11): 2249–2256, Nov 1989, http://josab.osa.org/abstract.cfm?URI=josab-6-11-2249.

[BMN+14] J. F. Barry, D. J. McCarron, E. B. Norrgard, M. H. Steinecker, and D. DeMille. Magneto-optical trapping of a diatomic molecule. *Nature*, 512(7514): 286–289, August 2014, http://dx.doi.org/10.1038/nature13634.

[BMV74] H C W Beijerinck, R G J M Moonen, and N F Verster. Calibration of a time-of-flight machine for molecular beam studies. *Journal of Physics E: Scientific Instruments*, 7(1): 31, 1974, http://stacks.iop.org/0022-3735/7/i=1/a=009.

[Bon64] A. Bondi. van der waals volumes and radii. *The Journal of Physical Chemistry*, 68(3): 441–451, 1964, https://doi.org/10.1021/j100785a001.

[BRY17] John L Bohn, Ana Maria Rey, and Jun Ye. Cold molecules: Progress in quantum engineering of chemistry and quantum matter. *Science*, 357(6355): 1002–1010, 2017.

[BS09] Martin T Bell and Timothy P Softley. Ultracold molecules and ultracold chemistry. *Mol. Phys.*, 107: 99, 2009, http://dx.doi.org/10.1080/00268970902724955.

[BSD11] J. F. Barry, E. S. Shuman, and D. DeMille. A bright, slow cryogenic molecular beam source for free radicals. *Phys. Chem. Chem. Phys.*, 13: 18936–18947, 2011, http://dx.doi.org/10.1039/C1CP20335E.

[BSH+13] N. E. Bulleid, S. M. Skoff, R. J. Hendricks, B. E. Sauer, E. A. Hinds, and M. R. Tarbutt. Characterization of a cryogenic beam source for atoms and molecules. *Phys. Chem. Chem. Phys.*, 15: 12299–12307, 2013, http://dx.doi.org/10.1039/C3CP51553B.

[CAA+18] Lawrence W Cheuk, Loïc Anderegg, Benjamin L Augenbraun, Yicheng Bao, Sean Burchesky, Wolfgang Ketterle, and John M Doyle. λ-enhanced imaging of molecules in an optical trap. *Physical review letters*, 121(8): 083201, 2018.

[CBC+14] The ACME Collaboration, J. Baron, W. C. Campbell, D. DeMille, J. M. Doyle, G. Gabrielse, Y. V. Gurevich, P. W. Hess, N. R. Hutzler, E. Kirilov, I. Kozyryev, B. R. Oï¿œLeary, C. D. Panda, M. F. Parsons, E. S. Petrik, B. Spaun, A. C. Vutha, and A. D. West. Order of magnitude smaller limit on the electric dipole moment of the electron. *Science*, 343(6168): 269–272, 2014, http://www.sciencemag.org/content/343/6168/269.abstract.

[CDS12] Laurent Canetti, Marco Drewes, and Mikhail Shaposhnikov. Matter and antimatter in the universe. *New Journal of Physics*, 14(9): 095012, 2012, http://stacks.iop.org/1367-2630/14/i=9/a=095012.

[CDW+18a] L Caldwell, JA Devlin, HJ Williams, NJ Fitch, EA Hinds, BE Sauer, and MR Tarbutt. Deep laser cooling and efficient magnetic compression of molecules. *arXiv preprint arXiv:1812.07926*, 2018.

[CDW+18b] Alejandra L Collopy, Shiqian Ding, Yewei Wu, Ian A Finneran, Loïc Anderegg, Benjamin L Augenbraun, John M Doyle, and Jun Ye. 3d magneto-optical trap of yttrium monoxide. *Physical Review Letters*, 121(21): 213201, 2018.

[CGG+17] William B Cairncross, Daniel N Gresh, Matt Grau, Kevin C Cossel, Tanya S Roussy, Yiqi Ni, Yan Zhou, Jun Ye, and Eric A Cornell. Precision measurement of the electrons electric dipole moment using trapped molecular ions. *Physical review letters*, 119(15): 153001, 2017.

[CWB+14] S. Chervenkov, X. Wu, J. Bayerl, A. Rohlfes, T. Gantner, M. Zeppenfeld, and G. Rempe. Continuous centrifuge decelerator for polar molecules. *Phys. Rev. Lett.*, 112: 013001, Jan 2014, http://link.aps.org/doi/10.1103/PhysRevLett.112.013001.

[DCT89] J. Dalibard and C. Cohen-Tannoudji. Laser cooling below the doppler limit by polarization gradients: simple theoretical models. *J. Opt. Soc. Am. B*, 6(11): 2023–2045, Nov 1989, http://josab.osa.org/abstract.cfm?URI=josab-6-11-2023.

[DeM02] D. DeMille. Quantum computation with trapped polar molecules. *Phys. Rev. Lett.*, 88: 067901, Jan 2002, http://link.aps.org/doi/10.1103/PhysRevLett.88.067901.

[DMA+95] K. B. Davis, M. O. Mewes, M. R. Andrews, N. J. van Druten, D. S. Durfee, D. M. Kurn, and W. Ketterle. Bose-einstein condensation in a gas of sodium atoms. *Phys. Rev. Lett.*, 75: 3969–3973, Nov 1995, http://link.aps.org/doi/10.1103/PhysRevLett.75.3969.

[DMJ+95] Kendall B Davis, Marc-Oliver Mewes, Michael A Joffe, Michael R Andrews, and Wolfgang Ketterle. Evaporative cooling of sodium atoms. *Physical review letters*, 74(26): 5202, 1995.

[DR04] M. D. Di Rosa. Laser-cooling molecules. *Eur. Phys. J. D*, 31: 395, 2004, http://dx.doi.org/10.1140/epjd/e2004-00167-2.

[DSL+17] Maximilian J. Doppelbauer, Otto Schullian, Jerome Loreau, Nathalie Vaeck, Ad van der Avoird, Christopher J. Rennick, Timothy P. Softley, and Brianna R. Heazlewood. Using a direct simulation monte carlo approach to model collisions in a buffer gas cell. *The Journal of Chemical Physics*, 146(4): 044302, 2017, https://doi.org/10.1063/1.4974253.

[DST+06] Leanne D Duffy, P Sikivie, DB Tanner, Stephen J Asztalos, C Hagmann, D Kinion, LJ Rosenberg, K Van Bibber, DB Yu, and RF Bradley. High resolution search for dark-matter axions. *Physical Review D*, 74(1): 012006, 2006.

[EBHZ85] W Ertmer, R Blatt, JL Hall, and M Zhu. Laser manipulation of atomic beam velocities: demonstration of stopped atoms and velocity reversal. *Physical review letters*, 54(10): 996, 1985.

[ECF+04] D. Egorov, W. C. Campbell, B. Friedrich, S.E. Maxwell, E. Tsikata, L. D. van Buuren, and J. M. Doyle. Buffer-gas cooling of NH via the beam loaded buffer-gas method. *Eur. Phys. J. D*, 31: 307, 2004, http://dx.doi.org/10.1140/epjd/e2004-00140-1.

[Edw83] AWF Edwards. Pascal's problem: The'gambler's ruin'. *International Statistical Review/Revue Internationale de Statistique*, pages 73–79, 1983.

[Eke91] Artur K Ekert. Ak ekert, phys. rev. lett. 67, 661 (1991). *Phys. Rev. Lett.*, 67: 661, 1991.

[EMS+11] B. G. U. Englert, M. Mielenz, C. Sommer, J. Bayerl, M. Motsch, P. W. H. Pinkse, G. Rempe, and M. Zeppenfeld. Storage and adiabatic cooling of polar molecules in a microstructured trap. *Phys. Rev. Lett.*, 107: 263003, Dec 2011, http://link.aps.org/doi/10.1103/PhysRevLett.107.263003.

[Eng13] Barbara Englert. *Sisyphus-KÃŒhlung von polyatomaren MolekÃŒlen*. PhD thesis, Max-Planck-Institut f ?ur Quantenoptik, Garching und Physik Department, Technische Universit ?at M ?unchen, 2013.

[FCC+98] A. Fioretti, D. Comparat, A. Crubellier, O. Dulieu, F. Masnou-Seeuws, and P. Pillet. Formation of Cold Cs_2 Molecules through Photoassociation. *Phys. Rev. Lett.*, 80: 4402, 1998, http://dx.doi.org/10.1103/PhysRevLett.80.4402.

[Fen10] Jonathan L Feng. Dark matter candidates from particle physics and methods of detection. *Annual Review of Astronomy and Astrophysics*, 48: 495–545, 2010.

[Fer01] Katia M Ferriere. The interstellar environment of our galaxy. *Reviews of Modern Physics*, 73(4): 1031, 2001.

[GFO+89] Gerald Gabrielse, X Fei, LA Orozco, RL Tjoelker, J Haas, H Kalinowsky, TA Trainor, and W Kells. Cooling and slowing of trapped antiprotons below 100 mev. *Physical review letters*, 63(13): 1360, 1989.

[GME+02] Markus Greiner, Olaf Mandel, Tilman Esslinger, Theodor W. Hänsch, and Immanuel Bloch. Quantum phase transition from a superfluid to a Mott insulator in a gas of ultracold atoms. *Nature*, 415: 39, 2002, http://dx.doi.org/10.1038/415039a.

[GPE+15] Rosa Glöckner, Alexander Prehn, Barbara G. U. Englert, Gerhard Rempe, and Martin Zeppenfeld. Rotational cooling of trapped polyatomic molecules. *Phys. Rev. Lett.*, 115: 233001, Dec 2015, http://link.aps.org/doi/10.1103/PhysRevLett.115.233001.

[GPRZ15] Rosa Glöckner, Alexander Prehn, Gerhard Rempe, and Martin Zeppenfeld. Rotational state detection of electrically trapped polyatomic molecules. *New Journal of Physics*, 17(5): 055022, 2015, http://stacks.iop.org/1367-2630/17/i=5/a=055022.

[GWO00] Rudolf Grimm, Matthias Weidemüller, and Yurii B Ovchinnikov. Optical dipole traps for neutral atoms. In *Advances in atomic, molecular, and optical physics*, volume 42, pages 95–170. Elsevier, 2000.

[GZL+16] Mingyang Guo, Bing Zhu, Bo Lu, Xin Ye, Fudong Wang, Romain Vexiau, Nadia Bouloufa-Maafa, Goulven Quéméner, Olivier Dulieu, and Dajun Wang. Creation of an ultracold gas of ground-state dipolar $^{23}Na^{87}Rb$ molecules. *Phys. Rev. Lett.*, 116: 205303, May 2016, https://link.aps.org/doi/10.1103/PhysRevLett.116.205303.

[HGS+12] A. B. Henson, S. Gersten, Y. Shagam, J. Narevicius, and E. Narevicius. Observation of resonances in penning ionization reactions at sub-kelvin temperatures in merged beams. *Science*, 338(6104): 234–238, 2012, http://www.sciencemag.org/content/338/6104/234.abstract.

[HKS+11] J. J. Hudson, D. M. Kara, I. J. Smallman, B. E. Sauer, M. R. Tarbutt, and E. A. Hinds. Improved measurement of the shape of the electron. *Nature*, 473(7348): 493–496, May 2011, http://dx.doi.org/10.1038/nature10104.

[HLD12] Nicholas R. Hutzler, Hsin-I Lu, and John M. Doyle. The buffer gas beam: An intense, cold, and slow source for atoms and molecules. *Chem. Rev.*, 112(9): 4803–4827, Sep 2012, http://pubs.acs.org/doi/abs/10.1021/cr200362u.

[HM08] Eric Herbst and Tom J Millar. The chemistry of cold interstellar cloud cores. In *Low Temperatures and cold molecules*, pages 1–54. World Scientific, 2008.

[Hut14] Nick Hutzler. *A New Limit on the Electron Electric Dipole Moment: Beam Production, Data Interpretation, and Systematics*. PhD thesis, Harvard University, 2014.

[HYS+13] Matthew T Hummon, Mark Yeo, Benjamin K Stuhl, Alejandra L Collopy, Yong Xia, and Jun Ye. 2d magneto-optical trapping of diatomic molecules. *Physical review letters*, 110(14): 143001, 2013.

[JBJDL13] Amine Jaouadi, Etienne Barrez, Yves Justum, and M Desouter-Lecomte. Quantum gates in hyperfine levels of ultracold alkali dimers by revisiting constrained-phase optimal control design. *The Journal of Chemical Physics*, 139(1): 014310, 2013.

[JO15] Justin Jankunas and Andreas Osterwalder. Cold and controlled molecular beams: Production and applications. *Annual Review of Physical Chemistry*, 66(1): 241–262, 2015, http://dx.doi.org/10.1146/annurev-physchem-040214-121307. PMID: 25532950.

[JRR+04] T. Junglen, T. Rieger, S. A. Rangwala, P. W. H. Pinkse, and G. Rempe. Slow ammonia molecules in an electrostatic quadrupole guide. *Eur. Phys. J. D*, 31: 365–373, 2004, http://dx.doi.org/10.1140/epjd/e2004-00130-3.

[Jun05] Tobias Junglen. *Guiding and Trapping of Cold Dipolar Molecules*. PhD thesis, Max-Planck-Institut für Quantenoptik, Garching, und Fakultät für Physik, Technische Universität München, 2005.

[JZ18] Ferdinand Jarisch and Martin Zeppenfeld. State resolved investigation of förster resonant energy transfer in collisions between polar molecules and rydberg atoms. *New Journal of Physics*, 2018.

[KBM+17] Ivan Kozyryev, Louis Baum, Kyle Matsuda, Benjamin L Augenbraun, Loic Anderegg, Alexander P Sedlack, and John M Doyle. Sisyphus laser cooling of a polyatomic molecule. *Physical review letters*, 118(17): 173201, 2017.

[KFK+97] Jinha Kim, Bretislav Friedrich, Daniel P Katz, David Patterson, Jonathan D Weinstein, Robert DeCarvalho, and John M Doyle. Buffer-gas loading and magnetic trapping of atomic europium. *Physical Review Letters*, 78(19): 3665, 1997.

[KSF+16] Mallikarjun Karra, Ketan Sharma, Bretislav Friedrich, Sabre Kais, and Dudley Herschbach. Prospects for quantum computing with an array of ultracold polar paramagnetic molecules. *The Journal of Chemical Physics*, 144(9): 094301, 2016.

[KSS+17] Ayelet Klein, Yuval Shagam, Wojciech Skomorowski, Piotr S Zuchowski, Mariusz Pawlak, Liesbeth MC Janssen, Nimrod Moiseyev, Sebastiaan YT van de Meerakker, Ad van der Avoird, Christiane P Koch, et al. Directly probing anisotropy in atom-molecule collisions through quantum scattering resonances. *Nature Physics*, 13(1): 35–38, 2017.

[KVD+96] Wolfgang Ketterle, NJ Van Druten, et al. Evaporative cooling of trapped atoms. *Adv. At. Mol. Opt. Phys*, 37(0): 181, 1996.

[LAKC96] HJ Lee, CS Adams, M Kasevich, and S Chu. Raman cooling of atoms in an optical dipole trap. *Physical review letters*, 76(15): 2658, 1996.

[LAT+18] J Lim, JR Almond, MA Trigatzis, JA Devlin, NJ Fitch, BE Sauer, MR Tarbutt, and EA Hinds. Laser cooled ybf molecules for measuring the electrons electric dipole moment. *Physical review letters*, 120(12): 123201, 2018.

[LO05] Chaohong Lee and Elena A Ostrovskaya. Quantum computation with diatomic bits in optical lattices. *Physical Review A*, 72(6): 062321, 2005.

[LWW+88] Paul D Lett, Richard N Watts, Christoph I Westbrook, William D Phillips, Phillip L Gould, and Harold J Metcalf. Observation of atoms laser cooled below the doppler limit. *Physical review letters*, 61(2): 169, 1988.

[MB08] Edmund R. Meyer and John L. Bohn. Prospects for an electron electric-dipole moment search in metastable ThO and ThF^+. *Phys. Rev. A*, 78: 010502(R), 2008, http://dx.doi.org/10.1103/PhysRevA.78.010502.

[MCM09a] Samuel A Meek, Horst Conrad, and Gerard Meijer. A stark decelerator on a chip. *New Journal of Physics*, 11(5): 055024, 2009.

[MCM09b] Samuel A. Meek, Horst Conrad, and Gerard Meijer. Trapping Molecules on a Chip. *Science*, 324: 5935, 2009, http://dx.doi.org/10.1126/science.1175975.

[MGJ+14] Peter K. Molony, Philip D. Gregory, Zhonghua Ji, Bo Lu, Michael P. Köppinger, C. Ruth Le Sueur, Caroline L. Blackley, Jeremy M. Hutson, and Simon L. Cornish. Creation of ultracold $^{87}Rb^{133}Cs$ molecules in the rovibrational ground state. *Phys. Rev. Lett.*, 113: 255301, Dec 2014, https://link.aps.org/doi/10.1103/PhysRevLett.113.255301.

[MO07] Christopher F McKee and Eve C Ostriker. Theory of star formation. *Annu. Rev. Astron. Astrophys.*, 45: 565–687, 2007.

[Mot09] Michael Motsch. *Cold Guided Beams of Polar Molecules*. PhD thesis, MPQ, 2009.

[MSZ+09] M. Motsch, C. Sommer, M. Zeppenfeld, L D van Buuren, G. Rempe, and P W H Pinkse. Collisional effects in the formation of cold guided beams of polar molecules. *New J. Phys.*, 11: 055030, 2009, http://dx.doi.org/10.1088/1367-2630/11/5/055030.

[MSZD18] DJ McCarron, MH Steinecker, Y Zhu, and D DeMille. Magnetic trapping of an ultracold gas of polar molecules. *Physical review letters*, 121(1): 013202, 2018.

[NMS+16] EB Norrgard, DJ McCarron, MH Steinecker, MR Tarbutt, and D DeMille. Submillikelvin dipolar molecules in a radio-frequency magneto-optical trap. *Physical review letters*, 116(6): 063004, 2016.

[NOW+10] K-K Ni, S Ospelkaus, D Wang, G Quéméner, B Neyenhuis, MHG De Miranda, JL Bohn, J Ye, and DS Jin. Dipolar collisions of polar molecules in the quantum regime. *Nature*, 464(7293): 1324, 2010.

[NR12] Edvardas Narevicius and Mark G. Raizen. Toward cold chemistry with magnetically decelerated supersonic beams. *Chem. Rev.*, 112(9): 4879–4889, Sep 2012, http://pubs.acs.org/doi/abs/10.1021/cr2004597.

[NRG18] Kang-Kuen Ni, Till Rosenband, and David D. Grimes. Dipolar exchange quantum logic gate with polar molecules. *arXiv:1805.10930*, 2018.

[OMH+10] Andreas Osterwalder, Samuel A Meek, Georg Hammer, Henrik Haak, and Gerard Meijer. Deceleration of neutral molecules in macroscopic traveling traps. *Physical Review A*, 81(5): 051401, 2010.

[ONW+10] S. Ospelkaus, K.-K. Ni, D. Wang, M. H. G. de Miranda, B. Neyenhuis, G. Quï¿œmï¿œener, P. S. Julienne, J. L. Bohn, D. S. Jin, and J. Ye. Quantum-state controlled chemical reactions of ultracold

potassium-rubidium molecules. *Science*, 327(5967): 853–857, 2010, http://www.sciencemag.org/content/327/5967/853.abstract.

[PAEC95] Wolfgang Petrich, Michael H Anderson, Jason R Ensher, and Eric A Cornell. Stable, tightly confining magnetic trap for evaporative cooling of neutral atoms. *Physical Review Letters*, 74(17): 3352, 1995.

[PIG+16] Alexander Prehn, Martin Ibrügger, Rosa Glöckner, Gerhard Rempe, and Martin Zeppenfeld. Optoelectrical cooling of polar molecules to submillikelvin temperatures. *Physical review letters*, 116(6): 063005, 2016.

[PM82] William D. Phillips and Harold Metcalf. Laser deceleration of an atomic beam. *Phys. Rev. Lett.*, 48: 596–599, Mar 1982, http://link.aps.org/doi/10.1103/PhysRevLett.48.596.

[PMP+85] John Prodan, Alan Migdall, William D Phillips, Ivan So, Harold Metcalf, and Jean Dalibard. Stopping atoms with laser light. *Physical review letters*, 54(10): 992, 1985.

[PPM85] William D Phillips, John V Prodan, and Harold J Metcalf. Laser cooling and electromagnetic trapping of neutral atoms. *JOSA B*, 2(11): 1751–1767, 1985.

[PWZ15] Jee Woo Park, Sebastian A. Will, and Martin W. Zwierlein. Ultracold dipolar gas of fermionic $^{23}Na^{40}K$ molecules in their absolute ground state. *Phys. Rev. Lett.*, 114: 205302, May 2015, https://link.aps.org/doi/10.1103/PhysRevLett.114.205302.

[PYL+17] Jee Woo Park, Zoe Z Yan, Huanqian Loh, Sebastian A Will, and Martin W Zwierlein. Second-scale nuclear spin coherence time of ultracold 23na40k molecules. *Science*, 357(6349): 372–375, 2017.

[Rab16] Isabel Rabey. *Improved shot noise limit of the YbF EDM experiment.* PhD thesis, Imperial College London, 2016.

[RCSD02] B. C. Regan, Eugene D. Commins, Christian J. Schmidt, and David DeMille. New Limit on the Electron Electric Dipole Moment. *Phys. Rev. Lett.*, 88: 071805, 2002, http://dx.doi.org/10.1103/PhysRevLett.88.071805.

[RJR+03] S. A. Rangwala, T. Junglen, T. Rieger, P. W. H. Pinkse, and G. Rempe. Continuous source of translationally cold dipolar molecules. *Phys. Rev. A*, 67: 043406, 2003, http://dx.doi.org/10.1103/PhysRevA.67.043406.

[RPC+87] E. L. Raab, M. Prentiss, Alex Cable, Steven Chu, and D. E. Pritchard. Trapping of neutral sodium atoms with radiation pressure. *Phys. Rev. Lett.*, 59: 2631–2634, Dec 1987, http://link.aps.org/doi/10.1103/PhysRevLett.59.2631.

[SB09] Markus Schröder and Alex Brown. Realization of the cnot quantum gate operation in six-dimensional ammonia using the oct-mctdh approach. *The Journal of chemical physics*, 131(3): 034101, 2009.

[SBC+15] L Santamaria, C Braggio, G Carugno, V Di Sarno, P Maddaloni, and G Ruoso. Axion dark matter detection by laser spectroscopy of ultracold molecular oxygen: a proposal. *New Journal of Physics*, 17(11): 113025, 2015.

[SBD10] E. S. Shuman, J. F. Barry, and D. DeMille. Laser cooling of a diatomic molecule. *Nature*, 467(7317): 820–823, October 2010, http://dx.doi.org/10.1038/nature09443.

[SBGH13] Robin J Shannon, Mark A Blitz, Andrew Goddard, and Dwayne E Heard. Accelerated chemistry in the reaction between the hydroxyl radical and methanol at interstellar temperatures facilitated by tunnelling. *Nature chemistry*, 5(9): 745, 2013.

[SBK+91] Guy Savard, G Bollen, H-J Kluge, RB Moore, Th Otto, L Schweikhard, H Stolzenberg, U Wiess, et al. A new cooling technique for heavy ions in a penning trap. *Physics Letters A*, 158(5): 247–252, 1991.

[SBL+18] Frauke Seeßelberg, Nikolaus Buchheim, Zhen-Kai Lu, Tobias Schneider, Xin-Yu Luo, Eberhard Tiemann, Immanuel Bloch, and Christoph Gohle. Modeling the adiabatic creation of ultracold polar ^{23}na^{40}K molecules. *Phys. Rev. A*, 97: 013405, Jan 2018, https://link.aps.org/doi/10.1103/PhysRevA.97.013405.

[Sho94] Peter W Shor. Algorithms for quantum computation: Discrete logarithms and factoring. In *Foundations of Computer Science, 1994 Proceedings., 35th Annual Symposium on*, pages 124–134. Ieee, 1994.

[SMC+10] C. Sommer, M. Motsch, S. Chervenkov, L. D. van Buuren, M. Zeppenfeld, P. W. H. Pinkse, and G. Rempe. Velocity-selected molecular pulses produced by an electric guide. *Phys. Rev. A*, 82: 013410, Jul 2010, http://link.aps.org/doi/10.1103/PhysRevA.82.013410.

[SNR+11] Holger P Specht, Christian Nölleke, Andreas Reiserer, Manuel Uphoff, Eden Figueroa, Stephan Ritter, and Gerhard Rempe. A single-atom quantum memory. *Nature*, 473(7346): 190, 2011.

[Som11] Christian Sommer. *Construction and Operation of a Source for Cold Polar Molecules*. PhD thesis, Max-Planck-Institut für Quantenoptik, Garching, und Fakultät für Physik, Technische Universität München, 2011.

[SPT13] LV Skripnikov, AN Petrov, and AV Titov. Communication: Theoretical study of tho for the electron electric dipole moment search. *The Journal of Chemical Physics*, 2013.

[SSWY08] Benjamin K Stuhl, Brian C Sawyer, Dajun Wang, and Jun Ye. Magneto-optical trap for polar molecules. *Physical review letters*, 101(24): 243002, 2008.

[SvBM+09] C. Sommer, L. D. van Buuren, M. Motsch, S. Pohle, J. Bayerl, P. W. H. Pinkse, and G. Rempe. Continuous guided beams of slow and internally cold polar molecules. *Faraday Discuss.*, 142: 203, 2009, http://dx.doi.org/10.1039/b819726a.

[TdVR02] Carmen M. Tesch and Regina de Vivie-Riedle. Quantum Computation with Vibrationally Excited Molecules. *Phys. Rev. Lett.*, 89: 157901, 2002, http://dx.doi.org/10.1103/PhysRevLett.89.157901.

[THHK05] Masao Takamoto, Feng-Lei Hong, Ryoichi Higashi, and Hidetoshi Katori. An optical lattice clock. *Nature*, 435(7040): 321, 2005.

[Tie13] AGGM Tielens. The molecular universe. *Reviews of Modern Physics*, 85(3): 1021, 2013.

[TRS+14] Tetsu Takekoshi, Lukas Reichsöllner, Andreas Schindewolf, Jeremy M. Hutson, C. Ruth Le Sueur, Olivier Dulieu, Francesca Ferlaino, Rudolf Grimm, and Hanns-Christoph Nägerl. Ultracold dense samples of dipolar rbcs molecules in the rovibrational and hyperfine ground state. *Phys. Rev. Lett.*, 113: 205301, Nov 2014, https://link.aps.org/doi/10.1103/PhysRevLett.113.205301.

[TW77] J Peter Toennies and Klaus Winkelmann. Theoretical studies of highly expanded free jets: Influence of quantum effects and a realistic intermolecular potential. *The Journal of Chemical Physics*, 66(9): 3965–3979, 1977.

[TWH+17] S Truppe, HJ Williams, M Hambach, L Caldwell, NJ Fitch, EA Hinds, BE Sauer, and MR Tarbutt. Molecules cooled below the doppler limit. *Nature Physics*, 13(12): 1173, 2017.

[UHH02] Th. Udem, R. Holzwarth, and T. W. Hänsch. Optical frequency metrology. *Nature*, 416: 233, 2002, http://www.nature.com/nature/journal/v416/n6877/full/416233a.html.

[vBSM+09] L. D. van Buuren, C. Sommer, M. Motsch, S. Pohle, M. Schenk, J. Bayerl, P. W. H. Pinkse, and G. Rempe. Electrostatic Extraction of Cold Molecules from a Cryogenic Reservoir. *Phys. Rev. Lett.*, 102: 033001, 2009, http://dx.doi.org/10.1103/PhysRevLett.102.033001.

[VCG+10] A C Vutha, W C Campbell, Y V Gurevich, N R Hutzler, M Parsons, D Patterson, E Petrik, B Spaun, J M Doyle, G Gabrielse, and D DeMille. Search for the electric dipole moment of the electron with thorium monoxide. *J. Phys. B: At. Mol. Opt. Phys.*, 43(7): 074007, 2010, http://stacks.iop.org/0953-4075/43/i=7/a=074007.

[vdMBM08] S. Y. T. van de Meerakker, H. L. Bethlem, and G. Meijer. Taming molecular beams. *Nature Phys.*, 4: 595–602, 2008, http://dx.doi.org/10.1038/nphys1031.

[VOC+15] Sjoerd N Vogels, Jolijn Onvlee, Simon Chefdeville, Ad van der Avoird, Gerrit C Groenenboom, and Sebastiaan YT van de Meerakker. Imaging resonances in low-energy no-he inelastic collisions. *Science*, 350(6262): 787–790, 2015.

[VZOV+14] Alexander Von Zastrow, Jolijn Onvlee, Sjoerd N Vogels, Gerrit C Groenenboom, Ad Van Der Avoird, and Sebastiaan YT Van De Meerakker. State-resolved diffraction oscillations imaged for inelastic collisions of no radicals with he, ne and ar. *Nature chemistry*, 6(3): 216, 2014.

[WdG+98] J. D. Weinstein, R. deCarvalho, T. Guillet, B. Friedrich, and J. M. Doyle. Magnetic trapping of calcium monohydride molecules at millikelvin temperatures. *Nature*, 395: 148–150, 1998, http://dx.doi.org/10.1038/25949.

[WGK+17] Xing Wu, Thomas Gantner, Manuel Koller, Martin Zeppenfeld, Sotir Chervenkov, and Gerhard Rempe. A cryofuge for cold-collision experiments with slow polar molecules. *Science*, 358(6363): 645–648, 2017, http://science.sciencemag.org/content/358/6363/645.

[WGZ+16] Xing Wu, Thomas Gantner, Martin Zeppenfeld, Sotir Chervenkov, and Gerhard Rempe. Thermometry of guided molecular beams from a cryogenic buffer-gas cell. *ChemPhysChem*, 17(22): 3631–3640, 2016, http://dx.doi.org/10.1002/cphc.201600559.

[WI79] D. J. Wineland and W. M. Itano. Laser cooling of atoms. *Phys. Rev. A*, 20: 1521, 1979, http://dx.doi.org/10.1103/PhysRevA.20.1521.

[WKFH11] Qi Wei, Sabre Kais, Bretislav Friedrich, and Dudley Herschbach. Entanglement of polar symmetric top molecules as candidate qubits. *The Journal of chemical physics*, 135(15): 154102, 2011.

[WMC15] M L Wall, K Maeda, and Lincoln D Carr. Realizing unconventional quantum magnetism with symmetric top molecules. *New Journal of Physics*, 17(2): 025001, 2015, http://stacks.iop.org/1367-2630/17/i=2/a=025001.

[WQS+04] D. Wang, J. Qi, M. F. Stone, O. Nikolayeva, H. Wang, B. Hattaway, S. D. Gensemer, P. L. Gould, E. E. Eyler, and W. C. Stwalley. Photoassociative Production and Trapping of Ultracold KRb Molecules. *Phys. Rev. Lett.*, 93: 243005, 2004, http://dx.doi.org/10.1103/PhysRevLett.93.243005.

[Wu17] Xing Wu. *A Centrifuge Decelerator and a Thermometer for Cold Polar Molecules*. PhD thesis, Max-Planck-Institut für Quantenoptik, Garching, und Fakultät für Physik, Technische Universität München, 2017.

[YKC06] S. F. Yelin, K. Kirby, and Robin Côté. Schemes for robust quantum computation with polar molecules. *Phys. Rev. A*, 74: 050301, 2006, http://dx.doi.org/10.1103/PhysRevA.74.050301.

[YMG+13] Bo Yan, Steven A Moses, Bryce Gadway, Jacob P Covey, Kaden RA Hazzard, Ana Maria Rey, Deborah S Jin, and Jun Ye. Observation of dipolar spin-exchange interactions with lattice-confined polar molecules. *Nature*, 501(7468): 521, 2013.

[ZBMS15] Sabrina Zinn, Thomas Betz, Chris Medcraft, and Melanie Schnell. Structure determination of trans-cinnamaldehyde by broadband microwave spectroscopy. *Phys. Chem. Chem. Phys.*, 17: 16080–16085, 2015, http://dx.doi.org/10.1039/C5CP02582F.

[ZCW+14] Valentina Zhelyazkova, Anne Cournol, Thomas E Wall, Aki Matsushima, Jonathan J Hudson, EA Hinds, MR Tarbutt, and BE Sauer. Laser cooling and slowing of caf molecules. *Physical Review A*, 89(5): 053416, 2014.

[ZEG+12] Martin Zeppenfeld, Barbara G. U. Englert, Rosa Glöckner, Alexander Prehn, Manuel Mielenz, Christian Sommer, Laurens D. van Buuren, Michael Motsch, and Gerhard Rempe. Sisyphus cooling of electrically trapped polyatomic molecules. *Nature*, 491(7425): 570–573, November 2012, http://dx.doi.org/10.1038/nature11595.

[Zep13] Martin Zeppenfeld. *Electric Trapping and Cooling of Polyatomic Molecules*. PhD thesis, Max-Planck-Institut f ?ur Quantenoptik, Garching und Physik Department, Technische Universit ?at M ?unchen, 2013.

[Zep17] Martin Zeppenfeld. Nondestructive detection of polar molecules via rydberg atoms. *EPL (Europhysics Letters)*, 118(1): 13002, 2017.

[ŻH10] Piotr S Żuchowski and Jeremy M Hutson. Reactions of ultracold alkali-metal dimers. *Physical Review A*, 81(6): 060703, 2010.

[ZMPR09] M. Zeppenfeld, M. Motsch, P. W. H. Pinkse, and G. Rempe. Optoelectrical cooling of polar molecules. *Phys. Rev. A*, 80: 041401, Oct 2009, http://link.aps.org/doi/10.1103/PhysRevA.80.041401.

[ZS88] K Zioutas and Y Semertzidis. A new detector scheme for axions. *Physics Letters A*, 130(2): 94–97, 1988.

Acknowledgments

I first want to thank Gerhard Rempe for giving me the amazing opportunity to work in this group. I really appreciate the freedom to try own ideas, his curiosity and thorough questioning taught me to be a better scientist.

I thank Martin Zeppenfeld for all his ideas, the lessons on physics, data analysis and programming. The fast solution of problems in the day to day lab business is invaluable.

I also want to thank Sotir Chervenkov for his calm attitude and all the lessons on molecule theory.

Then I want to thank Xing Wu, who first introduced me to the experiment, and explained the ins and outs on how to handle the beast. I'm also grateful for all the discussions in the lab, and his eagerness to always tackle the problems wherever they appear.

I thank Manuel Koller for the great atmosphere in the office and the lab, and his readiness to work at whatever task is coming up. I also appreciate the discussion about everything, and the positive mood when the setup is acting up, again... It's easier to leave knowing the setup is in good hands.

Next I want to thank Isabel Rabey for the knowledge and expertise she brought to the experiment, the interesting discussions, and the optimistic attitude.

Thanks also to Florian Jung for joining the group, the enthusiasm and interest in all topics he brings.

I also want to thank the rest of the molecule team, Barbara Englert, Rosa Glöckner, Alexander Prehn, Martin Ibrügger, and Maximilian Löw. It was nice to share group meetings and equipment, and discuss about molecules and other stuff.

Thank you also to the technicians, Sepp Bayerl, Helmut Stehbeck, Franz Denk, Thomas Wiesmeier, Tobi Urban, Florian Furchtsam, and Johannes Siegl. They are the backbone for setting up a new experiment, extending it, improving it... Thank you also for all the patience in the discussions when explaining technical details and limitations, when plans keep changing every other day, or when finding the source of the weird effects on the setup.

Thanks also to Iris Anneser who is always helpful when there is an administrative problem, and all the organisation.

Also thank you to the rest of the group, for the discussions, beers, skiing days, practical help, cakes, lent equipment, coffees, kicker matches, physical explanations

and all the swearwords and insults I learned. The atmosphere in the group made the work in the last years so much more enjoyable.

Thanks also to my friends outside the institute, for the cooking evenings, Tatort sessions, hikes, skitours, making music, long discussions, and one or the other alcoholic beverage. It's great to have something to look forward to when the lab is too annoying, or to enjoy the time when it's running smoothly.

Danke an meine Familie, Helga, Sepp und Andrea, die mich immer unterstützt haben und auf die ich mich immer voll verlassen kann. Ich wäre ohne euch nicht da wo ich heute bin.

Last but not least, I want to thank Barbara, who was with me for almost all the thesis time. It's great to know I can always trust her, she listens to all my stories for the hundredth time, she calms me down on the occasional rant and celebrates when things are working out. She gives me the certainty and confidence whenever I need it the most.

Without the help of all these people the dissertation couldn't have happened, and the last years wouldn't have been such a good time.